SMALL–SCALE TESTING OF FIXED–BED REGENERATORS

A Thesis Submitted to the
College of Graduate and Postdoctoral Studies
In Partial Fulfillment of the Requirements
For the Degree of Doctor of Philosophy
In the Department of Mechanical Engineering
University of Saskatchewan
Saskatoon

By

Easwaran Nampoothiry Krishnan

PERMISSION TO USE

In presenting this thesis in partial fulfillment of the requirements for a Postgraduate degree from the University of Saskatchewan, I agree that the Libraries of this University may make it freely available for inspection. I further agree that permission for copying of this thesis in any manner, in whole or in part, for scholarly purposes may be granted by the professor or professors who supervised my thesis work or, in their absence, by the Head of the Department or the Dean of the College in which my thesis work was done. It is understood that any copying or publication or use of this thesis or parts thereof for financial gain shall not be allowed without my written permission. It is also understood that due recognition shall be given to me and to the University of Saskatchewan in any scholarly use which may be made of any material in my thesis.

DISCLAIMER

Reference in this thesis/dissertation to any specific commercial products, process, or service by trade name, trademark, manufacturer, or otherwise, does not constitute or imply its endorsement, recommendation, or favoring by the University of Saskatchewan. The views and opinions of the author expressed herein do not state or reflect those of the University of Saskatchewan, and shall not be used for advertising or product endorsement purposes.

Requests for permission to copy or to make other uses of materials in this thesis in whole or part should be addressed to:

Head of the Department of Mechanical Engineering
University of Saskatchewan
Saskatoon, Saskatchewan, S7N 5A9
Canada

OR

Dean
College of Graduate and Postdoctoral Studies
University of Saskatchewan
116 Thorvaldson Building, 110 Science Place
Saskatoon, Saskatchewan, S7N 5C9
Canada

ABSTRACT

Fixed-bed regenerators (FBRs) are air-to-air energy exchangers (AAEEs) used in ventilation systems to reduce energy consumption. FBRs transfer energy by storing and releasing heat and moisture as the exchanger is cyclically exposed to different airstreams. This thesis hypothesizes that the sensible, latent, and total effectiveness of a FBR can be determined by testing a similar small-scale exchanger. The primary goal of this thesis is to develop test methods for the performance (effectiveness) evaluation of full-scale FBRs from small-scale testing.

In this thesis, a small-scale test facility is developed which simulates the operation of FBRs by moving the exchanger periodically between two airstreams. Unlike other AAEEs, FBRs are transient devices in which the outlet temperature and humidity vary periodically. The effectiveness of the FBR is determined by measuring the transient outlet temperature and humidity of the air streams. Errors in effectiveness may result due to the slow response of temperature and humidity sensors and the errors depend on the time constants and location of the sensors. Methodologies to correct the errors in the measured temperature and humidity are presented and the sensible, latent, and total effectiveness results are verified with a numerical model and field test data. The average humidity measurement technique by sampling the transient outlet air, called the bag sampling method proposed by ASHRAE standard 84-2020, is also implemented and verified in this thesis.

The challenge undertaken in this research was the development of a transient test facility and more flexible test methods at a lower cost per test than that presented in ASHRAE Standard 84-2020. The proposed methodology, which is especially useful during product development, does not require full-scale prototypes, large laboratories, or a high volume of conditioned airflow. In the future, this new facility and methods can be implemented to test FBRs.

ACKNOWLEDGEMENTS

First and foremost, I would like to express my sincere thanks to my supervisor, Prof. Carey J. Simonson, for his patience, guidance, inspiration, and exceptional mentorship throughout my Ph.D. studies.

I would like to thank my advisory committee members Prof. Donald Bergstrom, Prof. David Sumner, Prof. Huiqing Guo, and Prof. Lope G. Tabil for their valuable comments and constructive feedback.

I am thankful for the technical assistance I received from the departmental assistants Dr. M. Fauchoux, Mr. H. Reitenbach, and Mr. S. Reinink. The support received from Mr. B. Cole and Mr. D. Vessey (Engineering shops, College of Engineering), Mr. A. Kebernik, and Mr. J. Goertzen (Tempeff Inc., Winnipeg) is also appreciated.

Special thanks to Mr. H. Ramin, my fellow graduate student, for undertaking the numerical simulations and countless hours of discussions. I acknowledge my fellow graduate students and postdoctoral fellows, Dr. M. Shakouri, Dr. A. Olufade, Dr. S. Niroomand, Dr. A. Gurubalan, Dr. W.O. Alabi, Mr. P. Navid, Mr. D. Storle, Mr. A. Hossain, Mr. B. Xing, Mr. M. Torabi, Mr. A. Razmavar, Mr. T. Okolo, and Mr. M. Mostafa for their valuable feedback, comments, and support.

Thanks to my Dad, Mom, brother and sister and their spouses for your love and support. I also thank my friends, Mr. A. Thomas and Mr. S. K. Selvichan, for their endless words of motivation.

The financial assistance from a Dean’s Scholarship, Russell (Russ) Haid Memorial Award, Lauretta Schoenau Scholarship, Toyota Automotive Engineering and Safety Scholarship, Graduate Devolved Scholarship, and the Natural Sciences and Engineering Research Council of Canada (NSERC) is greatly appreciated.

DEDICATION

I dedicate this thesis to my wife, Chitra, and son, Siddharth.

Thank you very much for your love and support throughout my Ph.D. studies.

TABLE OF CONTENTS

LIST OF TABLES

LIST OF FIGURES

NOMENCLATURE

ACRONYMS

AAEE	Air-to-air energy exchanger
EX	Exchanger
FBR	Fixed-bed regenerator
HVAC	Heating, ventilation, and air-conditioning
LAU	Linear actuator unit
SEM	Scanning electron microscopy

SYMBOLS

A_{ht}	Total heat transfer area of the exchanger (m^2)
B_x	Systematic uncertainty
C_p	Specific heat capacity (J/kg·K)
Cr*	Heat capacity rate ratio
D_h	Hydraulic diameter (m)
f	Friction factor
h	Average convective heat transfer coefficient ($W/m^2 \cdot K$)
h_{ch}	Height of the exchanger flow channels (m)
h_e	Specific enthalpy (kJ/kg·K)
H_{EX}	Height of the exchanger (m)
H*	Operating condition factor
k	Thermal conductivity (W/m·K)
L_{EX}	Length of the exchanger (m)

M	Mass of the exchanger (kg)
m_a	Air mass flow rate (kg/s)
M_d	Mass of desiccant coating in the exchanger (kg)
n_p	Number of plates
n_f	Number of flow channels
NTU	Number of transfer units on supply or exhaust side
NTU_o	Overall number of transfer units
P	Period or recovery period (s)
P_{ch}	Corrugation pitch (m)
P_x	Random uncertainty
Re	Reynolds number
RH	Relative humidity (%)
T	Instantaneous temperature (°C)
$\overline{T}$	Average temperature (°C)
t	Time (s)
t_p	Plate thickness (m)
t_s	Student t-factor
U	Overall uncertainty
V_{ch}	Channel velocity (m/s)
V_f	Face velocity (m/s)
W_t	Instantaneous humidity ratio (kg_w/kg_a)
$\overline{W}$	Average humidity ratio (kg_w/kg_a)
W_m	Maximum moisture content in the desiccant (kg_w/kg_a)

GREEK SYMBOLS

β	Corrugation angle
Δ	Difference between supply inlet and exhaust inlet conditions
ε	Effectiveness (%)
ε_{CF}	Effectiveness of a counter flow heat exchanger (%)
ε_{cold}	Cold side effectiveness (%)
ε_{hot}	Hot side effectiveness (%)
ε_{l}	Latent effectiveness (%)
ε_{reg}	Effectiveness of regenerator (%)
ε_{s}	Sensible effectiveness (%)
ε_{t}	Total effectiveness (%)
λ	Longitudinal heat conduction factor
μ	Dynamic viscosity (Pa·s)
ρ	Density (kg/m^3)
τ	Time constant (s)

SUBSCRIPTS

a	Airflow
ads	Adsorption
ch	Channels
des	Desorption
g	Bulk air

ht	Heat transfer
i	Initial
1, 2, 3, and 4	Measurement station numbers in ASHRAE Std 84 (2020) at the inlets and outlets of the test section.
m	Matrix

CHAPTER 1

INTRODUCTION

1.1 MOTIVATION

Global energy consumption has increased due to rapid industrialization, economic growth, and increased standard of living. In Canada, about 30% of total energy is used in buildings, and more than 50% of this energy is attributed to heating ventilation and air-conditioning (HVAC) systems [1]. The building sector also accounts for about 17% of total greenhouse gas (GHG) emissions in Canada [2]. The space heating process in residential and industrial buildings is responsible for 62% and 56% of overall building energy consumption, respectively [3]. On the other hand, people in North America spent 90% of their life indoors [4] and it is already proven that indoor air quality (IAQ) and thermal comfort affect the occupant's productivity [5]. The government of Canada encourages the use of energy-efficient buildings and HVAC systems through the climate action incentive funds and by incorporating energy efficient measures in standards and building codes [6].

Over the past decades, building energy consumption has been reduced by optimizing the thickness of thermal insulation, developing new insulation materials, and applying energy exchangers [7]. However, many of these methods have several adverse effects on the thermal comfort, health, and productivity of occupants. The main factors influencing thermal comfort and IAQ are temperature, humidity, ventilation, the concentration of particles, and pollutant gases [8]. Air-to-air energy exchangers (AAEEs) reduce energy consumption and lower the load on HVAC systems without affecting ventilation rates while maintaining adequate IAQ. New energy-efficient HVAC systems often include AAEEs, which transfer the energy between building exhaust and supply airstreams.

The payback period of these systems can be as short as 2-4 years, depending on the climate and building [9].

Fixed-bed regenerators (FBRs) are AAEEs recently introduced in HVAC systems in North America. They have advantages like high effectiveness, low maintenance, and reliable operation in extreme weather conditions [10], [11]. There are several parameters used to quantify the performance of FBRs. Effectiveness is the most important among them, and it represents the energy recovery potential of the system. ASHRAE 84 and CSA C439-18 test standards [12], [13] have recently included guidelines for performance testing of FBRs. CSA C439-18 [13] is in informative Appendix and they are not in the normative standard. ASHRAE 84 [12] guidelines are normative but are based on expert opinion rather than through research and measured data. These tests require long-duration experiments, full-scale exchangers (prototyping costs), a high volume of conditioned airflow, large duct works, and laboratories. Hence, the main goal of this thesis is to develop a new test method to determine the performance of practical FBR units by testing a similar small-scale prototype, eliminating the disadvantages of the conventional test method. The proposed method is called “small-scale testing”, which can be used in the design and development of high performance FBRs for HVAC applications.

1.2 BACKGROUND

The operation of an HVAC system with an energy exchanger in buildings, and heat and moisture transfer process in different types of energy exchangers, are discussed in detail in the following subsections.

1.2.1 HVAC and energy recovery systems

HVAC systems are essential in buildings to maintain indoor air quality and thermal comfort. The schematic of an HVAC unit with an AAEE is shown in Figure 1.1. The supply fan provides

conditioned fresh air to the indoor space and the exhaust fan removes the stale air from the building. Depending on climatic conditions, heating or cooling systems are used to condition the incoming outdoor air. Filters are employed in HVAC units to prevent dust or aerosol particles from entering the building via supply air. Filters also protect the fans and exchangers from fouling. The AAEEs transfer energy between airstreams of the building exhaust and the fresh incoming outdoor air, thus reducing energy consumption.

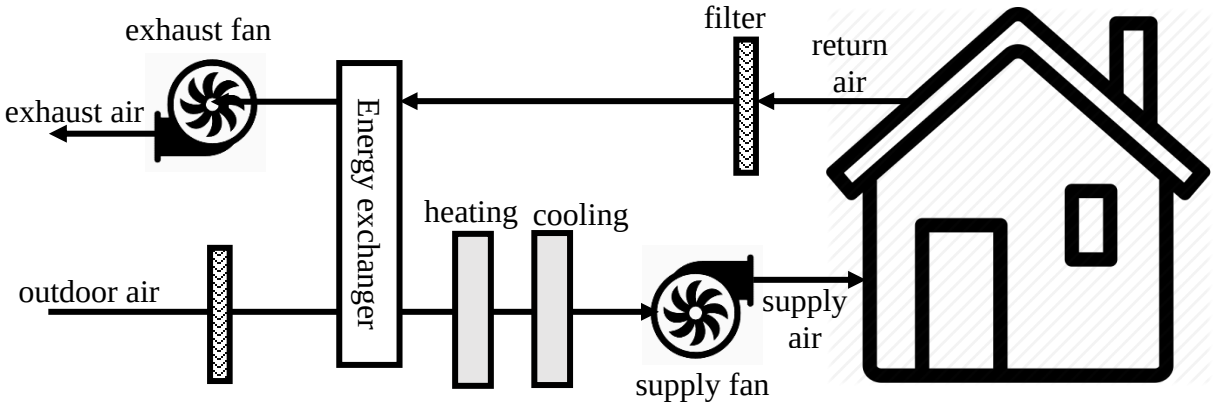

Figure 1.1. Schematic of an HVAC system with an energy exchanger delivering conditioned ventilation air to a building.

The AAEEs can be categorized into recuperators and regenerators based on their principle of operation. In recuperators, heat (and moisture) transfers continuously between the airstreams through a dividing wall. Plate, tubular, and membrane-type exchangers are examples of recuperators. Regenerators are storage-type exchangers where the outdoor air and return air alternatively flow through the exchanger, and they transfer the heat (and moisture) with the exchanger. Regenerators can be further divided into rotary wheels and fixed-bed regenerators (FBRs) based on their configuration. The principle and operation of recuperators and regenerators are discussed in following subsections.

1.2.2 Heat and moisture transfer in recuperators

Recuperators are used to transfer heat (and moisture) between two or more air streams at different temperatures (and humidity) which are in thermal contact [14]. In recuperators, the two airstreams are separated by a heat transfer surface, and ideally, they do not mix with each other. These exchangers are often known as direct transfer type exchangers. The recuperator's ability to transfer heat/moisture depends on the properties of the heat transfer surface. The conventional recuperators consist of impermeable metallic heat transfer surfaces, allowing only the exchange of heat between the airstreams. Recently, semi-permeable membranes have been introduced as heat transfer surfaces, enabling the simultaneous exchange of both heat and water vapor between the airstreams; hence, they have relatively higher energy performance than other types of recuperators [15]. The heat and moisture transfer process in a single flow channel of recuperators with impermeable and semi-permeable walls is presented in Figure 1.2.

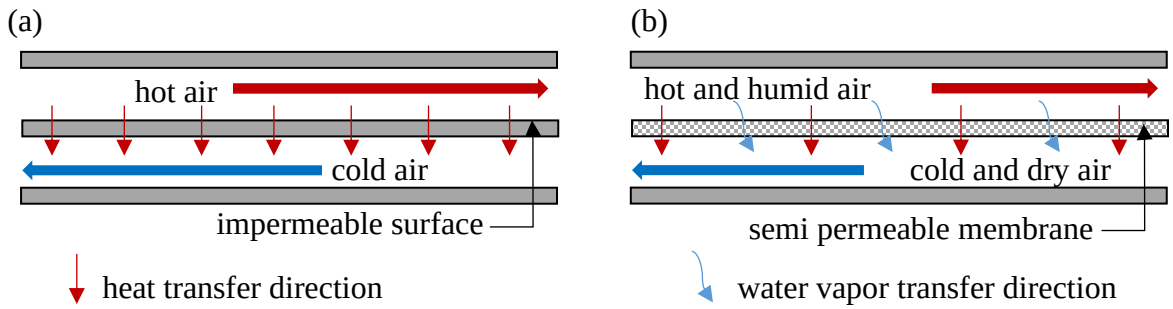

Figure 1.2. Schematic of heat (and moisture) transfer process in a single flow channel of (a) a conventional recuperative exchanger and (b) a membrane exchanger.

1.2.3 Heat and moisture transfer in regenerators

Regenerators consist of metal heat transfer surfaces, generally referred as an exchanger, matrix, or core. Typically, the exchangers consist of several flow channels made of materials having high specific heat and thermal conductivity (e.g., aluminum). Solid desiccants such as molecular sieves or silica gel may be coated on the surface of the exchangers to facilitate moisture transfer. A unique

advantage of desiccant-coated regenerators is the ability to transfer heat and moisture simultaneously between the airstreams.

A single airflow channel of a desiccant-coated regenerator is shown in Figure 1.3. When the hot and humid outdoor air (summer operation) flows through the regenerator, the heat and moisture are transferred to the substrate and the desiccants, respectively. The substrate (e.g., aluminum) stores thermal energy and the desiccants adsorb the moisture, as shown in Figure 1.3 (a); thus, the air comes out as cold and dry. After a specific time interval (called recovery period or period), the cold and dry exhaust air flows through the regenerator, and the heat and moisture will be released from the substrate and desiccants to airstreams (Figure 1.3 (b)), thereby increasing the temperature and humidity of the airstream. Similarly, during winter operation, the cold and dry outdoor air will be heated and humidified by the heat and moisture that was stored in the regenerator from the warm and humid exhaust air. This thesis deals with the heat and moisture transfer process on a specific type of regenerator called a fixed-bed regenerator (FBR). The principle, operation, and configuration of different types of regenerators are described in following subsections.

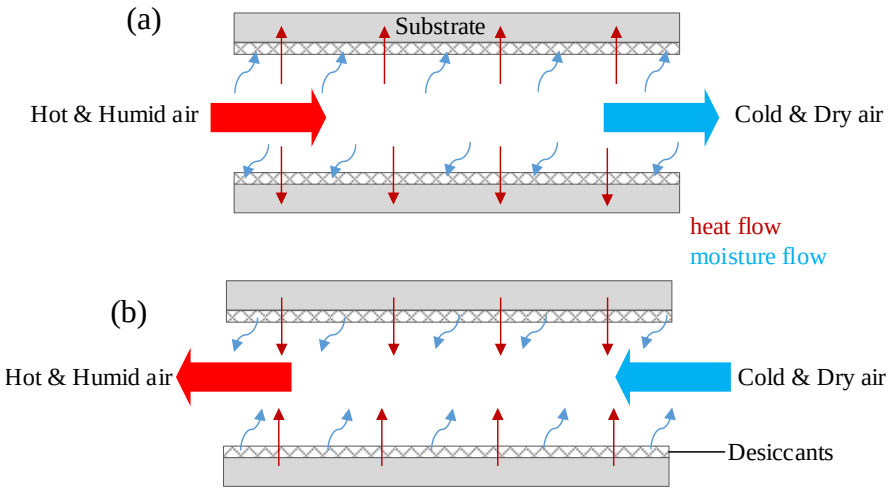

Figure 1.3. Schematic of heat and moisture transfer from (a) the airstream to the matrix and (b) the matrix to the airstream in a single flow channel of desiccant coated regenerators.

1.2.4 Fixed-bed regenerators

The schematic of an FBR with two stationary exchangers (EX1 and EX 2), dampers, and supply and exhaust fans is shown in Figure 1.4. The dampers are used to change the direction of airflow through the exchangers. The exchangers are preferably made of corrugated metal plates to achieve (i) a higher surface area for a given volume and (ii) a high convective heat transfer coefficient.

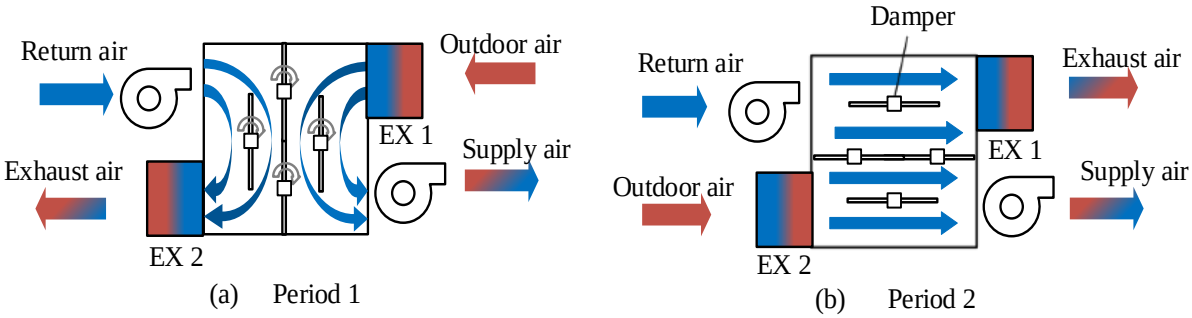

Figure 1.4. Schematic of FBRs with two stationary exchangers during (a) period 1 and (b) period 2.

One complete operational cycle of the FBR is comprised of two periods. During summer, hot and humid outdoor air flows through EX 1 and heat and moisture from the outdoor air get stored in the desiccant coated plates. As a result, the air at the FBR outlet (supply air) will be cold and dry. During the beginning of the second period, the damper rotates to 90° (Figure 1.4 b), redirecting the return air through EX 1, which releases the heat and moisture stored during the previous period to the airstream. Both the exchangers work simultaneously to provide conditioned air continuously. The typical recovery period of FBRs is about 40-60 s [11]. It should also be noted that FBRs are not developed with desiccant coating and currently they are used only as heat recovery regenerators.

FBRs have several advantages compared to rotary regenerators, such as they are relatively maintenance-free due to the absence of revolving components (except dampers), have a high

sensible effectiveness, and can operate at extreme winter conditions without any auxiliary defrosting techniques [10].

1.2.5 Rotary wheels

Rotary wheels (or regenerators) exchange heat and moisture between the return air from the building and the fresh outdoor airstreams. Like FBRs, rotary wheels consist of desiccant coated corrugated or sinusoidal flow channels, which can transfer both heat and moisture between the airstreams simultaneously. Based on their application, rotary wheels can be divided into heat wheels, energy wheels, and desiccant wheels. The heat wheels are used to transfer sensible energy only (heat recovery) and they do not have a desiccant coating. In contrast, the energy wheel consists of a desiccant-coated substrate, which allows simultaneous heat and moisture transfer. As the wheel rotates, the heat and moisture will be continuously transferred between supply and exhaust airstreams, as shown in Figure 1.5. The purpose of desiccant wheels is mainly to control the humidity of the incoming airstream (humidification/dehumidification). The main difference between energy wheels and desiccant wheels are that (i) energy wheels do not require any external energy for regeneration (passive device), whereas desiccant wheels consist of a dedicated regeneration section (active device), (ii) energy wheels consist of a uniform monolayer of desiccants to maintain relative humidity between 30-60% (depending on operating conditions), but the desiccant wheels are made of thick layers of desiccant coating to dry/humidify the incoming airstream.

When hot and humid air (outdoor air in the summer and return air in the winter seasons) flows through the wheel, the heat and moisture are transferred and get stored in the matrix. As the wheel rotates, the matrix will be exposed to the cold and dry air stream, and then the stored heat and moisture will be released, and this process repeats continuously. The usual rotating speed of rotary

regenerators varies from 5-20 rpm and can achieve sensible and latent effectiveness of 70-90% [16].

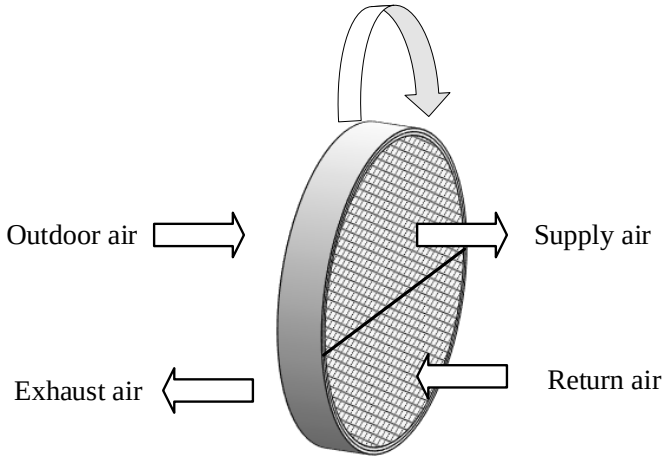

Figure 1.5. Schematic of a rotary wheel.

1.3 TESTING OF REGENERATORS

1.3.1 Full-scale testing

Testing of regenerators is necessary to understand their thermo-hydraulic performance. Various test standards have already been published and are available in the open literature, such as ASHRAE 84 [12] and CSA C439-18 [13]. The guidelines include the possible configuration of FBRs, locations of temperature and humidity sensors, requirements of instrumentation, and measurement methods. The testing of full-scale energy exchanger units following the guidelines provided in test standards is known as full-scale testing. Generally, the performance of regenerators for HVAC applications is determined as specified at AHRI 1060 test conditions [17].

Testing of FBRs is critical compared to other AAEEs since air temperature and humidity never attain a steady-state at the FBR outlet. Instead, the outlet air conditions reach a quasi-steady-state condition (i.e., they change continuously but periodically with time). Hence, instruments having

slow response cannot be used for outlet air temperature and humidity measurements. Temperature sensors generally have an acceptable response time, but the humidity sensor response is typically slower [18], and hence ASHRAE 84 [12] and CSA C439-18 [13] standards introduced a new technique for measuring the average humidity called the bag sampling method (BSM). In BSM, the outlet air is sampled over the entire duration of the period and the relative humidity of the sample is then measured after reaching an equilibrium condition. However, BSM has not yet been implemented or verified in the open literature. The BSM will be implemented, and the results will be verified, in this thesis.

1.3.2 Alternate test methods

An alternate test method for full-scale testing to predict the performance of rotary regenerators was developed by Abe et al. [19]. In this method, the time constants of the regenerator are measured by exposing it to a step-change in temperatures or humidity. Abe et al. [19] has shown that the time constants of each wheel depend on the thermo-physical and geometrical properties of regenerator and can be correlated to the wheel effectiveness. This method is called transient testing and it does not require the entire wheel for the experiments; instead, the response can be measured by testing a portion of the wheel [19]–[21]. This method has several advantages such as short duration for the tests, stationary facility, low uncertainty, and better control in test conditions compared to full-scale tests. Fathieh et al. [16] applied this methodology in a small-scale heat exchanger and showed that the performance of the rotary wheel could be predicted by testing a small-scale exchanger made of the same material as that of the wheel. This method can also be applied to FBRs; however, it is not a direct method, as it requires additional computations and a semi-empirical model to get results. It also has high uncertainty at some operating conditions due to the error propagation and cannot be applied for simultaneous heat and moisture transfer

experiments. Shakouri et al. [22], [23] and Wahab et al. [24] evaluated the moisture transfer performance of biomaterials using transient and direct testing methods with a small-scale parallel plate exchanger. The small-scale test method presented in this thesis is a direct method and is developed using FBR test conditions and geometry as an example. A comparison of full-scale testing, transient testing, and small-scale testing proposed in this thesis is presented in Table 1.1.

Table 1.1. Comparison of full-scale and transient test methods of regenerators with expected outcomes of small-scale test method (present study).

Parameter	Full-scale testing [16]	Transient testing [16]	Small-scale testing [present study]
Test time	5-10 hours	1 hour	1-2 hours
Equipment cost	$1-2,000,00	$50,000	$50,000
Space	200 m^2	100 m^2	100 m^2
Method	Direct	Indirect	Direct
Uncertainty	±5% (sensible)	±4-30% (sensible)	±5 % (sensible)
	±7% (latent)	±5-30% (latent)	±7% (latent)
Applicability	Sensible, latent, and total effectiveness	Sensible and latent effectiveness	Sensible, latent, and total effectiveness

1.4 LITERATURE OVERVIEW

An overview of the literature published in the area of regenerators for energy recovery is assessed and reported in this section. This literature survey aims to report the published papers on regenerators and the area of their applications. The literature was collected from Engineering Village (www.engineeringvillage.com) and ASME (https://asmedigitalcollection.asme.org/) databases. The keywords used for this search are “Rotary regenerator” and “Fixed-bed regenerator,” with a controlled (or limited) vocabulary of “heat and moisture transfer.” More detailed literature reviews related to each objective of this thesis are presented in the introduction sections of the corresponding chapters.

The first publications related to regenerators available in the open literature are from the 1950's and the initial publications were focused on explaining the principle of heat transfer, matrix geometry, temperature transients, analytical and numerical solutions, and the thermo-hydraulic performance at different operating conditions. Later, regenerators were widely investigated and analyzed specifically for gas turbine power plants, process industries, and desiccant and energy wheel applications. Figure 1.6 shows the publication statistics from 1950-2020, and it indicates an increasing trend in the number of articles from 1950's onwards. Even though many studies have focused on the system level (e.g., gas turbine power plants), studying the regenerator as a single component has the highest contribution in the available literature. It is also found that rotary wheels have been investigated more in detail for heat and mass transfer applications, and nearly four times more papers are published on rotary wheels than on FBRs.

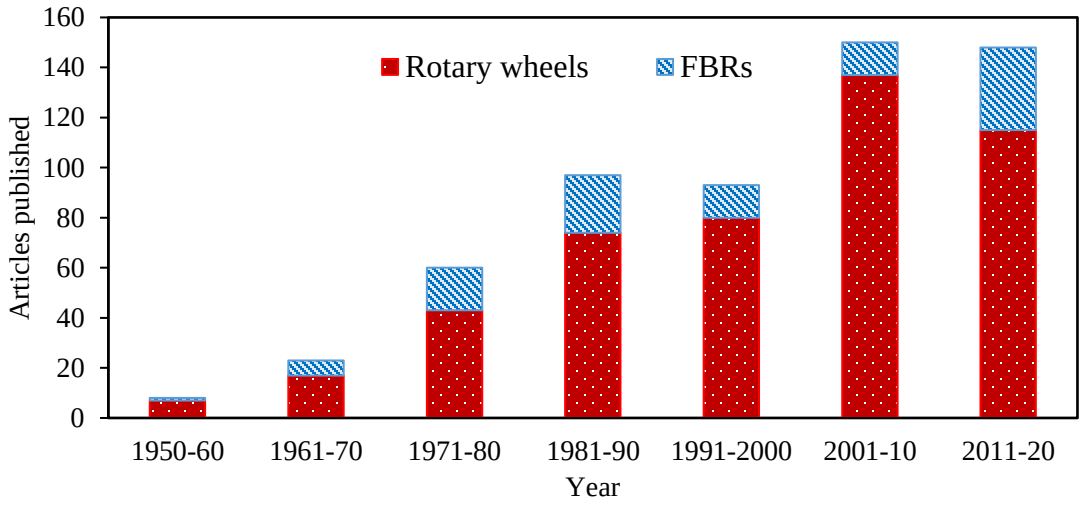

Figure 1.6. Publication statistics on FBRs and rotary wheels from 1950-2020.

Several correlations are available in the literature to predict the heat transfer performance or sensible effectiveness of regenerators. Among them, the Kays and London regenerator equation [25] is widely accepted and is accurate over a wide range of operating conditions. The correlations

proposed by Buyukalaca and Yilmaz [26], and Worse-Schmidt [27] cover the operating range excluded in the Kays and London correlation. All these correlations require the heat transfer surface area and the heat transfer coefficients. Correlations for heat transfer coefficients are available for many standard geometries such as parallel-plate, hexagonal and circular [28]. However, the validity of these equations is limited to their corresponding geometries. For the case of combined heat and moisture transfer process in regenerators, the effectiveness correlations developed by Simonson and Besant [29], [30] are widely accepted for determining sensible, latent, and total effectiveness [31], [32]. Some other practical correlations are also available for individual wheels with specific types of desiccant coatings [32].

The summary of published papers related to FBRs and rotary wheels in different areas is presented in Figure 1.7. For FBRs, the papers related to building energy recovery and air quality are included in the HVAC category, including system level and component level studies. The studies reported in process industries include packed-bed systems for adsorption/desorption of chemicals, gas separation process, and desiccant coated drying beds. The papers related to desiccant beds mainly consist of investigations to humidify or dehumidify the process airstream, desiccant materials selection, moisture transfer augmentation, and other parametric studies. The fundamental research category contains papers that report the principle, operation, and correlations of regenerators, and they contribute to the field of regenerators irrespective of their application. In rotary wheels, desiccant wheels are included as a separate category since many studies in this area have focussed on the dehumidification process in air conditioning systems.

In FBRs, about 27% of studies are from HVAC applications, and more than 85% of these papers are published after 2000, which indicates that FBR research has been accelerating in the past few

years. Nearly 30% of publications for both FBRs and rotary wheels are based on experiments, and more than 90% of these experiments were performed on full-scale exchangers.

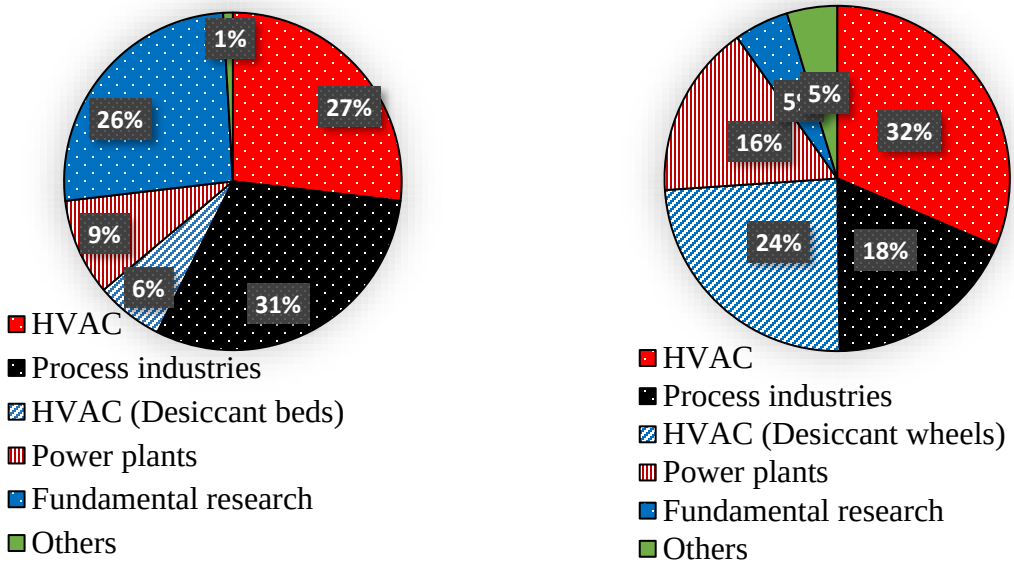

(a) (b)

Figure 1.7. Classification of published papers (1950-2020) based on the area of applications for (a) FBRs and (b) rotary wheels.

The limited experimental works for regenerators could be due to the challenges and limitations in setting up the full-scale test facility, instrumentation, and cost of experimentation. On the other hand, testing is essential for product development and material selection. Therefore, alternate test methods for performance testing would be beneficial.

1.5 OBJECTIVES

This Ph.D. study aims to develop new test methods to evaluate the performance of FBRs for HVAC applications. The hypothesis is that it is possible to predict the performance of a full-scale FBR by testing a similar small-scale FBR. This novel method of testing is called small-scale testing and has not been reported anywhere in the literature for FBRs. The small-scale testing methodology

has been successfully developed for the performance evaluation of liquid-to-air-membrane energy exchangers (LAMEEs) [33]. However, the methodology, measurement procedures, and data analysis are significantly different for FBRs since they are transient or quasi-steady state devices. The small-scale testing methodology enables researchers to test FBRs with different plate geometries and desiccant materials in a shorter time and lower cost per test. This Ph.D. research is a part of the collaborative project between Natural Sciences and Engineering Research Council of Canada (NSERC) and Tempeff Inc., Canada. Based on the requirements of Tempeff Inc., and the gaps identified from the literature survey, the specific objectives of the Ph.D. study are:

1. To develop an experimental facility to evaluate the sensible effectiveness of fixed-bed regenerators.
2. To develop testing methodologies to predict the sensible effectiveness and uncertainty of full-scale FBRs from small-scale tests.
3. To develop testing methodologies to predict the latent and total effectiveness and uncertainty of desiccant-coated full-scale FBRs from small-scale tests.

1.6 PUBLICATIONS

The findings from this work have been reported in four peer-reviewed journal papers, two conference papers, and one poster presentation. Two more graduate students have also worked on this collaborative research project with NSERC and Tempeff Inc., but the contributions of the author of this thesis (Easwaran N. Krishnan) to their publications are not included in this thesis.

1.6.1 Refereed journal papers

1. E. N. Krishnan, H. Ramin, M. Shakouri, L. D. Wilson, and C. J. Simonson, 2020, "Development of a small-scale test facility for effectiveness evaluation of fixed-bed regenerators," *Applied Thermal Engineering*, vol. 174, p. 115263.

2. E. N. Krishnan, H. Ramin, G. Annadurai, W. O. Alabi, and C. J. Simonson, 2021, "Methodologies for predicting the effectiveness of full-scale fixed-bed regenerators from small-scale test data," *Journal of Thermal Science and Engineering Applications*, vol. 13 no. 5, p. 051019.

3. E. N. Krishnan, H. Ramin, A. Guruabalan, and C. J. Simonson, 2021, "Experimental investigation on thermo-hydraulic performance of triangular cross-corrugated flow passages," *International Communications in Heat and Mass Transfer*, vol. 122, p. 105160.

4. E.N. Krishnan, H. Ramin, A. Gurubalan, and C.J. Simonson, 2022, "Experimental methods to determine the performance of desiccant coated fixed-bed regenerators," *International Journal of Heat and Mass Transfer*, vol. 182, p. 121909.

1.6.2 Conference papers and posters

1. E. N. Krishnan, H. Ramin, and C. J. Simonson, 2019, "Performance testing of fixed-bed regenerators for HVAC applications," *Proceedings of the 2nd Pacific Rim Thermal Engineering Conference*, Dec. 13-17, Hawaii, United States, pp. 1–5.

2. E.N. Krishnan, H. Ramin, A. Gurubalan, C.J. Simonson, 2020, "Influence of plate geometry on sensible effectiveness of FBRs," *Proceedings of the 7th Fluid Flow Heat and Mass Transfer Conference*, Nov 15-17 (virtual), pp. 1–5.

3. E. N. Krishnan, H. Ramin, and C. J. Simonson, 2019, “Fixed-bed regenerators for building energy recovery,” Engineering Graduate Community Council Conference, Sep. 12, Saskatoon, Canada (poster).

1.7 THESIS STRUCTURE

This thesis is written in the manuscript style and consists of five chapters and four appendices. Chapter 1 contains the introduction and background of the research. Chapters 2, 3, and 4 consists of manuscripts addressing the three objectives, and Chapter 5 summarizes the conclusions and proposed future works from this study [12].

The first objective of this thesis is addressed in Chapter 2 where the development, commissioning, and verification of the test facility are presented. The test results are verified with a validated numerical model and literature correlations. The facility is designed in such a way that it can test exchangers up to 1 m long and can be operated at face velocities ranging from 0.9- 2.5 m/s with air temperatures ranging from -25 to 60 °C. It is also shown that the facility can generate sensible effectiveness results within ±5%, which is the maximum allowed test uncertainty in conventional steady-state testing.

The physical dimensions and test conditions of small-scale exchangers tested in Chapter 1 are different from that of full-scale exchangers. Hence, Chapter 2 extends results to full-scale FBRs, which is the second objective of this thesis. The second objective of this thesis is formulated to develop new methods to extend the small-scale test data to full-scale FBRs, and this objective is addressed in Chapter 3 of the thesis. Two new methods called direct and predictive methods are developed, and the uncertainty associated with both test methods is quantified. The direct method requires only measured data from small-scale tests, whereas the predictive method uses a validated numerical model in addition to the test data. Furthermore, the heat transfer performance of various

corrugated plate FBRs have been investigated by applying these methods. The effects of plate geometry on the thermohydraulic performance of corrugated plate FBRs are presented in detail in Appendix B.

The third objective of this thesis is to develop test methods to evaluate the sensible, latent, and total effectiveness of desiccant-coated FBRs and this objective is addressed in Chapter 4. Test methods are developed to determine the effectiveness of FBRs when the airstreams have different humidities but equal temperatures (isothermal tests) or different temperatures (non-isothermal tests). As part of Chapter 4, the bag sampling method suggested by ASHRAE 84 [12], and CSA C439-18 [13] standards was implemented and verified.

Chapter 5 of this thesis contains conclusions, key contributions from this thesis and proposes some future research areas. The copyright permissions for the published manuscripts used in this thesis are included in Appendix A. A short communication paper related to the third objective is provided in Appendix B. The detailed uncertainty analysis of the effectiveness is presented in Appendix C. The practical challenges in implementing the BSM are discussed in Appendix D and the experimental data are reported in Appendix E.

The manuscripts in this thesis (Chapters 2, 3, and 4) are slightly modified to improve the readability of the thesis. Each manuscript includes a description of FBRs and the experimental test facility. In this thesis, the operation of FBRs is excluded from the introduction section of each chapter, and a detailed description of the test facility is included only in Chapter 2 (for heat transfer) and Chapter 4 (for mass transfer). The research contribution of each author is included in the overview section of every chapter. The thesis outline with the objective addressed in each chapter is shown in Figure 1.8.

CHAPTER 1: INTRODUCTION

CHAPTER 2: DEVELOPMENT AND COMMISSIONING OF TEST FACILITY
Objective #1: To develop a new experimental facility to evaluate the sensible effectiveness of fixed-bed regenerators.
Manuscript #1: Development of a small-scale test facility for effectiveness evaluation of fixed-bed regenerators.

CHAPTER 3: METHODOLOGY DEVELOPMENT FOR SENSIBLE EFFECTIVENESS EVALUATION OF FBRs
Objective #2: To develop testing methodologies to predict the sensible effectiveness and uncertainty of full-scale FBRs from small-scale tests.
Manuscript #2: Methodologies for predicting the effectiveness of full-scale fixed-bed regenerators from small-scale test data
Manuscript #3: Experimental investigation of thermo-hydraulic performance of triangular cross-corrugated flow passages (Appendix B).

CHAPTER 4: METHODOLOGY DEVELOPMENT FOR LATENT AND TOTAL EFFECTIVENESS EVALUATION OF FBRs
Objective #3: To develop testing methodologies to predict the latent and total effectiveness and uncertainty of desiccant-coated full-scale FBRs from small-scale tests.
Manuscript #4: Experimental methods to determine the performance of desiccant coated fixed-bed regenerators.

CHAPTER 5: CONCLUSION

APPENDICES

Figure 1.8. Thesis outline with the objectives and corresponding manuscript title for each chapter.

CHAPTER 2

TEST FACILITY DEVELOPMENT AND COMMISSIONING

2.1 OVERVIEW

This chapter explains the development and commissioning of a small-scale test facility to evaluate the sensible effectiveness of FBRs, which is the first objective of the Ph.D. thesis research. The design and operation of the test facility, instrumentation, and the construction of the small-scale exchanger are explained here in detail. The calibration of sensors and uncertainty analysis are also discussed. This chapter deals with the heat transfer (or sensible effectiveness) performance of FBRs, whereas the expansion of the test facility to include moisture transfer (latent effectiveness) will be discussed in Chapter 4. In this chapter, the experimental data from the test facility are verified using a validated numerical model and two design correlations from the literature. The test uncertainty is quantified through generalized uncertainty analysis for a wide range of FBR operating conditions.

The author of this thesis (Mr. Easwaran N. Krishnan) developed the test facility, conducted the experiments, and prepared the original draft manuscript. Mr. Hadi Ramin (Ph.D. student) has conducted the numerical analysis, Dr. Mohsen Shakouri (postdoctoral fellow) and Prof. Carey J. Simonson (supervisor) guided in the facility development and critically reviewed the manuscript. Prof. Lee D. Wilson contributed by proofreading the manuscript and providing guidance to clarify the discussions in the manuscript. The manuscript was published in Applied Thermal Engineering in June 2020.

Development of a Small-Scale Test Facility for Effectiveness Evaluation of Fixed-Bed Regenerators

(Published in Applied Thermal Engineering in June 2020)

Easwaran N. Krishnan, Hadi Ramin, Mohsen Shakouri, Lee D. Wilson, and Carey J. Simonson

2.2 ABSTRACT

Fixed-bed regenerators (FBR) transfer heat (and moisture) between supply and exhaust air streams in heating, ventilating and air conditioning (HVAC) systems to reduce building energy consumption. This chapter presents a new small-scale testing facility to evaluate the performance (i.e., sensible effectiveness) of FBRs for HVAC applications. The major contributions of this chapter are the development of a new small-scale experimental facility and methodology for testing FBRs, quantification of uncertainties, and verification of small-scale test data over a large range of FBR design conditions. A numerical model and two well-known design correlations are used to verify the results and testing methodology. The advantages of small-scale testing are that it requires a low volume of conditioned airflow, has low uncertainty, requires less exchanger material, and has a low cost per test. Moreover, the small-scale testing methodology of FBR would benefit heat exchanger manufacturers to perform detailed sensitivity studies and optimize the exchanger performance over a wide range of design and operating parameters prior to the fabrication of full-scale exchangers.

2.3 INTRODUCTION

Fixed-bed regenerators (FBRs) are air-to-air energy exchangers that have been widely used in various industries since 1950 [34]. The schematic and principle of operation of FBRs were described in detail in Chapter 1 (Section 1.2.3). Compared to other energy exchangers, FBRs have

low maintenance, high heat transfer effectiveness and they are less susceptible to frost formation during their winter operation [35].

Several numerical and analytical studies assessing the performance of FBRs for high-temperature applications such as power-plants [36], glass manufacturing [37] and process industries [38] have been reported in the literature. However, only limited literature has addressed the performance of FBRs experimentally in HVAC applications. Chang et al. [39] used an experimental approach to evaluate the performance of an FBR unit consisting of two desiccant-coated stationary wheels. They determined the optimum duration of heating and cooling periods required to obtain maximum total effectiveness using different desiccant composites [40]. Aristov et al. [41] developed an FBR with a single exchanger consisting of heat and moisture storage materials. Their device achieved sensible and latent effectiveness of 85 % and 60 %, respectively, during winter tests in Russia [42]. The possibility of using FBRs for room ventilation was evaluated numerically by Nizotsev et al. [43]. Their results were validated experimentally in a single-exchanger FBR test setup using a reversible fan. However, all the studies mentioned above require extensive test facilities and full-scale/practical FBR units.

The performance of FBRs in HVAC applications can be determined experimentally following the guidelines provided by the CSA C439-18 [13] standard with an acceptable range of uncertainties. Standard methods to evaluate the performance of full-scale FBRs are challenging since they require large laboratory spaces, a high volume of airflow rates and extensive testing facilities. Because of these limitations of the standard testing methodology of energy exchangers, researchers have been seeking alternative methods for performance evaluation and product development [19], [44].

Recent studies show that the performance of energy exchangers can be predicted by testing either a portion of the exchanger or a small-scale prototype [16]. Abe et al. [18] and Wang et al. [45] have studied the transient temperature and humidity response of an energy wheel subjected to temperature and humidity step changes. These tests were performed using only a portion of the wheel to predict sensible and latent effectiveness of full-size energy wheels from the transient temperature and humidity responses, respectively. Recently, Fathieh et al. [46], [47] predicted the performance of rotary heat wheels by measuring the transient response of a small-scale heat exchanger subjected to step changes in the inlet stream condition. Later, Shakouri et al. [22], [23] showed that the latent effectiveness of an energy wheel could be determined accurately from small-scale tests. Similar to rotary regenerators, the performance of liquid-to-air membrane energy exchangers (LAMEEs) has also been determined through testing a small-scale LAMEE exchanger [15]. Through LAMEE performance evaluation, Moghaddam et al. [33] developed a testing methodology for energy exchangers using nondimensional performance parameters such as the overall number of transfer units (NTU_o) and heat capacity rate ratio (Cr^*).

The main objectives of this chapter are (i) to introduce and describe the commissioning of a new test facility to determine the sensible effectiveness of FBRs at different operating conditions, (ii) to present the results of the tests of the small-scale facility, verify the testing methodology and quantify the uncertainty in sensible effectiveness at different operating conditions. The significance of temperature measurements, effects of operating conditions such as the duration of heating/cooling period and face velocity of the inlet airstreams on sensible effectiveness are also studied. Moreover, the results are presented using nondimensional performance parameters and compared with a numerical model and design correlations from the literature.

2.4 EXPERIMENTAL FACILITY

The principle of operation of the test facility, small-scale parallel-plate exchanger, and the experimental procedures will be presented in the following subsections.

2.4.1 Small-scale FBR test facility

The small-scale test facility is designed to simulate the cyclical operation of an FBR in practice by moving a small-scale exchanger between two air streams having different temperatures, as shown in Figure 2.1. The properties of air streams at inlet and outlet of the exchanger are measured to determine the performance of small-scale exchangers.

The test facility comprises a supply air system and a test section. The function of the supply air system is to provide conditioned air to the test section, where the small-scale exchanger is located. The test facility is capable of testing FBRs with different geometrical configurations.

2.4.1.1 Supply air system

Two centrifugal blowers are used to supply air to the test section. The air supply lines are made of circular PVC pipes with 50.8 mm (2 in.) inner diameter. The required flow rate is maintained by adjusting the rotational speed of blowers using variable voltage transformers. The airflow is measured by measuring the pressure drop across an orifice plate located in each supply line. The overall uncertainty in the airflow rate measurement is ± 1.4 %, mainly due to the ±12 Pa uncertainty in the pressure transducers. Honeycomb flow straighteners are installed at the blower outlets to enable accurate airflow rate measurements. The orifice plates and flow straighteners are designed in accordance with the ISO standard 5167-1 [48], [49]. A tubular electric heater is placed at one of the air supply lines to heat the incoming air stream. The heater is operated with a PID controller to maintain a constant temperature at the test section inlet with a maximum deviation of ±0.3°C. The supply air system can provide an airflow rate of 5.8-15 L/s in the range of -25 to 60˚C. For a

small-scale heat exchanger with a face area of 56 cm^2, the airflow rate corresponds to an exchanger face velocity of 0.8 to 2.5 m/s (157.5 to 492 fpm).

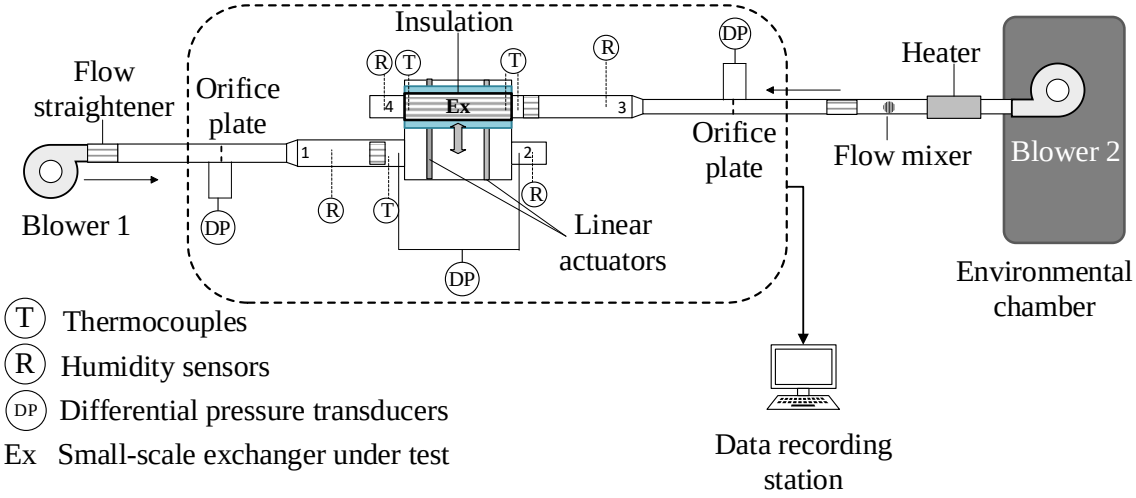

Figure 2.1. Schematic of the small-scale FBR testing facility.

The air supply lines are connected to rectangular plexiglass ducts with a length of 700 mm, shown as duct 1 and duct 3 in Figure 2.2. These ducts are 80 mm × 70 mm inner cross-section to match the size and geometry of test section to maintain uniform flow as the flow enters the test section. The two inlet ducts are insulated with 25.4 mm thick (1 in) extruded polystyrene to reduce heat losses/gains to/from the surrounding environment. A flow mixer and flow straightener are placed inside each supply line (duct 1 and duct 3) to obtain a uniform flow velocity and uniform temperature at the test section inlet. The flow straighteners are composed of hundreds of 2 mm × 3 mm rectangular channels with a length of 100 mm.

2.4.1.2 Test section

The function of the test section is to hold the small-scale exchanger and simulate the full-scale FBR operation by cycling the exchanger between the hot and cold airstreams. The test section includes an insulated PVC box, where the exchanger is located, and a linear actuator unit (LAU), as shown in Figure 2.2. The LAU is an integral part of the test section that consists of two linear

actuators, an air-filter pressure regulator and a solenoid valve controlled by a programmable phidget. It enables the exchanger to slide between the air streams and consequently subjects the exchanger to continuous hot and cold periods. The rails and cartridges of LAU are attached to the base of the test facility and exterior of the exchanger frame box, respectively. The LAU takes about 0.3 s to slide from one section to the other, and the sliding speed can be adjusted by controlling the air pressure to the actuators. The top face of the test section can be opened to add or remove the small-scale exchanger and can accommodate exchangers having a length of up to 1 m.

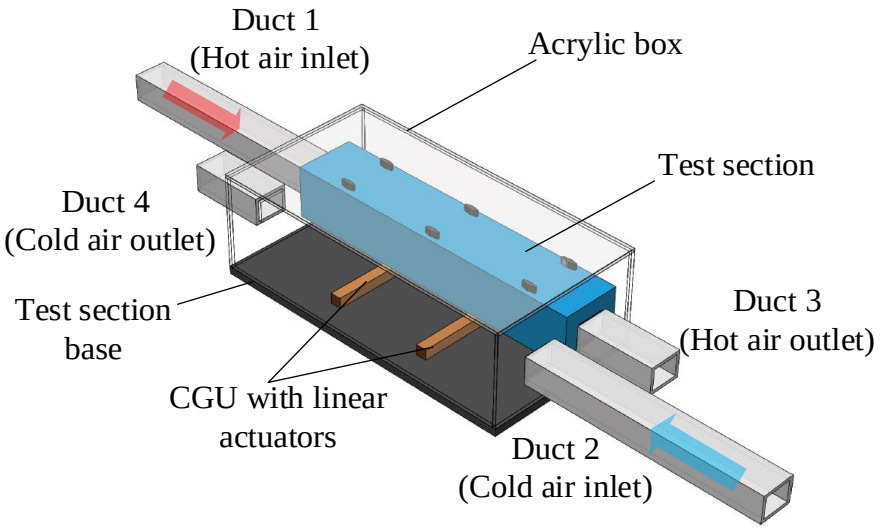

Figure 2.2. Schematic of the test section of small-scale FBR facility.

The chances of air leakages at the exchanger inlets and outlets are critical since the test section alternately slides between hot and cold airstreams. The leakage tests were performed at the beginning of experiments by injecting smoke through the blower suction side using a fog machine (Intertek, 1000 W) and visually observing the presence of smoke outside the test section. The leakages through the test section inlets and outlets were successfully eliminated by providing adequate rubber sealing at the test section outlets.

2.5 SMALL-SCALE EXCHANGER

A small-scale exchanger (or FBR) made of parallel aluminum plates is used in this study. The exchanger consists of 26 equally spaced aluminum plates, as shown in Figure 2.3. Each plate is 0.69 mm thick, 80 mm long, and 200 mm wide. A 3D printed ABS frame is used to hold the plates in an equally spaced (2.1 mm) parallel arrangement. Thus the 26 parallel plates assemble an FBR having 25 flow channels with a hydraulic diameter of 4.08 mm and a Reynolds number between 262 and 850. The geometrical and physical properties of the exchanger are given in Table 2.1.

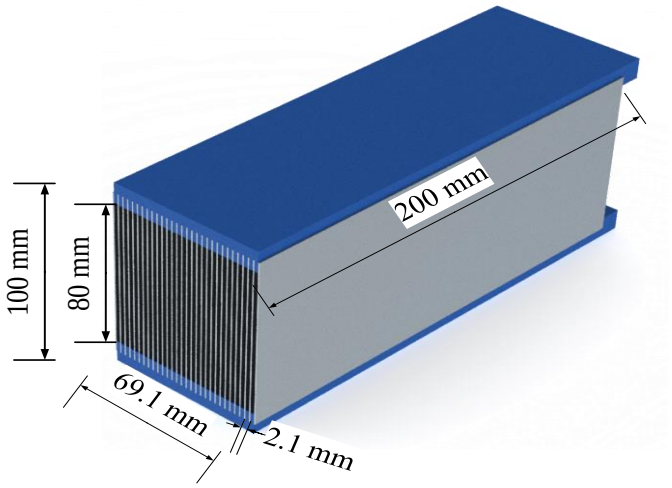

Figure 2.3. The small-scale parallel-plate exchanger geometry with supporting frames (the uncertainty of length measurements is 0.05 mm for all the reported values).

During a test, the exchanger is located inside the test section and is periodically exposed to conditioned (hot and cold) airstreams with the help of the LAU. When the test section is in line with the hot air stream, the exchanger stores heat from the hot air (hot period) and releases this stored heat when exposed to the cold air stream (cold period), simulating the operation of an FBR in practice. The exchanger is insulated using a 50.8 mm (2 in.) thick polystyrene insulation, which substantially reduces heat transfer between the exchanger and its surroundings.

Table 2.1. Geometrical details and thermophysical properties of the exchanger.

Channel				Plates			
Length (mm)	Height (mm)	Width (mm)	Hydraulic diameter (mm)	Thickness (mm)	Thermal conductivity (W/m·K)	Density (kg/m^3)	Specific heat (J/((kg·K))
200	80	2.1	4.08	0.69	162	2730	903

2.6 MEASUREMENTS AND DATA ACQUISITION

2.6.1 Instrumentation and uncertainty analysis

The uncertainties in sensible effectiveness are calculated from the uncertainties in temperature and flow rate measurements. The uncertainties in measurements are obtained by calibrating the thermocouples, humidity sensors and pressure transducers using a Hart Scientific dry-well temperature calibrator [50] (± 0.1˚C), Thunder Scientific humidity generator [51] (±0.5% RH) and a Druck precision portable pressure calibrator DPI 605 [52] (±1 Pa), respectively. During the calibrations, a sampling rate of 10 s is used to determine transients in temperature and humidity measurements. The uncertainties of the measured variables are presented in Table 2.2.

Table 2.2. Instrument specifications and calibration details.

Sl. No.	Instrument	Manufacturer/ type	Parameter	Capacity/ Calibration range	Total uncertainty
1	Thermocouples	T-type/ (0.08 mm wire dia.)	Temperature	20-60ºC	±0.2ºC
2	Pressure transducers	Validyne DP17	Differential pressure	0-860 Pa	±12 Pa
3	Tubular heater	Omega (electric resistance)	-	0-600 W	-
4	Humidity sensors	Honeywell (capacitive type)	Relative humidity	15-85% at 25ºC and 35ºC	±1.5 %

The total uncertainty (U) in a measurement is determined from systematic (B_x) and random (P_x) uncertainties for 95% confidence intervals according to the ASME PTC standard 19.1 [53]:

$$U = \sqrt{P_x^{\,2} + B_x^{\,2}}. \tag{2.1}$$

The random uncertainties (P_x) associated with all measured parameters are determined using Eq. (2.2)

$$P_x = \frac{t_s \cdot SD}{N}, \tag{2.2}$$

where t_s is the student t- factor at a 95% confidence interval for a degree of freedom of (N-1), and SD is the standard deviation of the measurements. Calibration and data reduction errors are included in the systematic uncertainty. The overall uncertainty in sensible effectiveness is determined using the method of uncertainty propagation rules as follows [54],

$$U_R = \left[\sum_{i=1}^{j} \left(\frac{\partial R}{\partial p_i} U_{p_i}\right)^2\right]^{0.5}, \tag{2.3}$$

where U_R, U_{p_i}, and $\partial R / \partial p_i$ are the overall uncertainty, uncertainty associated with measurement property P_i, and the sensitivity coefficient of measurement property P_i, respectively.

2.6.2 Temperature measurements and thermocouples arrangement

Since the exchanger periodically moves between two air streams, the outlet temperature continuously varies. Therefore, the sensors must respond quickly to obtain accurate measurements. Calibrated T-type thermocouples are arranged in two different locations at the exchanger inlet and outlet for precise temperature measurements. The locations and configuration of thermocouples in the test facility are shown in Figure 2.4. Four thermocouples, which are 5 mm away from the exchanger, are placed in the test section so that the sensors can move with the exchanger and are hence named exchanger sensors. Therefore the exchanger sensors measuring the temperature of

the air at the exchanger inlets during one period measure the exchanger outlet air temperature in the adjacent period.

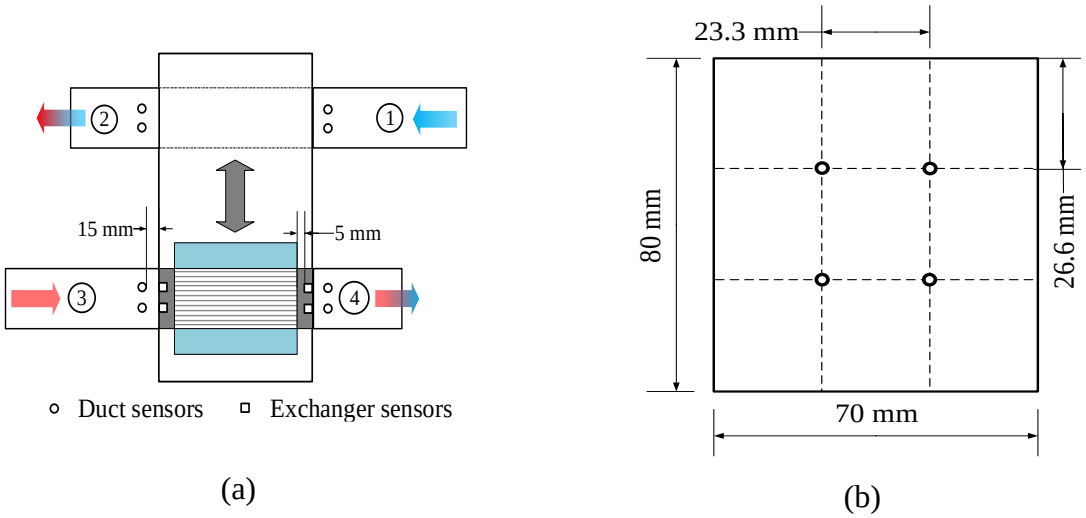

Figure 2.4. Schematic of the test facility showing thermocouples locations (a) and their spatial arrangements (b) at the exchanger inlet and outlet.

Additionally, four thermocouples are placed in each inlet and outlet duct, named duct sensors, which are stationary and exposed to the same kind of air stream always. For example, the sensors located in duct 4 will measure the exchanger outlet temperature during the hot period and measure the hot air inlet temperature during the cold period. The measured temperatures are recorded using a computer-controlled National Instruments data acquisition system (Chassis: NI SCXI-1000, modules: NI SCXI 1102, terminal blocks: NI SCXI-1303).

2.7 EXPERIMENTAL PROCEDURES

As described above, the supply air system provides the required airflow through the test section. One of the air streams is heated to 39 ±0.2°C (hot air stream), and the other stream is kept at room temperature (cold air stream). Before every experiment, the conditioned air passes through the test section for at least one hour. When the variations in temperatures and flow rate measurements

become less than their measurement uncertainties for a period of 30 min, it is assumed that the ducts and test section reach the steady-state condition. Then, the exchanger movement facilitates using the LAU. The LAU slides the exchanger from one air stream to another in a very short time (approximately 0.3 s). After a series of cyclic exposures to hot and cold airstreams, the exchanger attains a quasi-steady state where the outlet temperature profile remains unchanged within the uncertainty of the measurements for every period. The performance of FBR is then evaluated from quasi-steady-state outlet temperature profiles.

2.8 NUMERICAL MODEL

In this study, a 1-D numerical model is used to verify the measured data from the small-scale FBR. The model considers laminar and incompressible flow through a representative parallel plate channel of the FBR (as shown in Figure 2.5). The air and matrix material properties, and the mean air velocity are assumed to be constant, and the model solves for bulk mean temperature of the air and the matrix (aluminum plate). The energy equations governing the heat transfer in one channel are [55]:

$$\rho_g C_{P_g} A_g \frac{\partial T_g}{\partial t} + V_{ch} \rho_g C_{P_g} A_g \frac{\partial T_g}{\partial x} + h \frac{A_{ht}}{L_{ch}} \left(T_g - T_m\right) = 0 \tag{2.4}$$

$$\rho_m C_{P_m} A_m \frac{\partial T_m}{\partial t} - h \frac{A_{ht}}{L_{ch}} \left(T_g - T_m\right) = \frac{\partial}{\partial x}\left(k_m A_m \frac{\partial T_m}{\partial x}\right), \tag{2.5}$$

where T, x, ρ, C_p, k, V_{ch}, h, L, and t are temperature, axial coordinate, density, specific heat capacity, thermal conductivity, mean airflow velocity, convective heat transfer coefficient, length of channel and time, respectively. The cross-sectional area of the air channel, heat transfer surface area and cross-sectional area of the matrix sheet are denoted as A_g, A_{ht} and A_m, respectively. The subscripts 'g' and 'm' are used to refer to the bulk air and matrix properties, respectively. The energy equation for the airflow includes the storage, advection, and convection, while the axial heat

conduction is neglected because Pe > 50. The energy equation for the matrix includes storage, convection, and axial conduction. The axial conduction term is particularly important for FBRs because they have thick matrix plates when compared to energy wheels. The assumptions used in the numerical model were reported and discussed in [56].

The boundary conditions are presented in Eqs. (2.6) and (2.7) must be satisfied for the supply and exhaust temperature [57].

$$T_g(0) = T_{s,i} \text{ (hot period)} \tag{2.6}$$

$$T_g(L) = T_{e,i} \text{ (cold period)} \tag{2.7}$$

Furthermore, the heat transfer at the ends of the channel is assumed to be negligible [57], i.e.

$$\left.\frac{\partial T_m}{\partial x}\right|_{x=0} = \left.\frac{\partial T_m}{\partial x}\right|_{x=L} = 0. \tag{2.8}$$

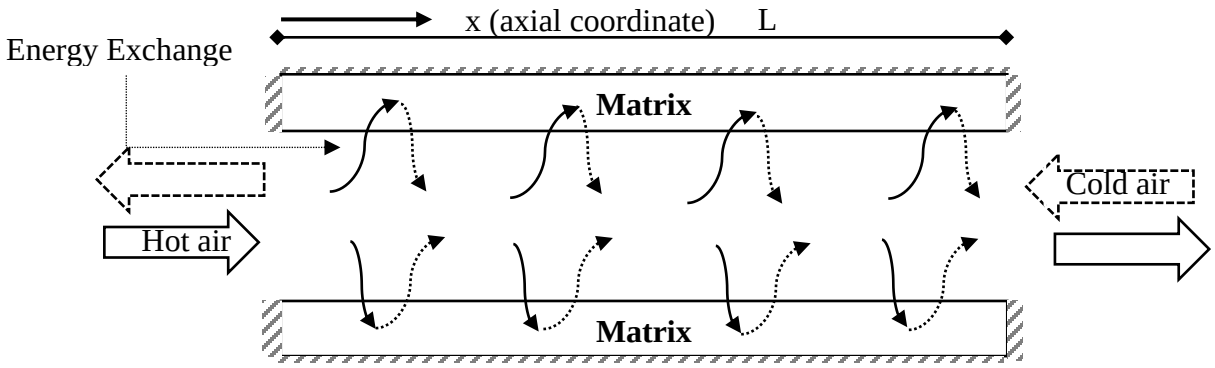

Figure 2.5. Schematic of the numerical domain for heat transfer in the FBR channel (solid line for the hot period (hot air) and the dashed line for the cold period (cold air)).

The transient transport equations (Eqs. (2.4) and (2.5)) for the conservation of energy in the airflow and matrix are discretized using a finite-volume method [58]. The upwind differencing and central differencing schemes are used to approximate the convection/diffusion terms in the airflow and the matrix, respectively. The resulting algebraic equation for the airflow is solved using a Gauss-

Seidel iteration technique, where the Tridiagonal Matrix Algorithm (TDMA) is used to solve the energy equation in the matrix.

2.9 PERFORMANCE PARAMETERS AND EMPIRICAL CORRELATIONS

In this section, the performance parameters of FBRs and the empirical correlations used to validate the small-scale testing methodology will be presented and discussed in detail.

2.9.1 Performance parameters

Sensible effectiveness is one of the main parameters to assess the performance of regenerators. The sensible effectiveness of an FBR is defined as the ratio of the heat transfer rate between the exchanger and airstreams to the maximum possible heat transfer rate. The heat capacity rate of the working fluid, thermal properties of the exchanger materials, heat transfer area, and duration of heating and cooling periods are the factors that affect the sensible effectiveness. Equations. (2.9) and (2.10) are used to determine the sensible effectiveness of a small-scale FBR for the hot and cold periods, respectively [14]. Theoretically, the effectiveness values determined using Eqs. (2.9) and (2.10) must be equal if there is no heat interaction between the exchanger and surroundings. However, in experiments, the measured data may vary due to experimental uncertainties, even if there is no heat loss/gain from outside. Therefore the average of ε_{hot} and ε_{cold} is considered as the sensible effectiveness of small-scale FBR, which also reduces the experimental uncertainty [29]

$$\varepsilon_{hot} = \frac{C_1}{C_{min}} \frac{(T_1 - \overline{T}_2)}{(T_1 - T_3)} \tag{2.9}$$

$$\varepsilon_{cold} = \frac{C_3}{C_{min}} \frac{(\overline{T}_4 - T_3)}{(T_1 - T_3)} \tag{2.10}$$

where T_1 and T_3 are the temperatures of the hot and cold inlet air streams, and $\overline{T}_2$ and $\overline{T}_4$ are the time-averaged air temperatures at the exchanger outlets, respectively (Figure 2.4). C_1 and C_3 are the heat capacity rates of the hot and cold airstreams and C_{min} is the minimum of C_1 and C_3. Since the outlet temperature of the airstreams varies with time, the time-averaged outlet temperatures are determined using Eq. (2.11) [14].

$$\overline{T} = \frac{1}{P}\int_0^P T(t)dt, \tag{2.11}$$

where $T(t)$ is the instantaneous outlet air temperature and P is the total period.

The design and operating condition variables such as the physical dimensions of the exchanger, face velocity and cycle period in small-scale experiments are different from that of practical FBRs. However, the sensible effectiveness can be represented as a function of two dimensionless parameters the number of transfer units (NTU_o) and the heat capacity rate ratio (Cr^*) which includes the effects of these design and operating condition variables [14], i.e., $\varepsilon = f(NTU_o \text{ and } Cr^*)$,

$$NTU_o = \frac{UA_{ht}}{C_{min}} \tag{2.12}$$

$$Cr^* = \frac{(\dot{m}C_p)_{matrix}/P}{(C_{min})_{air}}, \tag{2.13}$$

where U is the overall heat transfer coefficient, A_{ht} is the area of heat transfer, and C is the heat capacity rate, respectively.

2.9.2 Empirical correlations

The operation of the test facility and the testing methodology will be verified by comparing the test results with two effectiveness correlations proposed by Kays and London [14] and Buyukalaca and Yilmaz [26], [59]. The Kays and London correlation is valid when NTU_o and Cr^* are greater

than or equal to one, whereas Buyukalaca and Yilmaz's correlation is valid for the entire range of NTU_o and Cr^*. However, the latter was developed based on experiments performed at low NTU_o and Cr^*; therefore, it is expected to be more accurate at lower values of NTU_o's and Cr^*.

Kays and London's correlation was developed by including two correction factors to the recuperative heat exchanger effectiveness by considering the effects of the period ($\emptyset$) and longitudinal heat conduction (φ) on the heat transfer rate as shown in Eq. (2.14),

$$\varepsilon_{reg} = \varepsilon_{CF} \cdot \emptyset \cdot \varphi, \tag{2.14}$$

where, ε_{CF} is the effectiveness of a counter-flow heat exchanger and, for the same hot and cold air heat capacity rate, ε_{CF} can be determined using:

$$\varepsilon_{CF} = \frac{NTU_o}{1+NTU_o}. \tag{2.15}$$

The correction factors $\emptyset$ and φ are determined using Eqs. (2.16) and (2.17).

$$\emptyset = 1 - \frac{1}{9\,(Cr^*)^{1.93}} \tag{2.16}$$

$$\varphi = 1 - \frac{C_\lambda}{2-C^*}, \tag{2.17}$$

where

$$C_\lambda = \frac{1}{NTU_o(1+\lambda\theta)/(1+\lambda \cdot NTU_o)} - \frac{1}{(1+NTU_o)}, \tag{2.18}$$

$$\theta = \left(\frac{\lambda \cdot NTU_o}{1+\lambda \cdot NTU_o}\right)^{0.5} \tanh\left\{\frac{NTU_o}{[\lambda \cdot NTU_o/(1+\lambda \cdot NTU_o)]^{0.5}}\right\} \tag{2.19}$$

$$\lambda = \frac{K_m \cdot A_m}{L_{EX} \cdot C_{min}}, \tag{2.20}$$

where λ is known as longitudinal heat conduction factor and K_m, A_m and L_{EX} are the thermal conductivity, matrix cross-sectional area, and length of the exchanger, respectively.

Correlations for the longitudinal heat conduction factor K_m agree within ±1% with the results of Bahnke and Howard's numerical solution [60] for $0 \leq \lambda \leq 0.08$.

The correlation for sensible effectiveness proposed by Buyukalaca-Yilmaz is given as [26], [59]:

$$\varepsilon_{reg} = \frac{Cr^*}{\left\{1+3\cdot\left(\frac{NTU_o\cdot Cr^*}{1+NTU_o}\right)^2+\left(\frac{NTU_o\cdot Cr^*}{1+NTU_o}\right)^4\right\}^{0.25}} \cdot \tag{2.21}$$

In small-scale experiments, the flow within the exchanger is laminar. Therefore, the value of the convective heat transfer coefficient was taken from the literature based on the channel aspect ratio. The hydrodynamically and thermally developing lengths for the lowest face velocity (V_f = 0.8 m/s) are ${}^{X_{h,FD}}/_{L} = 0.2$ and ${}^{X_{th,FD}}/_{L} = 0.14$, which indicates that the flow becomes hydrodynamically and thermally fully developed only after 20% and 14 % of the total exchanger length, respectively. Therefore the correlation of Nusselt number for simultaneously developing flow [28] was utilized to account the effects of both hydrodynamically and thermally developing flow on the heat transfer coefficient.

2.10 RESULTS AND DISCUSSION

In this section, the test results at different operating conditions along with their uncertainty analysis are presented. The temporal and average outlet temperatures are analyzed and verified with the numerical model and correlations from the literature.

2.10.1 Transient response of temperature sensors

The response time of instruments indicates how fast they can respond to a change in the input conditions and is quantified using time constant. For the case of thermocouples, the time constant refers to the time required for it to attain 63.2% of the final temperature value when exposed to a step-change in the inlet temperatures. Three time constants are required to reach 95% of the final temperature and five time constants are required to reach 99% of the final temperature. Figure 2.6

provides the transient response of the temperature sensors (i.e., thermocouples) when they are exposed to a step-change in temperature. The sensors located at the test section (Exchanger sensors) are used to measure the time constants. It should be noted that these experiments are performed without placing the exchanger in the test section as the exchanger also affect the response of the temperature sensors. In this experiment, the inlet temperature was changed through 12°C and the face velocity of the airstreams was maintained at V_f = 1.8 m/s. The experiment data were correlated with an exponential function shown in Eq. (2.22) using the trust region optimization algorithm with MATLAB R2013a. The least-squares technique was used to fit the test data with calculated temperatures. The time constant (τ) values and the coefficient of determination (R^2) are reported in Table 2.3 and the high value of R^2 confirms the precise fitting of exponential function to the experiment data.

$$f(t) = \begin{cases} 1 - e^{-\frac{t}{\tau}} \\ e^{-\frac{t}{\tau}} \end{cases}, 0 \leq t \leq \infty \text{ (for step increase and decrease)} \quad (2.22)$$

Table 2.3. Thermocouple time constant data for a step change in inlet temperature.

	ΔT_{step}	Time constant τ, (s)	R^2
Step increase	12 ± 0.2°C	2.1	0.981
Step decrease		2.1	0.981

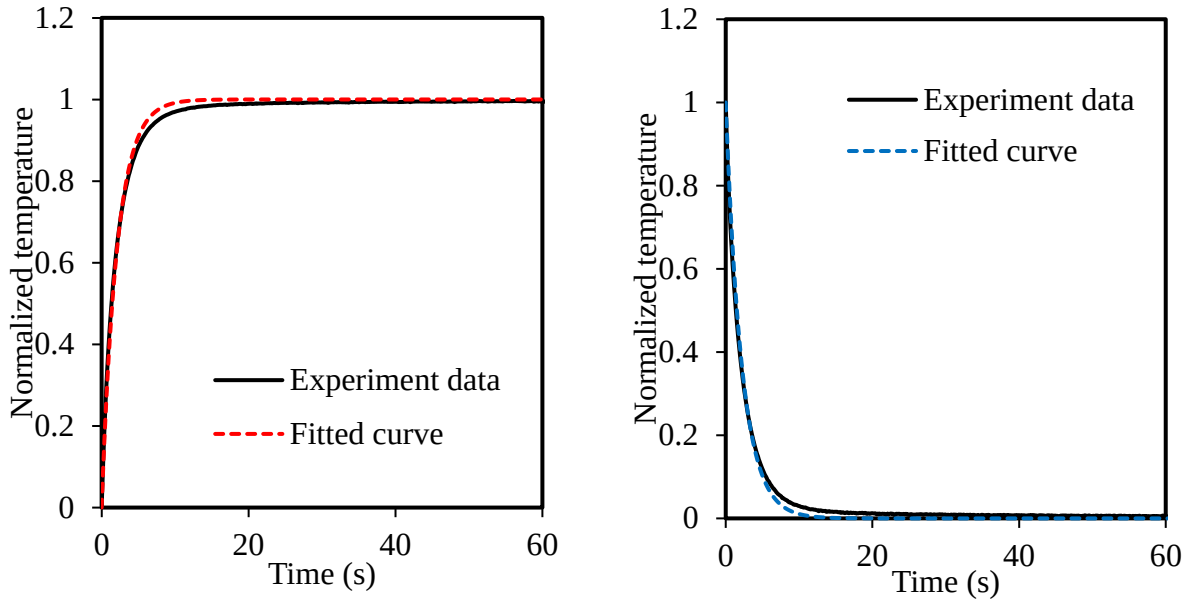

Figure 2.6. Normalized outlet temperature profile with the theoretical fitted curve for a step (a) increase and (b) decrease in the inlet temperature (ΔT_{step} = 12°C, V_f = 1.8 m/s).

2.10.2 Temperature measurements and sensible effectiveness

During the experiments, the temperatures at the FBR outlets vary with time and reach a periodic profile when the experiment reaches a quasi-steady state. The FBR outlet temperature profiles measured with the exchanger sensors and duct sensors are shown in Figure 2.7 for hot and cold periods of 60 s and 15 s. During the hot period, the exchanger stores heat from the air (i.e., the cold matrix cools the hot air), and thus the air temperatures at the outlet are lower than at the inlet. The maximum heat transfer occurs at the beginning of the period and the outlet air temperature increases gradually as the cold exchanger is heated by the hot air. During the cold period, the exchanger releases the stored heat to the incoming cold air stream, resulting in heating of the cold inlet air.

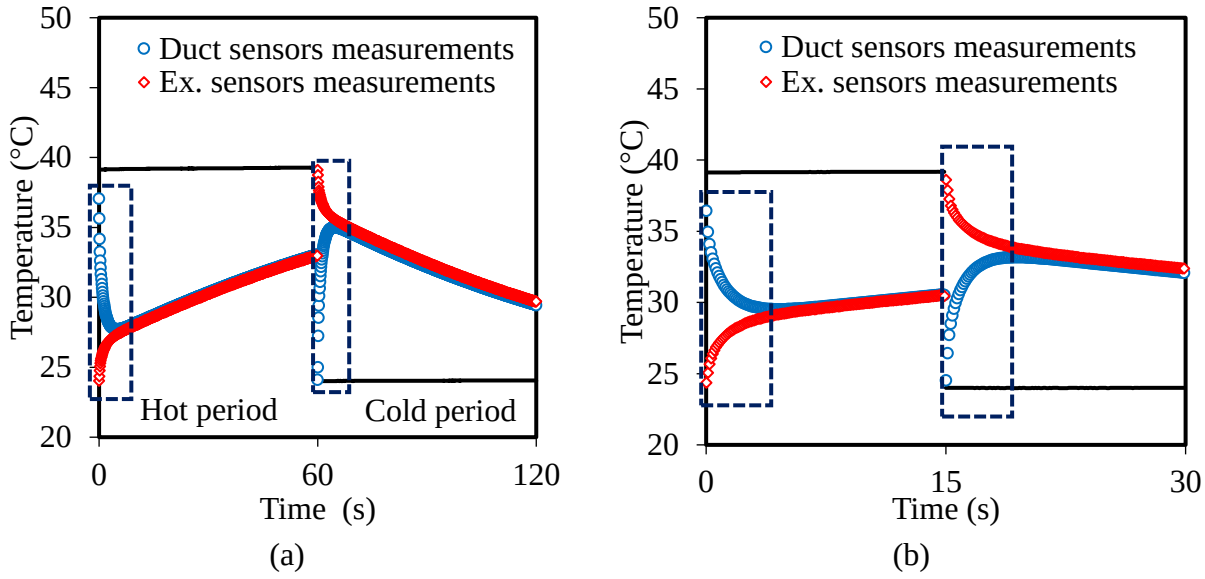

Figure 2.7. Comparison of FBR outlet temperature profiles measured using duct sensors and exchanger sensors for hot and cold periods: (a) 60 s ($Cr^* = 1.12$), and (b) 15 s ($Cr^* = 4.45$) (Face velocity, $V_f = 1.5$ m/s, $NTU_o = 2.25$).

Figure 2.7 shows that the temperature measured by the ducts and exchanger sensors are different at the beginning of each period but approach the same value at the end of each period. This deviation in the initial transient region (highlighted with dashed lines in Figure 2.7 (a) and (b)) is due to the transient response of the thermocouples and the conditions at which the thermocouples were exposed during the previous period. Prior to the hot period shown in Figure 2.7 (a) (0-60 s), the duct sensors were exposed to a hot airstream and the exchanger sensors were exposed to a cold airstream. Therefore, these sensor measurements start from the inlet hot and cold airstream temperatures, respectively. When the period is 60 s, the duct and exchanger sensors take only 10% of the period to reach the same value within the experimental uncertainty. By comparison, when the period is 15 s, the sensors take approximately 35% of the period to reach the same value.

The sensible effectiveness during the hot and cold periods are determined from the average temperature over a period; Eqs. (2.10) and (2.11) can be defined over any period. The sensible effectiveness calculated from the hot and cold period temperatures as a function of cycle number

is shown in Figure 2.8. At the beginning of the experiment, the exchanger is at room temperature, the heat transfer rate between the hot air and the exchanger is greater, as compared to that of the cold air and exchanger due to the large temperature difference between the exchanger and the hot airstream. Slowly, the exchanger attains a quasi-steady state where the heat transfer between both the airstreams and the exchanger become the same. The exchanger is assumed to operate in a quasi-steady state when the difference in hot side and cold side effectiveness is less than the uncertainty in sensible effectiveness for at least ten cycles.

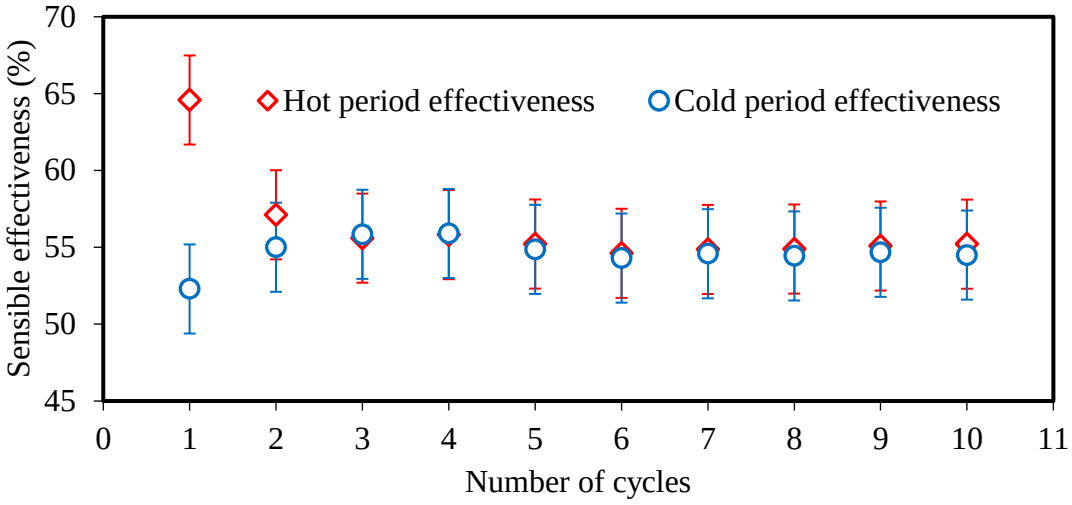

Figure 2.8. Sensible effectiveness during hot and cold periods as a function of the number of cycles ($NTU_o = 2.25$, $Cr^* = 0.75$).

The sensible effectiveness of the FBR determined using the exchanger and duct sensors after attaining a quasi-steady state is shown in Figure 2.9. As explained previously, the transient response of the thermocouple causes incorrect temperature measurements at the beginning of each period, resulting in significant deviations in sensible effectiveness for periods less than 60 s.

For a period of 60 s, the sensible effectiveness determined from both the duct and exchanger sensors agrees within the experimental uncertainty bound. By comparison, the sensible effectiveness determined from duct sensors and exchanger sensors has a 10% difference when the

exchanger operates with a 10 s period. Therefore, the temperature measurements in FBR experiments become more critical for short operating periods.

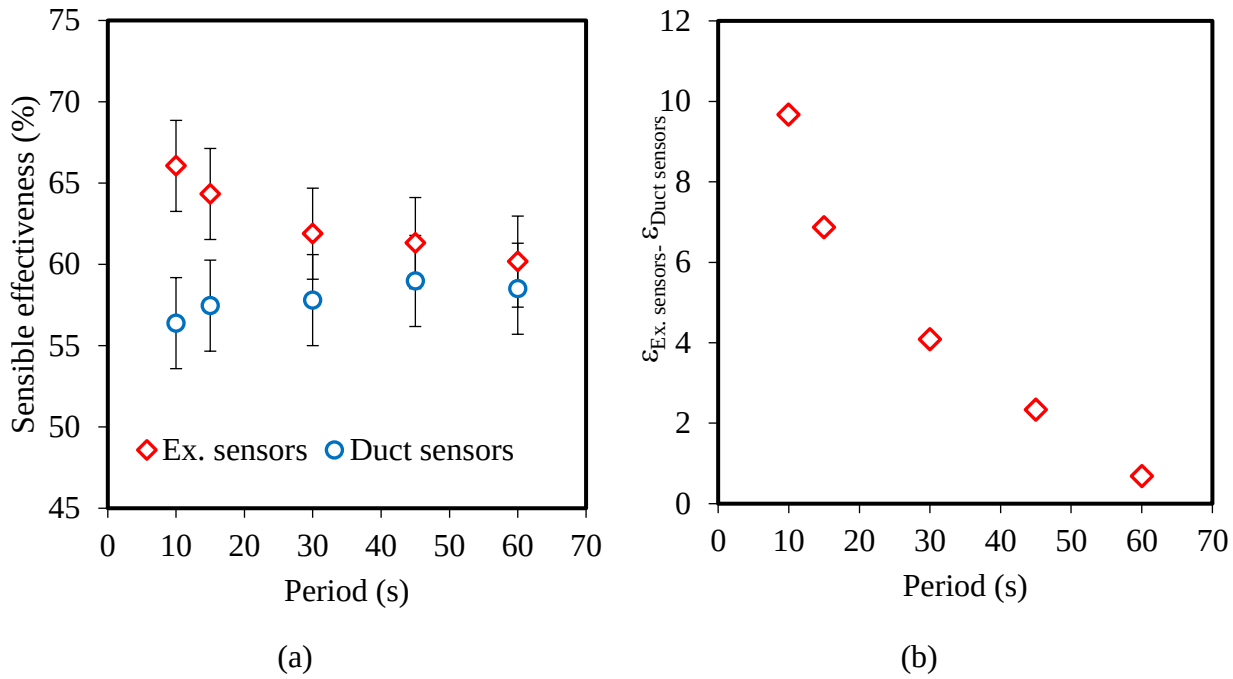

Figure 2.9. (a) Comparison of sensible effectiveness determined from exchanger and duct sensor measurements and (b) their difference at different periods (Face velocity, V_f = 1.5 m/s, NTU_o = 2.25).

Based on the experimental and numerical temperature profiles for several operating conditions (NTU_o 1.5 – 5 and Cr^* 1.5 – 7), it is found that the FBR outlet temperature varies linearly with time. Therefore, the initial temperature measurements are corrected by fitting a linear curve (linear backfit) on the final measurements in each period. The coefficient of determination R^2 is maintained to be at least 0.99. A sample temperature correction procedure is carried out on the exchanger sensor measurements and is shown in Figure 2.10 (a) and a comparison between the corrected experimental (Ex. corrected) and the numerical temperature profiles are shown in Figure 2.10 (b).

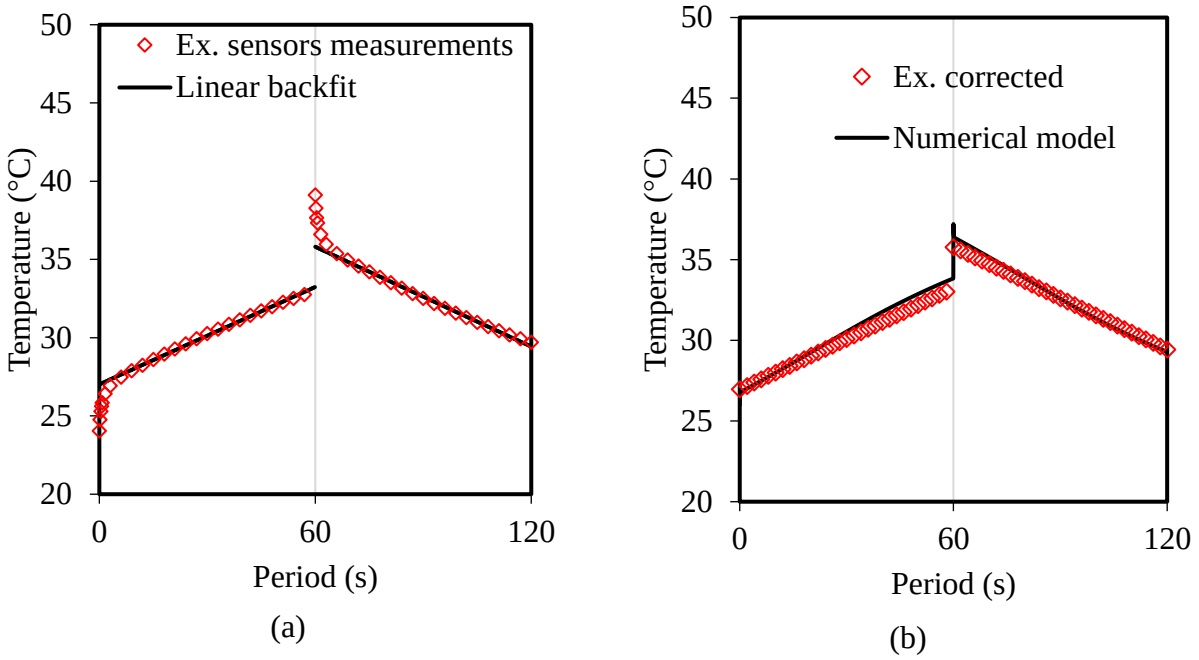

Figure 2.10. (a) Temperature profile correction on exchanger sensors measured data, and (b) the temperature profile at the FBR outlet obtained from experiment and numerical model (Face velocity, V_f = 1.5 m/s, NTU_o = 2.25, Cr^* = 1.12).

The average sensible effectiveness determined from corrected temperature measurements of both exchanger and duct sensors were compared with numerical results and are shown in Figure 2.11. It can be observed that the results from both sensor arrangements are in good agreement with each other and with the numerical model. The maximum deviation of measurements between the exchanger and duct sensors from the numerical model is about 1.5% for a period of 10 s and this difference becomes less than 1.25% for 30, 60, and 90 s periods. Therefore, it is clear that the back fit temperature correction can give accurate results even for a period of 10 s.

Average of exchanger and duct sensor measurements (Average effectiveness): From analyzing several experimental and numerical temperature profiles, it is found that the initial transient behavior of the temperature sensors adversely affects the duct and exchanger sensor measurements. Duct sensors always measure lower values and exchanger sensors always measure

higher values than the actual temperature obtained from the numerical model. Therefore, an average of duct and exchanger sensor measurements could minimize the effect of these sensor transients. Figure 2.11 shows the comparison of sensible effectiveness obtained from the average sensor measurements (average of duct and exchanger sensors) with the numerical model. The maximum difference between the average effectiveness from the numerical model and linear backfit is approximately 2.5%. This method gives accurate results without any curve fits; however, it should be noted that all experimental facilities may not have the provision to attach the duct sensors (e.g. configuration presented in ref [43]). Therefore the results presented in the following sections are from the linear backfit method.

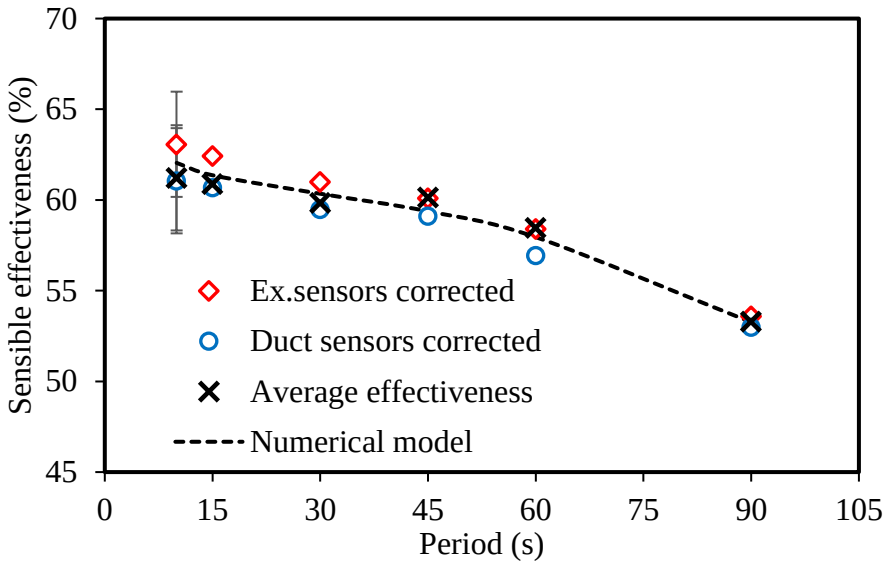

Figure 2.11. Comparison of sensible effectiveness determined from corrected sensor measurements and the numerical model (Face velocity, V_f = 1.5 m/s, NTU_o = 2.25).

2.10.3 Test facility energy balance

It is necessary to perform energy balance in every experiment to ensure that the system is operating at a quasi-steady state, (i.e., the heat stored in the exchanger during the hot period is equal to the

+heat released by the exchanger during the cold period) and to ensure the heat exchange with the surroundings is minimum.

During the quasi-steady state operation, in the absence of any heat losses and leakages from the test facility, the energy released from the exchanger during the cold period must be equal to the energy stored during the previous hot period. The sensible effectiveness values determined from temperature measurements in both the hot and cold periods (ε_{hot} and ε_{cold}) are used to analyze the energy balance since they represent a measure of energy transfer between the airstreams and the exchanger. The hot and cold period values of effectiveness, plotted in Figure 2.12, show that ε_{hot} is generally 2 to 4% greater than that of ε_{cold}.

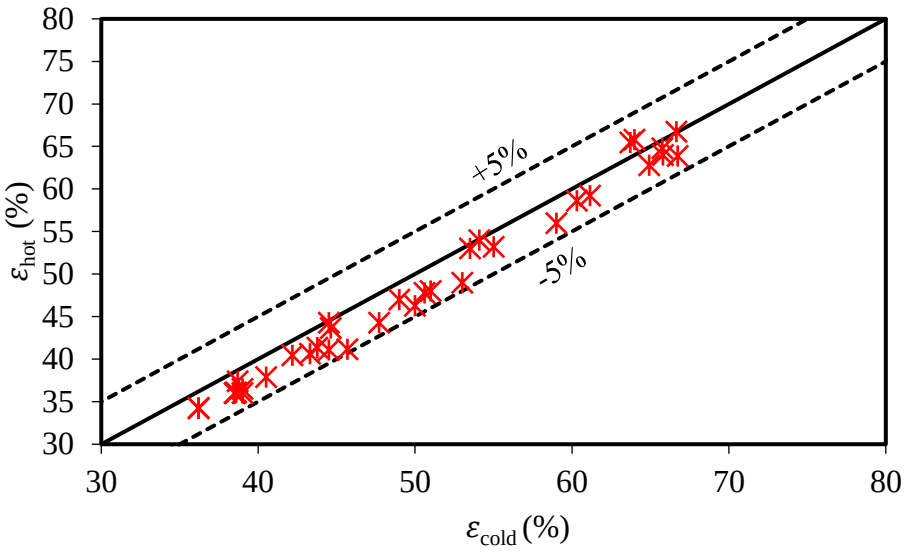

Figure 2.12. Sensible effectiveness determined from hot and cold period temperature measurements for the tested operating conditions.

In all tested operating conditions, comparatively higher ε_{hot} than ε_{cold} values indicate the possibility of heat loss to the surroundings. This difference between the ε_{hot} and ε_{cold} is acceptable because the deviation is less than 5% for a wide range of tested conditions, the uncertainty in

sensible effectiveness varies from 2 to 4%, and the average of ε_{hot} and ε_{cold} is being considered as the performance measure of FBRs.

2.10.4 Effects of face velocity on sensible effectiveness

The sensible effectiveness of the FBR varies with the inlet air stream velocity. The effect of the face velocity on the sensible effectiveness was studied by varying the face velocities from 1.0 to 1.7 m/s for a period of 60 s and the results are shown in Figure 2.13. The experiments were performed at balanced flow conditions, at which the flow rates of hot and cold airstreams are equal.

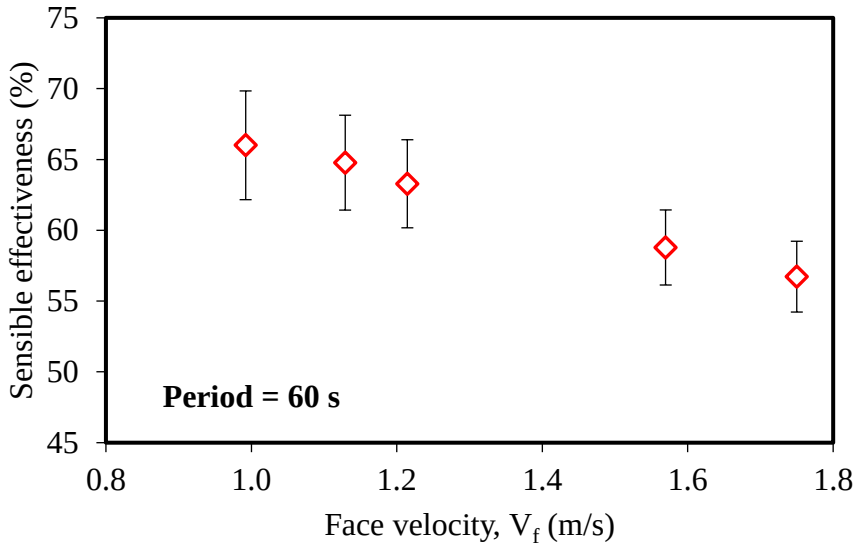

Figure 2.13. Variation of sensible effectiveness with face velocity.

It can be seen that the sensible effectiveness decreases with an increase in face velocity. This is due to the fact that, at higher face velocities, the flow residence time of air inside the exchanger is less, which reduces the heat transfer. In other words, NTU_o is inversely proportional to the face velocity and hence lower NTU_o at higher face velocity lowers the sensible effectiveness.

2.10.5 Effects of period on sensible effectiveness

The period is one of the critical design parameters for a FBR. In practical FBR units, the airflow direction is altered during each period with the help of dampers or valves. The life of the dampers/valves is also an important consideration since frequent valve switching, or damper movements, can cause excessive wear and tear, leading to leakages and premature failures. Furthermore, excessive carry-over due to frequent switching also reduces indoor air quality. The usual operating period of FBRs ranges from 40 to 60 s based on optimum sensible effectiveness, acceptable indoor air quality and the valves or damper's switching ability [8].

The effect of the period on the sensible effectiveness was studied by performing experiments at a constant face velocity of V_f = 1.12 m/s at five different periods ranging from 10 to 60 s. From Figure 2.14, it can be observed that sensible effectiveness increases with a decrease in period. This is mainly due to the fact that, the heat exchange between the air stream (hot/cold) and the exchanger is highest at the beginning of each period. As time proceeds, the heat transfer rate decreases and FBR reaches its maximum/minimum heat storage capacity, which decreases the sensible effectiveness.

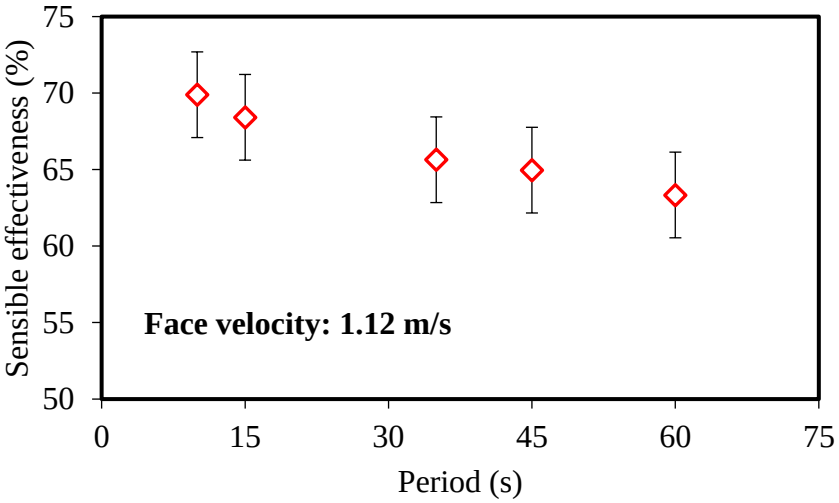

Figure 2.14. Variation of sensible effectiveness with period.

2.10.6 Comparison of test results with the numerical model and the correlations

The test results from small-scale tests can not be applied directly to evaluate the performance of FBRs in practice since the operating conditions and physical dimensions of the small-scale exchanger are different from that of real FBR units. Therefore, the tests were performed at different NTU_o and Cr^* conditions corresponding to that of practical FBRs. These results are verified with the numerical model and empirical correlations proposed by Kays and London [14] and Buyukalaca and Yilmaz [26].

The results from the parallel-plate exchanger are used to verify the small-scale testing methodology at different NTU_o and Cr^* conditions. The tested range of operating conditions for constant NTU_o and Cr^* experiments are summarized in Table 2.4.

Table 2.4. The small-scale FBR test conditions.

Sl. No	T_h (°C)	T_c (°C)	NTU_o	$Re_{channel}$	Cr^*
1	39 ± 0.2	24.1 ± 0.2	1.5 - 5.0	262-850	2.1
2			2.25	500	0.75 – 6.8

The obtained sensible effectiveness for constant Cr^* and NTU_o operating conditions are shown in Figure 2.15 and Figure 2.16, respectively. The sensible effectiveness of FBRs increases with an increase in NTU_o and Cr^*. It can be seen that the results obtained from experiments are in good agreement with the numerical model and literature correlations at the tested range of operating conditions. The maximum difference between experiment and numerical results is 2.3%. The uncertainty in measurements and the heat loss to surroundings could be the potential reasons for minor deviations in the experimental and numerical results.

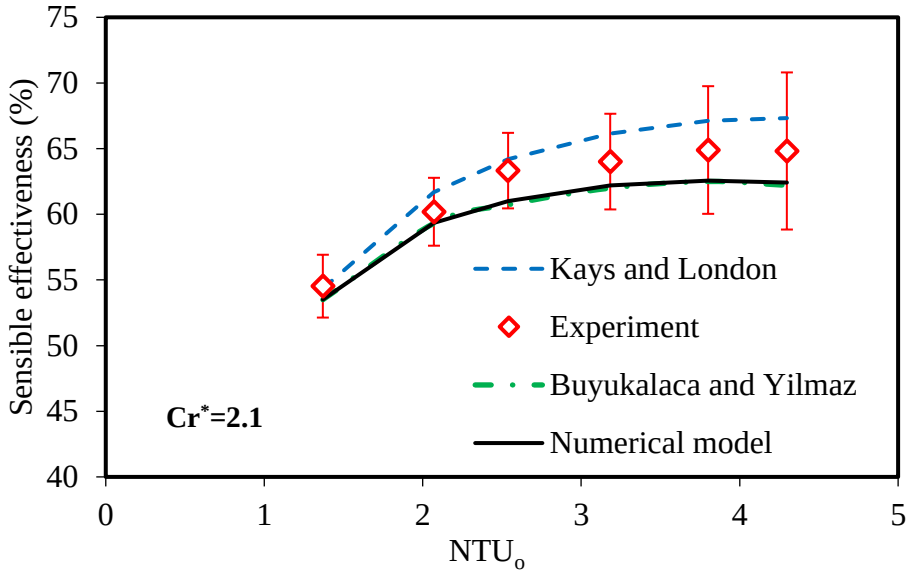

Figure 2.15. Comparison of sensible effectiveness obtained from experiments with numerical model and two design correlations for a constant Cr^*.

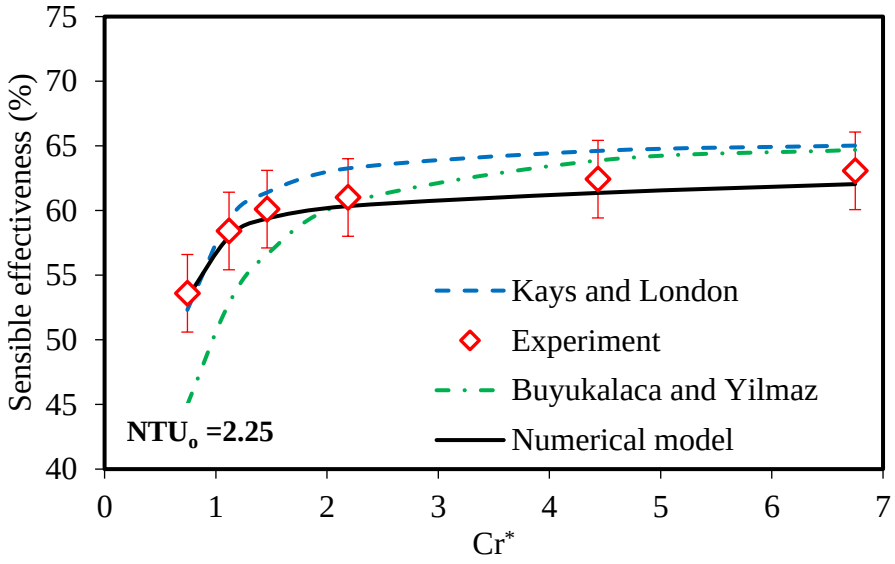

Figure 2.16. Comparison of sensible effectiveness obtained from experiments with the numerical model and two design correlations for a constant NTU_o.

The maximum difference between the experimental results and the Kays and London [14], [25] and Buyukalaca and Yilmaz [26], [59] correlations are about 3% and 8%, respectively. It should be noted that the Buyukalaca and Yilmaz have not included the effects of longitudinal heat conduction in their effectiveness correlation. Therefore the conduction parameter φ is determined

from Eqs. (2.17) to (2.20) and applied in both the Kays and London and Buyukalaca and Yilmaz correlations. The deviations in the experimental results from the literature correlations were expected since the applicability of the longitudinal heat conduction parameter in the literature correlations affects the sensible effectiveness results. As described in Section 2.9, the correlation for the conduction parameter is validated for $0 < \lambda < 0.08$. However, for the tested operating conditions, λ varies from 0.2 to 0.68 (where the face velocities are V_f = 2.5 m/s and 0.8 m/s, respectively).

It should also be noted that the correlations do not specify any uncertainty bounds for their results [21]. The Kays and London correlation is based on Lamberston's numerical model [38] which did not report any uncertainties. The correlation of Buyukalaca and Yilmaz was validated experimentally at low NTU_o and Cr^*operating conditions where they reported about 2.8-10% of deviation in sensible effectiveness for an increase in NTU_o from 1.26 to 2.31 [46], [59]. Considering the close agreement between numerical and experiment results as well as the range of applicability of literature correlations, the small-scale testing methodology can be considered as a potential alternative option for the performance evaluation of FBRs.

Full-scale FBRs with effectiveness more than 85% operate at NTU_o values ranging from 5-8. In small-scale testing, to achieve higher NTU_o's, either the air face velocity needs to be decreased or the heat transfer area should be increased. At lower face velocities, the longitudinal heat conduction through the exchanger plates reduces the sensible effectiveness even at high NTU_o's (or reduces the effective NTU_o). Therefore, increasing the length of the exchanger is an effective way to test at higher NTU_o's compared to lowering the face velocity.

2.10.7 Uncertainty analysis

Another critical aspect to be addressed with alternate testing methods is the uncertainty in results. ANSI/ASHRAE 84-2020 [12] recommends a maximum uncertainty level of 5% for the sensible effectiveness of energy exchangers. Therefore, the uncertainty levels of sensible effectiveness in any alternate testing methods should not exceed this limit. For the small-scale testing method presented herein, the uncertainty in sensible effectiveness comes from the systematic uncertainties in temperature and flow rate measurements. A detailed uncertainty analysis was carried out using the empirical correlation proposed by Kays and London [14] for a wide range of operating conditions. The sensible effectiveness of the small-scale exchanger presented in this study is estimated from the Kays and London correlation [14] at different operating conditions. Using this sensible effectiveness, the temperature of the air at the FBR outlet is calculated from Eqs. (2.4) and (2.5). The uncertainty in sensible effectiveness is finally determined by propagating the uncertainty in temperature and mass flow flowrate measurements using Eq. (2.3). The temperature difference between hot and cold inlet airstreams is assumed to be 10°C for this analysis. The relative uncertainty in the mass flow rate at different face velocities was determined by propagating the bias error in pressure drop measurements using Eq. (2.3) as shown in Figure 2.17.

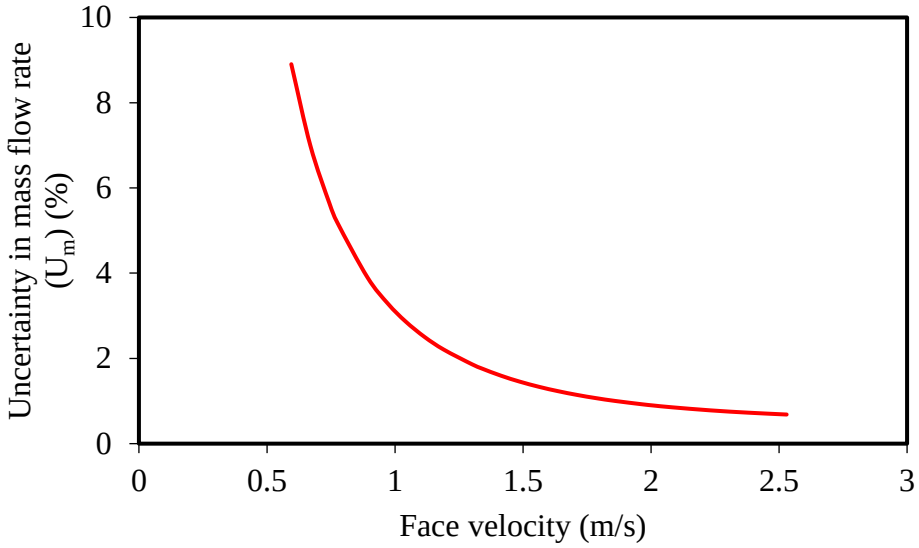

Figure 2.17. Uncertainty in mass flow rate at different velocities.

As the face velocity decreases, the pressure drop across the orifice plate decreases and the relative uncertainty in the pressure drop measurement increases. The usual operating face velocities in FBRs are between 1-2.5 m/s, where the corresponding uncertainty in mass flow rates are determined as 3.1 to 0.6%. The contribution of uncertainties in mass flow rates and temperature measurements on the sensible effectiveness for NTU_o ranging from 2-5 and the Cr^* from 0.5-5 are shown in Figure 2.18 (a) and (b), respectively. The uncertainty in sensible effectiveness due to systematic error in mass flow rate increases with an increase in NTU_o. This is because, for a given exchanger, the NTU_o can be increased only by reducing the mass flow rate. A decrease in mass flow rate results in an increase in uncertainty in pressure drop measurements (as shown in Figure 2.17), which leads to higher uncertainty in the sensible effectiveness as NTU_o increases. The contribution of bias errors in temperature measurements is shown in Figure 2.18 (b). It is clear that the uncertainty in sensible effectiveness due to bias error in temperature measurements increases slightly with an increase in NTU_o and Cr^*; however, these changes are less than 0.3%.

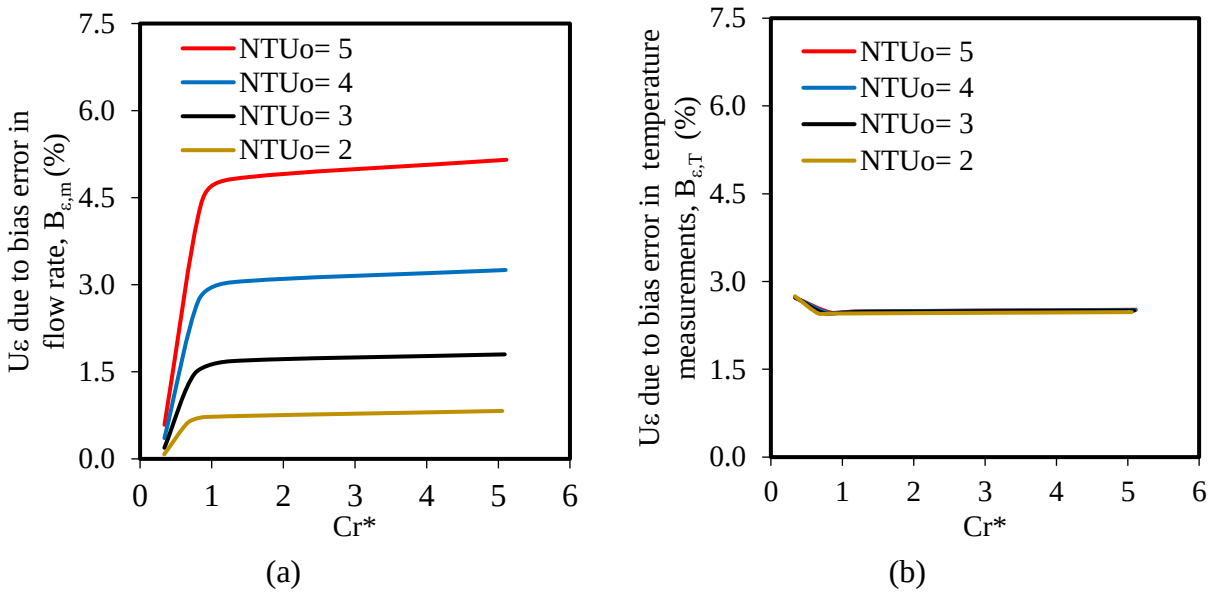

Figure 2.18. Uncertainty in sensible effectiveness due to systematic uncertainty in (a) flow rate and (b) temperature measurements at different NTU_o and Cr^* conditions.

The overall uncertainty in sensible effectiveness by considering bias errors in both pressure drop and temperature measurements is shown in Figure 2.19 (a). The increase in uncertainty in sensible effectiveness is significant with an increase in NTU_o compared to that of Cr*, which indicates that the uncertainty in flow rate measurements is more critical to the overall uncertainty in sensible effectiveness. In addition, the uncertainty in sensible effectiveness is determined for the limiting case of the test facility (i.e., operating a 1m long exchanger at NTU_o's ranging from 2-5), where the result is shown in Figure 2.19 (b).

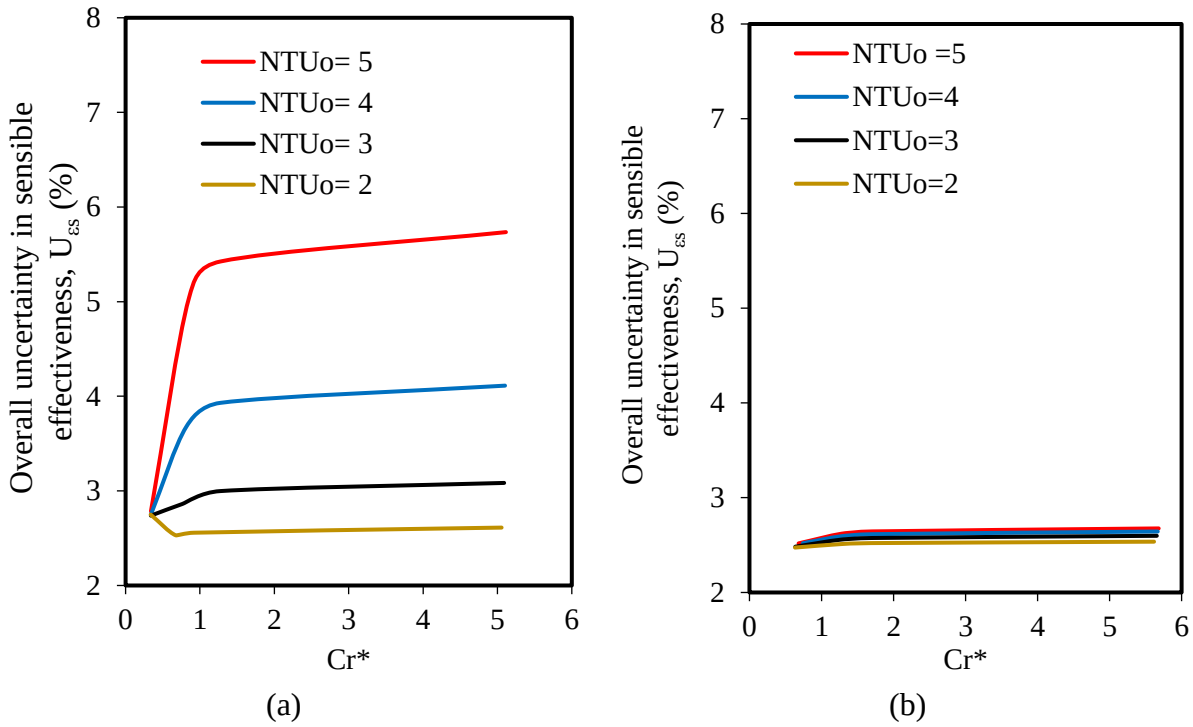

Figure 2.19. Overall uncertainty in sensible effectiveness for 20 cm (a) and 1 m (b) long FBRs at different NTU_o and Cr^* conditions.

It is also noted that the Kays and London correlation [14] is validated for the conditions where Cr^* and NTU_o are higher than unity. Therefore, the uncertainty analysis results may not be accurate for the operating conditions having NTU_o and Cr* less than unity. Based on the uncertainty analysis, it can be concluded that the facility is capable of producing test results below the ASHRAE 84 [12] recommended uncertainty limits up to an NTU_o of 4.5 for a 20 cm long parallel-plate exchanger. It is also possible to test FBRs having length up to 1 m and generate results within ASHRAE recommended uncertainty limits. Moreover, the uncertainties in small-scale testing can be further reduced by (i) decreasing the uncertainty in temperature and pressure drop measurements through equipment calibration and (ii) reducing the uncertainty in flow rate measurements by changing the orifice plates according to the operating conditions.

2.11 SUMMARY AND CONCLUSIONS

This chapter introduced a new small-scale test facility to investigate the performance of fixed-bed regenerators (FBRs) at different operating conditions. The facility is capable of testing exchangers having a length up to one meter, and the supply inlet air temperature and air velocity can be varied from -25 to 60°C and 0.8 to 2.5 m/s, respectively. The results from the small-scale tests are presented using dimensionless performance parameters, and the FBR performance curves are plotted at constant NTU_o and Cr^* operating conditions. The errors in FBR outlet temperature measurements due to the transient response of sensors are corrected using a linear backfit method. A parametric study is also performed to understand the influence of period and face velocity on the sensible effectiveness of the FBR.

The small-scale testing methodology is verified for FBRs by comparing the experimental results with the numerical model and two correlations for NTU_o and Cr^* from 1.5 to 5 and 1 to 6.5, respectively. The maximum difference in sensible effectiveness obtained from test results and the numerical model is 2.3%. When compared with the correlations, the experiment results have a maximum deviation of 3% and 8% with the Kays and London [14] and Buyukalaca and Yilmaz [59] correlations, respectively. These deviations are mainly because the value of the conduction parameter is outside the range of its applicability in the correlations. In addition, a detailed uncertainty analysis was performed and the contribution of each measurement to the overall uncertainty in sensible effectiveness was identified. The good agreement of test results with the numerical model and low uncertainty in sensible effectiveness show that small-scale testing is a promising alternative methodology to evaluate the performance of FBRs. An important contribution of this thesis (from this chapter) is a new test facility and method for the sensible

effectiveness evaluation of FBRs. The test facility can be used to study the heat and moisture transfer in FBRs having different plate geometries and desiccant materials.

CHAPTER 3

METHODOLOGIES FOR PREDICTING THE SENSIBLE EFFECTIVENESS OF FULL-SCALE FBRs

3.1 OVERVIEW

Development and commissioning of the small-scale test facility for FBR were presented in Chapter 2 of this thesis. In this chapter, new methods to estimate the sensible effectiveness of full-scale FBRs from small-scale tests are presented. Thus, this chapter addresses the second objective of this Ph.D. research, "To develop test methods to predict the sensible effectiveness and uncertainty of full-scale FBRs from small-scale tests." Two methods were proposed to determine the sensible effectiveness of FBRs from small-scale test data and verified with the field test results of full-scale FBRs. The results were published in the ASME Journal of Thermal Science and Engineering Applications in February 2021. It should also be noted two more sections are included in this chapter explaining (a) the differences in pressure drop measurements observed between small-scale and full-scale tests and (b) additional set of correlations for average heat transfer coefficients.

The developed test methods were applied for studying the effects of exchanger plate geometry on the thermo-hydraulic performance of FBRs. Experiments were conducted on small-scale exchangers having different corrugation angles, corrugation depths, and lengths. These results were verified for all the exchangers using direct and predictive methods and reported in a separate manuscript titled "Experimental investigation on thermo-hydraulic performance of triangular-cross corrugated flow channels." The manuscript was published in International Communications in Heat and Mass transfer in March 2021 and included as Appendix B of this thesis. The major contributions of the manuscripts in Chapter 3 and Appendix B are providing two methods to

determine the performance of full-scale exchangers from small-scale data and reporting the effects of corrugation parameters on the performance of FBRs.

Tempeff Inc. provided the exchanger samples, full-scale test results, and the author of this thesis (Easwaran N. Krishnan) performed all the experiments, data acquisition, and data analysis and wrote the original draft of the manuscripts. Mr. Hadi Ramin (Ph.D. student) generated the numerical data. Dr. A. Gurubalan (postdoctoral fellow), Dr. Wahab Alabi (postdoctoral fellow), and Prof. Carey J. Simonson (supervisor) critically reviewed this manuscript. The operation of the FBR, description of the test facility and instrumentation details are not included in this chapter to avoid repetition.

Methodologies for Predicting the Effectiveness of Full-Scale Fixed-Bed Regenerators from Small-Scale Test Data

(Published in ASME Journal of Thermal Science and Engineering Applications in February 2021)

Easwaran N. Krishnan, Hadi Ramin, A. Gurubalan, Wahab O. Alabi and Carey J. Simonson

3.2 ABSTRACT

Fixed-bed regenerators (FBRs) are air-to-air energy exchangers used to reduce energy consumption in heating, ventilation, and air conditioning (HVAC) systems. Since energy savings are directly related to the effectiveness of FBRs, testing is essential to determine the effectiveness of FBRs for quality assurances and during product development. However, testing of full-scale FBRs has disadvantages such as requiring full-scale prototypes, a high volume of conditioned airflow, long tests, and large testing laboratories. The disadvantages are especially crucial during product development and can be overcome by small-scale testing, provided the test data can be used to evaluate accurately full-scale FBRs. The major contribution of this chapter is two new methodologies (one direct method and one predictive method) to determine the sensible effectiveness of full-scale FBRs from small-scale test data. In the direct method, the effectiveness of the full-scale FBR is determined directly from the small-scale test data, whereas in the predictive method, the effectiveness is determined using the Wilson plot technique and a numerical model in addition to the small-scale test data. Both methods are shown to have uncertainties within the specified uncertainty limits required by testing standards and are applied to evaluate the influence of geometrical parameters (corrugation angle and corrugation depth) on the effectiveness of FBRs.

The test methods and results will be useful in the design and development of FBRs for HVAC applications.

3.3 INTRODUCTION

The motivations in developing new test methods for FBR performance evaluation were already discussed in Chapter 1 and the test facility was introduced in Chapter 2. However, the physical dimensions and operating conditions of small-scale tests are different from those of full-scale exchangers, and the test results cannot be applied directly in the performance evaluation of full-scale FBRs. Therefore, methodologies are developed to predict the sensible effectiveness of full-scale FBRs from small-scale test data and are presented in this chapter.

The experiments on FBRs are critical because numerical models and empirical correlations (e.g., Refs. [25], [26], [46], [57], [59], [61]) available in the literature require known values of the convective heat transfer coefficients. Heat transfer correlations have been developed for laminar flow in many flow channel configurations such as parallel plates and rectangular, or honeycomb shapes [28]. However, most of these correlations are only valid for certain operating conditions for their specific applications. The exchangers used in FBRs are made of cross corrugated metallic plates and the heat transfer process in these flow passages is still not fully understood [62] and there are no established heat transfer correlations available in the literature.

Studies have been reported in the literature explaining the heat transfer process in corrugated passages using different techniques such as (i) flow visualization techniques [63]–[65], (ii) liquid crystal thermography [66] and (iii) CFD numerical simulations [67]–[69]. However, these techniques require expensive instrumentation or complex 3D models and are often not suitable for designers. The Wilson plot technique is a powerful tool for performance testing of heat exchangers [70]. The idea of this technique is to split the overall thermal resistance of the system into

individual thermal resistances and develop correlations for heat transfer coefficients using statistical procedures. The heat transfer correlations based on the Wilson plot technique can then be used to design exchangers [71]–[73]. Thus, experiments on full-scale FBRs are considered as one of the conventional methods to evaluate the effect of corrugation on the heat transfer performance of FBRs.

The tests on small-scale FBRs cannot always be performed at the same design and operating conditions (NTU_o and Cr*) as that of full-scale FBRs, due to (i) the longitudinal heat conduction effects along the matrix and (ii) difference in exchanger lengths. Therefore, further analysis for extrapolating the small-scale data to full-scale FBRs is required. In this chapter, direct and predictive methods to determine the sensible effectiveness of FBRs from small-scale tests are presented. The direct method uses experiment data from small-scale tests, and the predictive method uses the Wilson plot technique and a numerical model in addition to the test data.

3.4 EXPERIMENTAL METHODS

3.4.1 Test facility

The same small-scale experimental facility described in Section 2.4 was used to develop the test methods presented in this chapter. The measurement procedures and data analysis are also identical to the procedure described in Section 2.7.

3.4.2 Small-scale exchangers

Small-scale corrugated exchanger prototypes from Tempeff Inc. [11] have been used in this study to develop the testing methodologies and perform the sensitivity studies. The exchangers are made of corrugated aluminum sheets (Al 3003) in a proprietary pattern. The geometry of a sample corrugated plate and the specifications of the exchanger prototypes are shown in Figure 3.1 and Table 3.1, respectively.

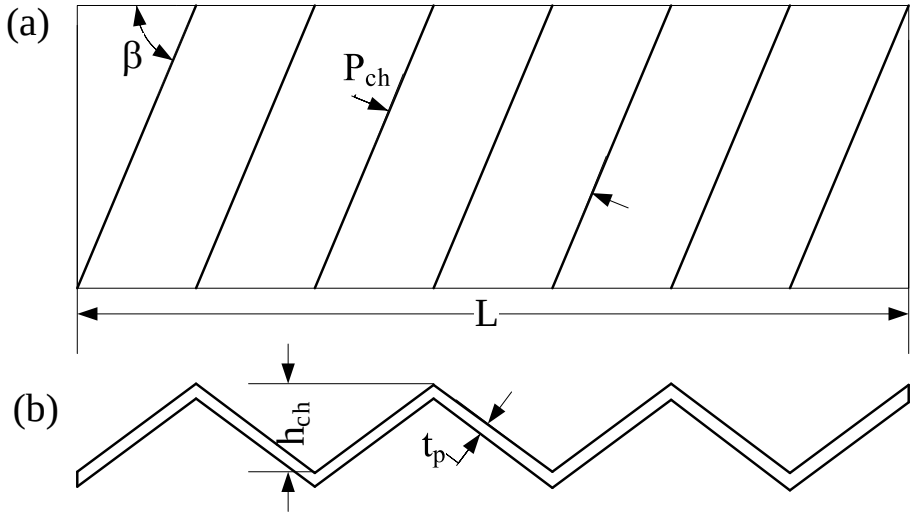

Figure 3.1. Schematic of a corrugated plate used in FBRs (a) top view (b) side view.

The channel hydraulic diameter (Eq. (3.2)) is defined using the width and equivalent height of flow channels (h_{ch}) which is determined using Eq. (3.1),

$$h_{ch} = \frac{\left[H_{EX} - \left(n_p \cdot t_p\right)\right]}{n_f} \tag{3.1}$$

$$D_h = \frac{4A_g}{P_w} \tag{3.2}$$

where A_g, and P_w are cross-sectional area and wetted perimeter of the flow channel, H_{EX}, t_p, n_p, and n_f are the height of the exchanger, the thickness of the plate, and the number of plates and the number of flow channels, respectively.

EX 1 is considered as the standard exchanger with a specific proprietary corrugation angle and depth, which is used as the reference exchanger for this study. EXs 1, 2, and 3 are used to validate the testing methodology since they all have the same plate geometry but with different lengths and thus heat transfer areas. The proposed methodologies are also applied to study the effects of plate geometry on the effectiveness of FBRs. The effect of corrugation angles is studied using EXs 1, 4, and 5. It is also noted that the corrugation angles of EXs 4 and 5 have been reported with

reference to that of EX 1, i.e., the corrugation angle of the plates in EX 4 with respect to the airflow direction is 29° lower than that of EX 1. The EXs 6, 7, and 8 are used to study the influence of corrugation depth, as noted in Table 3.1.

Table 3.1. Geometrical properties of small-scale exchangers.

Exchanger sample	Corrugation angle	h_{ch}/P_{ch}	L/h_{ch}	No. of flow channels	Hydraulic diameter (m)	Heat transfer area (m^2)
EX 1	β	0.13	49	14	0.0082	0.488
EX 2	β	0.13	116	14	0.0082	1.176
EX 3	β	0.13	232	14	0.0082	2.34
EX 4	β–29°	0.13	50	14	0.0082	0.498
EX 5	β+21°	0.13	52	14	0.0082	0.515
EX 6	β	0.08	82	22	0.00480	0.684
EX 7	β	0.25	73	9	0.0130	0.791
EX 8	β	0.36	59	7	0.0167	0.647

3.5 TESTING METHODOLOGIES

The purpose of this chapter is to develop and validate methodologies to evaluate the effectiveness of full-scale FBRs from small-scale test data. The first method, the direct method, is based on the test results from a similar small-scale exchanger, whereas the predictive method uses a numerical model, a correlation from the literature, and small-scale test data. The principle, procedures, advantages, and limitations of both methodologies are described in the following subsections.

3.5.1 Direct method

In the direct method, the effectiveness of FBRs is evaluated from the small-scale test results using dimensionless parameters NTU_o and Cr*. Based on the regenerator theory [25], regenerators will have the same effectiveness when they operate under the same design conditions of NTU_o's and Cr*. There are two ways to achieve same NTU_o for small-scale and full-scale FBRs: (i) testing a

portion of FBRs, i.e., a small-scale exchanger with the same length as the full-scale FBR and (ii) testing a small-scale exchanger (does not need to be the same length as the full-scale FBR) at a lower face velocity. Lowering the velocity will increase the NTU_o; however, it also favors the longitudinal heat conduction through the matrix, which is undesirable as it reduces the effectiveness. Therefore, in this method, testing a small-scale exchanger with the same length as the full-scale FBR is preferred.

It is already reported in the literature that the uncertainty in sensible effectiveness of the direct method (arising from the uncertainty in flow rate and temperature measurements) will be less than the ASHRAE specified limits (5%) by carefully selecting test conditions and suitable instrumentation [74]. This method is useful in testing of FBRs with shorter lengths, such as room-based ventilation systems. The limitation of this method is that it is not always practical to maintain the length of the small-scale exchanger as that of full-scale since many exchangers have a length of more than 2 m. This method is also not preferred for product development as it requires many exchanger samples, which increases the material and prototyping costs.

3.5.2 Predictive method

In this method, a correlation for average heat transfer coefficient is developed from the small-scale test data and the performance of the full-scale FBR is evaluated using this correlation in a numerical model. The overall number of transfer units (NTU_o) is calculated from the experimental effectiveness and ε-NTU_o method [25] as presented in Section 2.9.2 of Chapter 2. The average heat transfer coefficient for the air stream is determined from Eq. (3.3) using mass flow rate measurements, surface area of heat transfer and NTU_o. The experiments are repeated at different face velocities and a correlation for the heat transfer coefficient as a function of face velocity is developed by applying the concept of the Wilson plot technique [14], [70]. The effectiveness of

the full-scale FBRs is predicted using this correlation in a numerical model developed by Ramin et al. [55], [61]. The model was described in Section 2.8 of Chapter 2.

$$NTU_o = \frac{U\,A_{ht}}{C_{min}} = \frac{1}{C_{min}}\left[\frac{1}{1/(hA_{ht})_1 + 1/(hA_{ht})_2}\right] \quad (3.3)$$

3.6 RESULTS AND DISCUSSIONS

A series of 32 experiments were conducted using eight exchangers over the range of face velocities $1 < V_f < 2.5$ m/s to validate and apply the proposed testing methodologies. Tests were performed at balanced flow conditions($\dot{m}_1 = \dot{m}_3$) and the temperatures of the hot and cold airstreams were 23 °C and 1 °C, respectively. The detailed operating conditions for all the tests are reported in Table 3.2.

3.6.1 Validation of testing methodology

3.6.1.1 Direct method

The direct method is validated by conducting experiments on EX 3, which has the same length and similar corrugation as that of the tested full-scale exchanger. Therefore, when these exchangers operate at the same face velocity, NTU_o, and Cr*, the effectiveness of both the small-scale and full-scale exchangers must be equal. The results from the direct method are compared with the field test results of the full-scale exchanger and are shown in Figure 3.2.

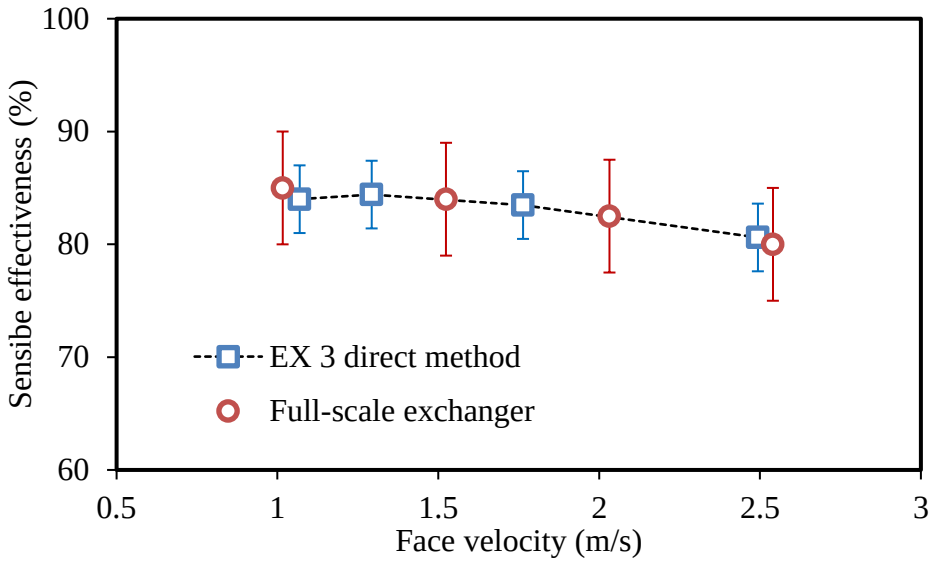

Figure 3.2. Sensible effectiveness of FBR from the direct method and full-scale tests.

Table 3.2. Operating conditions for small-scale tests.

Face velocity, V_f (m/s)	Re	EX 1		EX 2		EX 3		EX 4		EX 5	
		NTU_o	Cr*	NTU_o	Cr*	NTU_o	Cr*	NTU_o	Cr*	NTU_o	Cr*
1	643	1.6	2.4	3.8	2.6	7.4	4.9	1.7	2.4	1.2	2.3
1.3	778	1.5	1.6	3.5	2.2	7.0	4.0	1.5	1.6	1.05	1.6
1.8	1061	1.3	1.3	3.2	1.5	6.4	3.0	1.3	1.2	0.9	1.2
2.5	1500	1.2	0.8	3	1.0	6.0	2.1	1.1	0.8	0.75	0.8
Face velocity V_f (m/s)		EX 6			EX 7			EX 8			
		Re	NTU_o	Cr*	Re	NTU_o	Cr*	Re	NTU_o	Cr*	
1		438	1.85	2.9	963	3.2	3.5	1257	3.0	2.8	
1.3		543	1.6	2.35	1312	2.8	2.6	1524	2.7	2.3	
1.8		740	1.45	1.72	1617	2.6	1.9	2205	2.3	1.6	
2.5		980	1.3	1.2	2535	2.3	1.3	3182	2.1	1.3	

The effectiveness of EX 3 is in good agreement with that of the full-scale FBR within the experimental uncertainty limits and the maximum deviation is approximately 2.5%. The effectiveness results also agree with the regenerator theory reported in the literature [14], i.e., as the face velocity increases, the flow residence time in the exchanger decreases (or low NTU_o) and hence lowers the effectiveness. The good agreement between the results from the direct method and the full-scale tests, in addition to the lower uncertainty in the direct method, shows that the proposed methodology is a suitable alternative for the full-scale testing of FBRs.

3.6.1.2 Predictive method

The test results of EX 1, EX 2, and the full-scale exchanger are used to validate this testing methodology since these three exchangers have the same plate geometry but different heat transfer areas. The heat transfer correlation developed from the test results of EX 1 (following the procedure described in Section 3.2) is used to model the full-scale exchanger and EX 2. The variation of heat transfer coefficient as a function of face velocity is plotted and the correlation for heat transfer coefficient is derived by fitting a linear curve, as shown in Figure 3.3. The coefficient of determination (R^2) of the correlation is 0.9972.

Figure 3.4 compares the effectiveness determined from the predictive method with the experimental results of the full-scale exchanger and EX 2. The results are in good agreement within the experimental uncertainty limits, and the maximum differences between experimental and predicted results are less than 2.5% for all test conditions. This observed difference could be attributed to the experimental uncertainties, uncertainties in the heat transfer correlation, and the effects of heat loss/gain in the test facility.

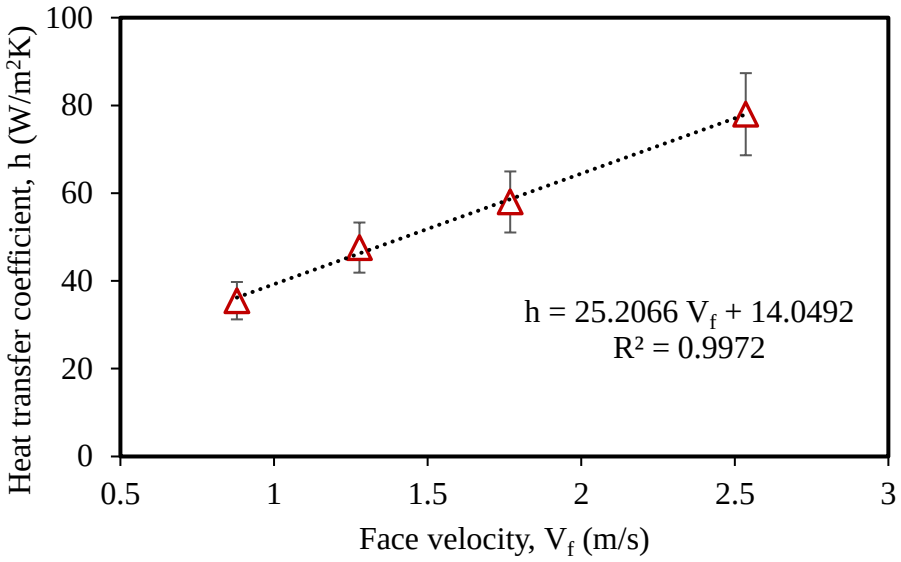

Figure 3.3. Average heat transfer coefficients for EX 1.

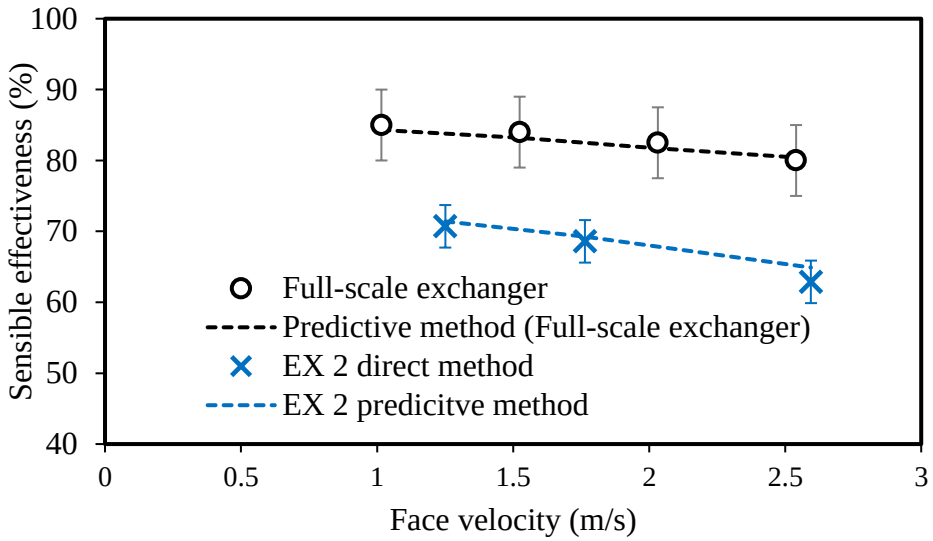

Figure 3.4. Sensible effectiveness of FBR from the direct method, predictive method, and full-scale tests.

The effectiveness of the full-scale exchanger is higher than that of EX 2, and which is directly related to its higher heat transfer area (or high NTU_o) as reported in Table 3.2. Considering the good agreement between the predictive method and test results, the method successfully predicts the effectiveness of the full-scale FBR.

3.6.2 Uncertainty analysis

ANSI/ASHRAE standard 84-2013 [12] recommends a maximum uncertainty of 5% for sensible effectiveness results. Thus, any alternate method (such as small-scale testing in this chapter) should be able to determine the results within this specified uncertainty limit. For the direct method, the uncertainty in sensible effectiveness arises from the flow rate and temperature measurements. The uncertainty in sensible effectiveness from small-scale testing is approximately 2.5% for a wide range of operating conditions, and the contribution of each measurement parameter to the overall uncertainty has been evaluated and reported in Section 2.10.7 of Chapter 2. [74].

The major source of uncertainty in the predictive method comes from the uncertainty in the heat transfer coefficient. Uncertainty in the heat transfer coefficient is determined using the rule of uncertainty propagation, which includes the uncertainties in effectiveness (obtained from the small-scale tests) and in the Kays and London correlation. The uncertainty propagation equations for the heat transfer coefficient and effectiveness (in small-scale tests) are given in Appendix C.

An uncertainty analysis on the reference exchanger (EX 1) is performed to determine the uncertainty in the predictive method. The analysis is carried out at lower NTU_o conditions as the predictive method does not require exchangers with a high heat transfer area (long exchangers). For this analysis, the uncertainty in mass flow rate and temperatures are assumed to be ±2% and ±0.2 °C, and the uncertainty in the Kays and London correlation is assumed to be ±1% [14]. It should also be noted that the Kays and London correlation is valid for cases with NTU_o and Cr* higher than unity. The relative uncertainty in the heat transfer coefficient (Eq. C.13) for the operating range of small-scale testing shown in Figure 3.5(a) and corresponding uncertainties in effectiveness are shown in Figure 3.5 (b).

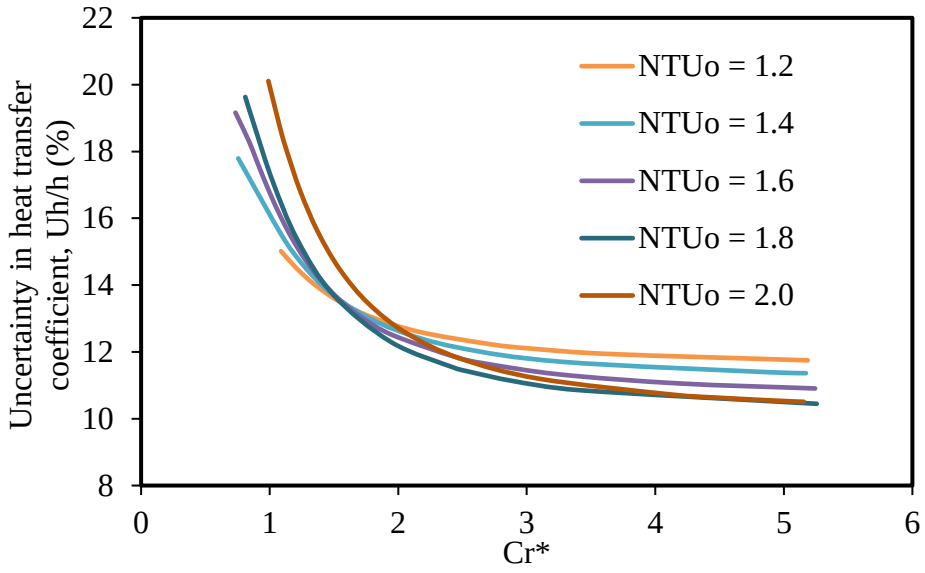

Figure 3.5. (a) Relative uncertainty in the heat transfer coefficient as a function of NTU_o and Cr*.

Figure 3.5(a) shows that the uncertainty in the heat transfer coefficient (h) and effectiveness (ε) generally decreases as Cr* and NTU_o increase. As the value of Cr* increases, the uncertainty in heat transfer coefficient (h) and effectiveness (ε_s) approaches a constant value, as seen in Figure 3.5 (a). Even though the heat transfer coefficient uncertainty may be as high as ±15%, the maximum uncertainty is less than 3.5% for the limiting test conditions (i.e., NTU_o=1.2) and decreases at higher NTU_o values. As NTU_o increases, the uncertainty in the heat transfer coefficient has a smaller influence on the effectiveness. Based on the uncertainty analysis, it is recommended to design small-scale experiments with Cr* > 1 and NTU_o > 1. For a given range of face velocities, the exchanger must have the physical dimensions (heat transfer area) to achieve NTU_o > 1. Higher Cr* can be achieved by reducing the period. However, short periods may introduce additional errors due to the sensor time constants [74], [75].

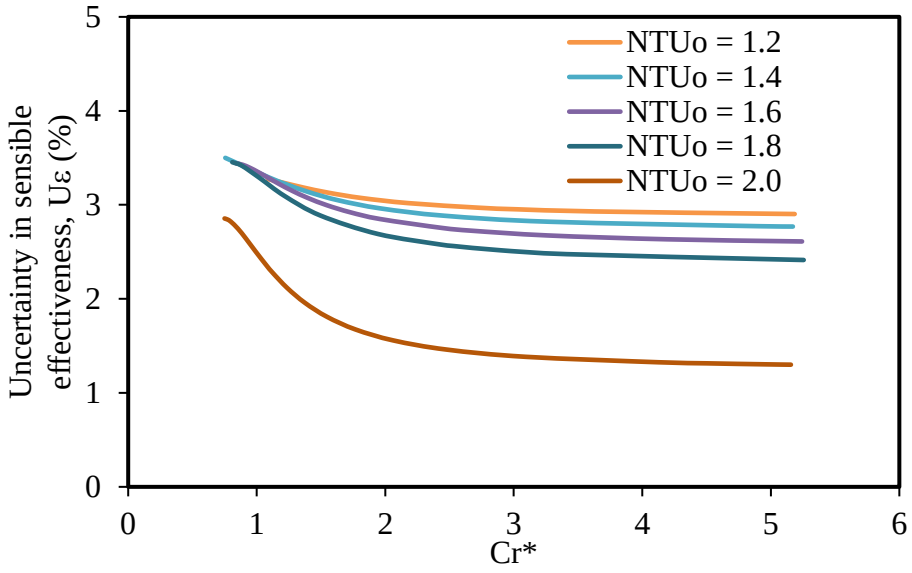

Figure 3.5. (b) uncertainty in effectiveness due to uncertainty in the heat transfer coefficient.

3.6.3 Application of testing methodologies

The test methodologies explained in the previous sections are now used to determine the effect of corrugation angle and corrugation depth on the heat transfer performance of FBRs.

3.6.3.1 Effect of corrugation angle

The effect of corrugation angle on sensible effectiveness and heat transfer coefficients are studied using EXs 1, 4, and 5. These exchangers have different corrugation angles but are similar in all other physical dimensions, as listed in Table 3.1. The specific operating conditions are listed in Table 3.2.

The effectiveness of the exchangers at different face velocities determined from small-scale testing and the predictive method is shown in Figure 3.6. The maximum difference between the effectiveness from the direct and predictive methods is less than 2.5% for all test conditions. Since the temperatures of the airstreams at the FBR outlet change with time, the temperature profiles at the outlet of these exchangers (for face velocity, V_f = 1.8 m/s) obtained from the experiments and

predictive method are also compared in Figure 3.7. During the hot period (0-30s), the exchanger stores heat from the airstream. The outlet air temperature is lowest at the beginning of each hot period since the heat transfer rate between the exchanger and airstream is maximum due to their large temperature difference. As time continues, the exchanger attains maximum heat capacity and thereby the outlet air temperature increases. In the subsequent cold period, the exchanger releases the heat stored in the previous hot period to the incoming cold airstream, therefore the outlet temperature increases. Similar to the hot period, the maximum heat exchange occurs at the beginning of each cold period, and gradually the outlet air temperature decreases. The good agreement of numerical and experimental temperature profiles (Figure 3.7) also confirms the validity of this method.

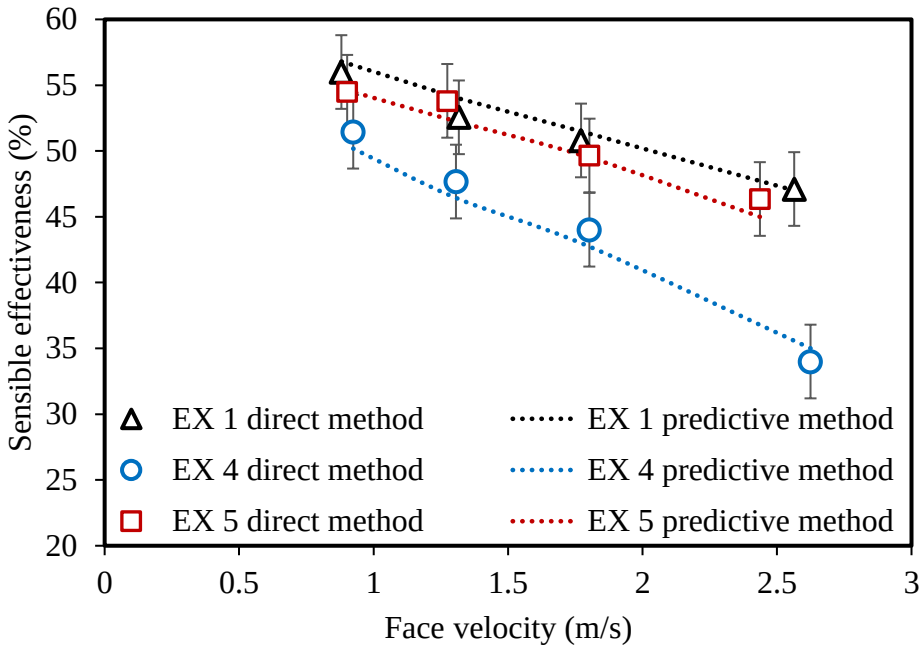

Figure 3.6. Effect of corrugation angle on sensible effectiveness for EXs 1, 4, and 5.

The numerical results are simulated using the heat transfer coefficients derived from the procedures explained in Section 3.2.3, and the heat transfer correlations results are presented in Figure 3.8. Among the three exchangers, EX 4 has the lowest corrugation angle (β–29°) and

effectiveness, as shown in Figure 3.6. EX 5 has the highest corrugation angle (β+19°) , and the effectiveness is about 1-2% lower than EX 1 for most of the test conditions.

The complex three-dimensional flow through the cross corrugated plates of exchangers strongly influences the heat transfer process. Based on corrugation angle and corrugation depth, three different types of flow patterns, namely furrow flow, longitudinal wavy flow, and mixing flow have been observed in cross corrugated flow channels [63], [65], [76]–[83]. At lower corrugation angles, the majority of flow follows the direction of corrugation and is reflected at the sidewalls of the exchanger, and this type of flow is called furrow flow, which is very similar to ordinary duct flow. At higher corrugation angles, most part of the fluid follows a parallel zig-zag pattern in the longitudinal direction (along the exchanger length) and is called longitudinal wavy flow. The presence of more contact points between the adjacent plates due to high corrugation angles results in flow separation and reduces the effective heat transfer [79]. At intermediate corrugation angles, the mixing of longitudinal and furrow flows (mixing flow) induces secondary swirls in the flow along corrugations, which leads to higher heat transfer [65], [83].

The results from flow visualization and mass transfer techniques suggests that the furrow flow occurs for $\beta < 30°$, mixing flow for $30° < \beta < 60°$ and longitudinal flow for $\beta > 60°$ [77], [82]. However it is not possible to specify the flow behavior based on corrugation angles alone since it is also a function of corrugation depth (or h_{ch}/P_{ch}). Gasier and Kottke [79] reported that for sinusoidal cross corrugated flow channels, the maximum heat transfer occurs at $\beta \approx 45°$ for a $h_{ch}/P_{ch} = 0.14$, when the h_{ch}/P_{ch} was changed to 0.20, the corresponding corrugation angle (β) for maximum heat transfer shifted to 60°. Their results have been recently verified using flow visualization techniques by Dovic and Svaic [65]. The findings of the present study are also in agreement with these literature conclusions, i.e., the maximum sensible effectiveness and heat

transfer coefficients are reported for EX 1, which has the intermediate corrugation angle. Therefore, based on the above-discussed results, it is reasonable to conclude that the heat transfer rate increases with an increase in the corrugation angle until it reaches a maximum value, after which there is no significant improvement in the heat transfer rate.

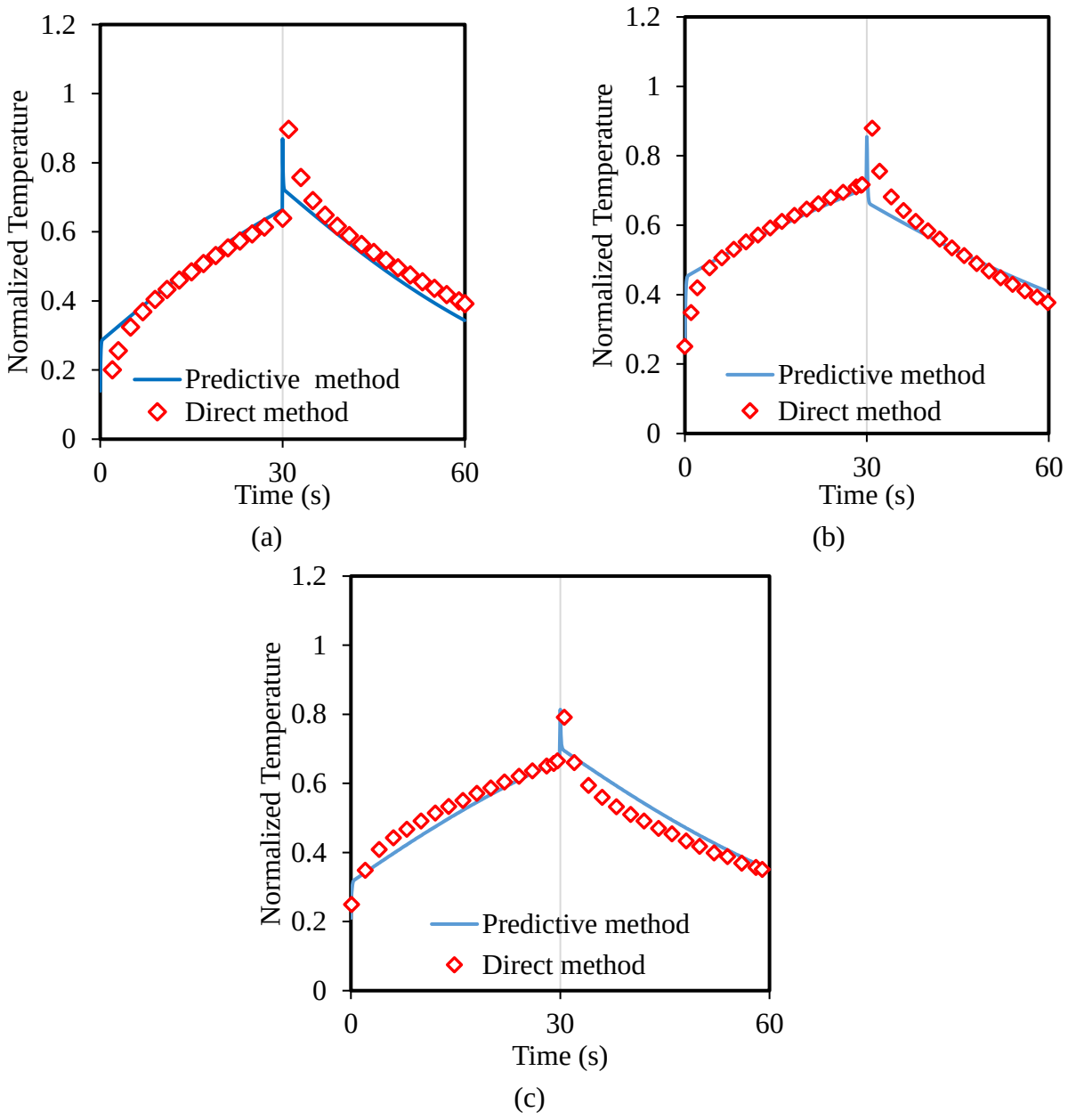

Figure 3.7. Temperature profile comparison of (a) EX 1, (b) EX 4 and (c) EX 5 (Face velocity, V_f = 1.8 m/s).

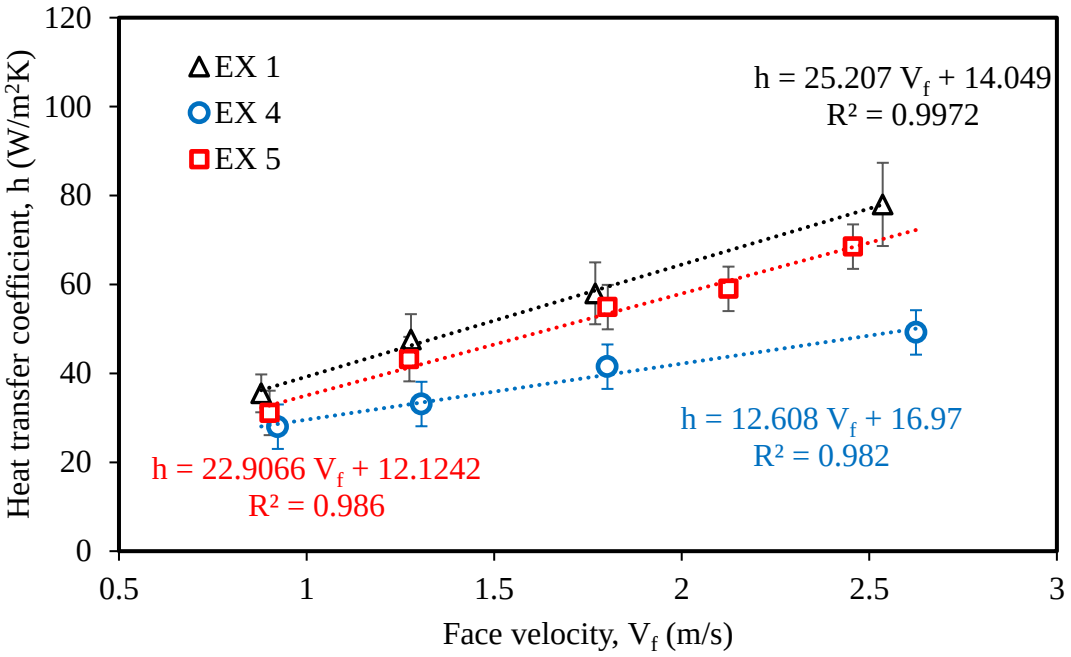

Figure 3.8. Average heat transfer coefficients for EXs 1, 4 and 5.

3.6.3.2 Effect of corrugation depth

Corrugation depth is considered as one of the key variables to optimize the performance of an FBR for maximum effectiveness. The effect of corrugation depth, or ratio of h_{ch}/P_{ch}, on heat transfer and sensible effectiveness is examined by testing three exchangers (EXs 6, 7, and 8) having the same corrugation angles but different corrugation depths.

Figure 3.9 shows the comparison of sensible effectiveness of EXs 6,7 and 8 obtained from the direct and predictive methods. For a given face velocity, the highest and lowest effectiveness are observed for EXs 7 and 6, respectively. The EX 7 cannot be considered as the best exchanger since the number of plates (i.e., heat transfer area) in these exchangers are different. Hence the comparison is extended for the heat transfer coefficient as depicted in Figure 3.10.

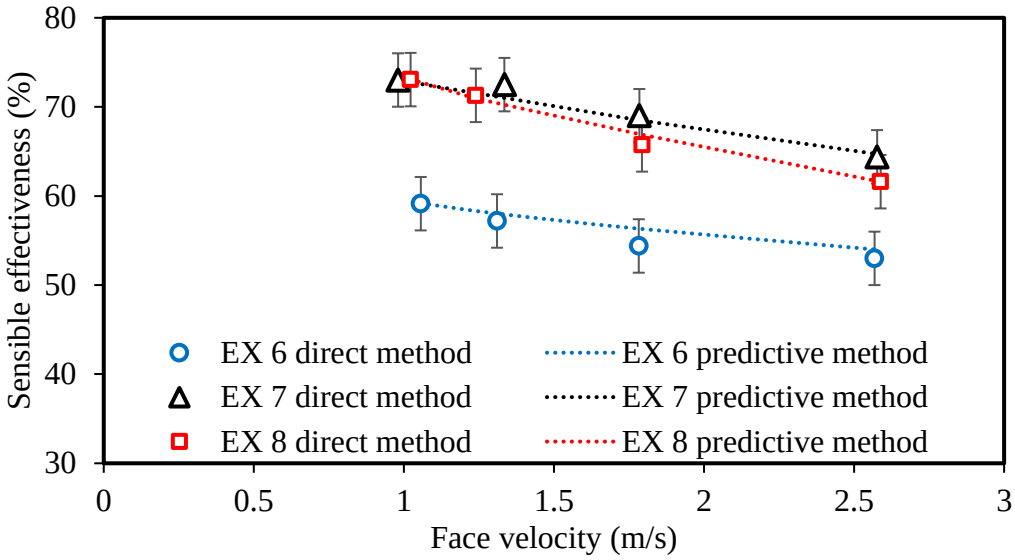

Figure 3.9. Effect of corrugation depth on sensible effectiveness for EXs 6, 7, and 8.

The highest and lowest heat transfer coefficients are observed for EXs 8 and 6, respectively, which indicates that the heat transfer rate increases with an increase in corrugation depth (or h_{ch}/P_{ch} ratio). The higher corrugation depth promotes the furrow component of the flow and as the corrugation angle increases the longitudinal wavy flow also becomes dominant [79]. Previous studies on sinusoidal cross corrugated flow channels have shown that at intermediate corrugation angles ($\beta \approx 45°$), these two streams are mixed more thoroughly resulting in higher heat transfer rates [65], [84]. On the other hand, decreasing corrugation depth increases the influence of the longitudinal wavy flow, which is desirable at lower corrugation angles for the effective mixing of two dominant flow components. Results from the present study are also in agreement with the findings of Dovic and Svaic [65], [84], Zimmerer et al. [83], and Gasier and Kottke [79], i.e., an increase in corrugation depth at intermediate corrugation angles results in higher heat transfer. The influence of corrugation depth and corrugation angle is summarized in Table 3.3 along with the results previously reported in the literature. It should be noted that the corrugation angle and corrugation depth reported in the table are based on the definition presented in Figure 3.1. The temperature

profiles obtained from the direct and predictive methods are presented and compared in Figure 3.11. The good agreement between the small-scale test data and predicted results also confirms the validity of this methodology.

The thermo-hydraulic performance of the exchangers reported in this chapter is investigated and compared using the Nusselt number and friction factor. A separate manuscript is published explaining the Nusselt number and friction factor results for each of these exchangers. This manuscript is not included in the main body of the thesis since the thesis is focusing on test methodology development, but it is included in Appendix B.

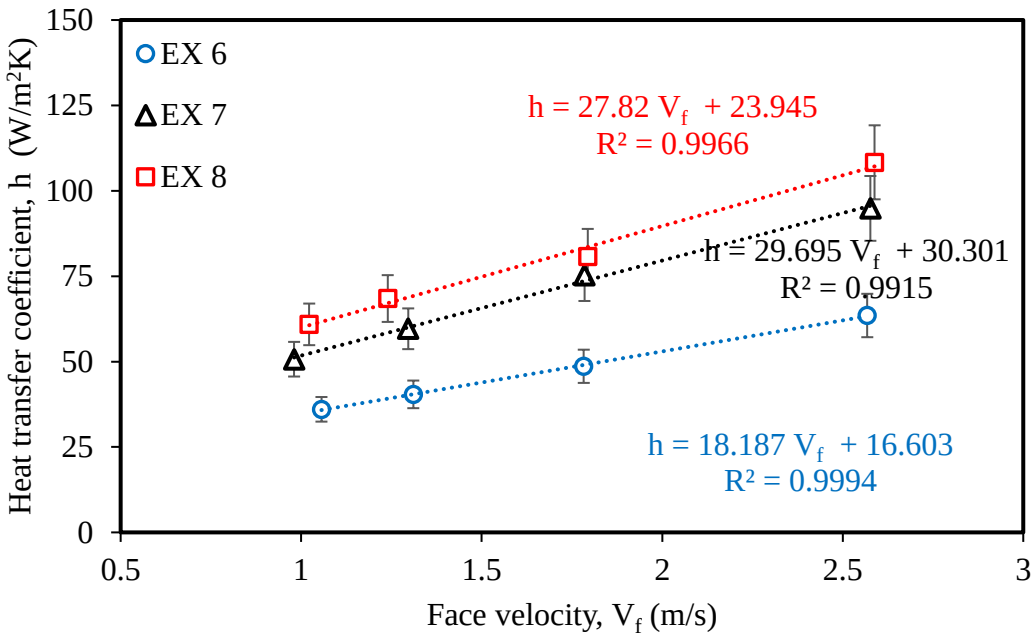

Figure 3.10. Average heat transfer coefficients for EXs 6, 7 and 8.

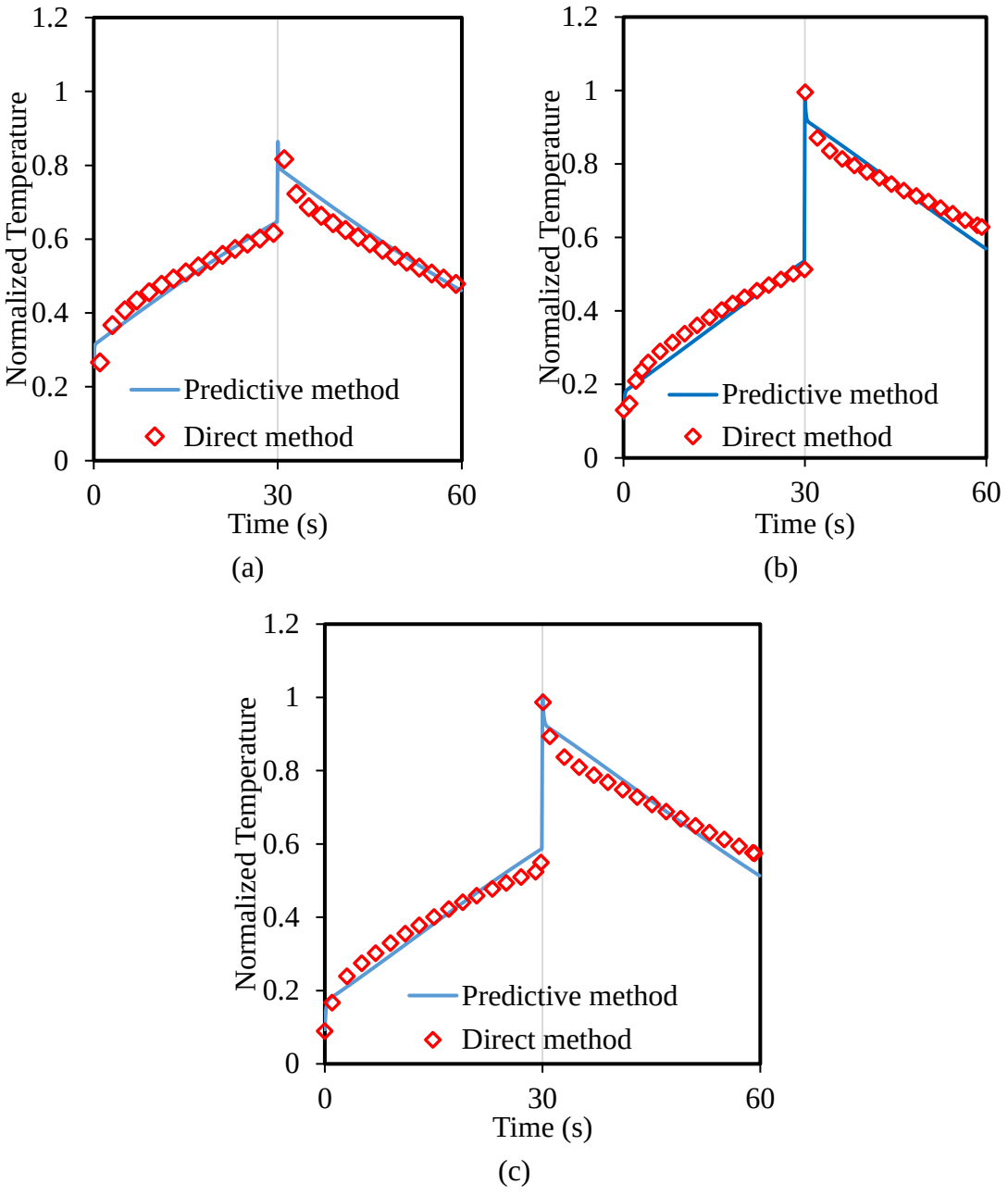

Figure 3.11. Temperature profile comparison of (a) EX 6, (b) EX 7 and (c) EX 8 (Face velocity, V_f = 1.8 m/s).

Table 3.3. Influence of corrugation angle and corrugation depth on heat transfer performance.

Author details	Corrugation angle considered (β)	Corrugation depth considered (h_{ch}/P_{ch})	Effect on heat transfer coefficient or Nusselt number	
			Increase in corrugation angle	Increase in corrugation depth
Gasier and Kottke [79]	20°→80°	0.14-0.27	↑followed by ↓	↑
Muley and Manglik [78]	30°, 60°	0.28	↑	↑
Dovic and Svaic [84]	28°, 65°	0.26	↑	---
Stasiek et al. [80]	30°, 37.5°	0.45	↑	↑
Fock et al. [77]	0°→90°	0.5	↑followed by ↓	---
Present study	0°→90°	0.08-0.36	↑ followed by ↓	↑

3.6.3.3 Correlations for heat transfer coeffect

For the tested operating conditions (0.8 m/s < V_f < 2.5 m/s), the average heat transfer coefficients of corrugated exchangers vary linearly with face velocity and are presented in Figures 3.8 and 3.10. Therefore, correlations were developed as y = mx + c. Similarly, it is possible to correlate the heat transfer coefficient with face velocity (V_f) in the form of $C(V_f)^n$. The fitting coefficients C and n, and the coefficient of determination of fit (R^2) for the tested exchangers are reported in Table 3.4.

Table 3.4. Correlation coefficients of heat transfer coefficients, $h = C(V_f)^n$.

EX	C	n	R^2
EX 1	39.13	0.71	0.998
EX 4	29.51	0.51	0.997
EX 5	34.92	0.72	0.999
EX 6	34.79	0.59	0.997
EX 7	44.28	0.7	0.998
EX 8	60.2	0.56	0.996

3.7 NOTES ON PRESSURE DROP EVALUATION OF FUL-SCALE FBRS FROM SMALL-SCALE TESTING

The small-scale testing method proposed in this thesis is verified only for the effectiveness evaluation. In addition to that, it is also essential to investigate the effect of scaling on the pressure drop across the exchangers. The effect of exchanger length (in the direction of airflow) on the pressure drop is investigated by testing EXs 1, 2, and 3. It is found that the friction factor of small-scale exchangers with different lengths agree with each other within the uncertainty limits (c.f. Figure B.6 (a)). However, the friction factor obtained for small-scale exchangers is nearly half that of the full-scale FBRs. This can be attributed to the frontal area of the small-scale exchangers being 10 times lower than that of the full-scale exchangers. The deviation in friction factor indicates that the exchanger side walls may significantly influence the flow direction and pattern inside the small-scale exchangers. It should also be noted that the findings from Stasiek et al. [80] confirming the side boundaries having a significant effect on the pressure drop measurements while the heat transfer is only affected a little. The effect of scaling on the pressure drop needs to be studied by testing small-scale exchanges with different aspect ratios and using flow visualization techniques. The current experimental facility requires modifications in order to test exchangers with different frontal areas.

3.8 SUMMARY AND CONCLUSIONS

The major contribution of this chapter is that it introduces new methodologies (direct and predictive methods) to determine the sensible effectiveness of full-scale fixed-bed regenerators (FBRs) from small-scale test data. The results from both methods were validated with field test results of a full-scale FBR, and they are in good agreement with each other within the experimental uncertainty limits. The proposed methodologies are to be chosen according to the test conditions

and the number of tests required. The direct method has the lowest uncertainty in effectiveness (≈ ±2.5%) because full-scale effectiveness values are obtained from the small-scale test data. The predictive method has a higher uncertainty (≈ ±3.5%) since it uses a numerical model and Wilson plot technique in addition to the small-scale test data. However, the predictive method requires only an optimum number of test runs since it uses the numerical model for the performance evaluation.

These methods developed in the chapter are applied to investigate the effects of plate geometry (corrugation angle and depth) on the effectiveness of FBRs. The obtained results show that the heat transfer coefficient and effectiveness increase with an increase in corrugation angle and attain maximum values, where further increase did not cause any significant changes. It is also found that the heat transfer coefficient and effectiveness increase with corrugation depth. Therefore, the effectiveness of FBRs can be improved by carefully choosing the plate corrugation angle and corrugation depth.

CHAPTER 4

METHODOLOGIES FOR PREDICTING THE EFFECTIVENESS OF DESICCANT COATED FBRs

4.1 OVERVIEW

This chapter presents (a) a new experimental method to determine the latent effectiveness of FBRs and (b) verifies the transient humidity measurement technique called the Bag Sampling Method (BSM) recommended by ASHRAE 84 [12] and CSA C439-18 [13] test standards. The methods and preparation of the desiccant coated small-scale exchanger, the design and development of the BSM, and the location and arrangements of sensors are explained in detail. A validated numerical model and a correlation from the literature have been used to verify the experimental results. The test uncertainty is also quantified for a wide range of FBR operating conditions. Thus, the third objective of this thesis, "To develop testing methodologies to predict the latent and total effectiveness and uncertainty of desiccant-coated full-scale FBRs from small-scale tests" is accomplished in this chapter.

The manuscript presented in this chapter has been published in the International Journal of Heat and Mass Transfer. The conclusion section of the thesis is modified from that of the manuscript to incorporate more details. The author of this Ph.D. thesis (Easwaran N. Krishnan) performed all the experiments, preparation of desiccant coated exchanger, data acquisition, and data analysis, and wrote the original draft of the manuscript. Dr. Mohsen Shakouri (postdoctoral fellow) has supported the development of the bag sampling method. Mr. Hadi Ramin (Ph.D. student) has performed numerical analysis and provided the results for the test conditions suggested by

Easwaran N. Krishnan. Dr. A. Gurubalan (postdoctoral fellow) and Prof. Carey J. Simonson (supervisor) critically reviewed this manuscript in addition to the supervision of the entire work.

Experimental Method to Determine the Effectiveness of Desiccant Coated Fixed-Bed Regenerators (FBRs)

Easwaran N. Krishnan, Hadi Ramin, A. Gurubalan and Carey J. Simonson

(Published in International Journal of Heat and Mass Transfer in September 2021)

4.2 ABSTRACT

Desiccant coated fixed-bed regenerators (FBRs) transfer heat and moisture between two airstreams having different temperatures and humidity. The experiments on FBRs are challenging because of their transient nature of operation. Unlike other energy exchangers, FBRs do not attain a steady-state condition; instead, they reach a quasi-steady state where the humidity and temperature of the outlet air continuously vary with time. This chapter shows that measuring the temperature and humidity of a time-varying airstream with temperature and humidity sensors may lead to errors in effectiveness in the order of 15-20%. Meanwhile, the method proposed in this chapter reduces errors to ±5-8%, which is comparable to the uncertainties in accepted steady-state test standards. The major contributions of this chapter are (i) development and verification of new experimental methods to determine the effectiveness of desiccant coated FBRs and (ii) verification of the bag sampling method (BSM) for humidity measurements proposed by test standards. The results are verified using a validated numerical model and a correlation from the literature.

4.3 INTRODUCTION

Most of the literature explaining the heat and mass transfer process in regenerators are based on numerical models or empirical correlations [43], [61], [80], [85], [86]. There are several correlations predicting sensible effectiveness accurately for a certain range of operating conditions [25], [26], [32], [46], [59]. However, only a few correlations are available for predicting the

moisture transfer performance (latent effectiveness) [29], [30], [87], and this could be due to the complexities in simultaneous heat and moisture transfer process because of the influence of many parameters such as operating conditions, properties of desiccants and types of desiccant coating [88], [89]. Therefore, conducting experiments is critical in quantifying the moisture transfer performance of FBRs and identifying suitable desiccants for moisture transfer applications. On the other hand, only a few materials have proven as suitable desiccant candidates for moisture recovery applications in HVAC systems [90]. Experimental investigations on full-scale regenerators have shown that silica gel, alumina composites, and molecular sieves [39], [40], [91]–[93] are suitable for building energy recovery systems. However, no investigations have specifically recommended any suitable desiccant candidates for FBR applications.

Recently Krishnan et al. [74], [94] developed a new experimental facility and methods to evaluate the heat transfer performance of FBRs for HVAC applications. The errors in sensible effectiveness of FBRs due to the slow response of thermocouples have been evaluated numerically and quantified for a range of test conditions [75]. The time constants of thermocouples and humidity sensors were investigated and reported previously by Abe et al. [18], [19] and Wang et al. [45], [95]. Their results show that commercial capacitive humidity sensor responses are even slower than that of thermocouples. The ASHRAE-84 [12] and CSA C439-18 [13] standards have recently proposed a new technique called the bag sampling method (BSM) for data reduction and accurate humidity averaging at FBR outlets. However, BSM is cumbersome, does not provide real-time humidity measurements, and requires additional instrumentation.

The major objectives of this study are to (a) develop a new test method called small-scale testing to determine the latent effectiveness of FBRs, (b) verify the bag sampling method (BSM) proposed by ASHRAE 84 [12] and CSA C439-18 [13] test standards, and (c) understand the significance of

transient humidity profiles at the FBR outlets and their impact on latent effectiveness. Finally, the results are presented using nondimensional performance parameters and compared with a numerical model and design correlations from the literature. The proposed method will be useful in testing and development of FBRs and selecting desiccant materials for HVAC applications.

4.4 METHODOLOGY

In this section, the principle and operation of the test facility, measurement and instrumentation details, and the uncertainty analysis are provided.

4.4.1 Experimental facility

The small-scale test facility used to measure the effectiveness of FBRs is shown in Figure 4.1. The core of the test facility is the test section (Figure 4.2), where the desiccant-coated exchanger (EX) is periodically moved between two conditioned airstreams. When the exchanger is exposed to the humid airstream, the desiccants adsorb the moisture (adsorption period), and it desorbs the same during the next period when it is exposed to the dry air stream (desorption period). More details of the test facility and measurements were reported in Chapter 1, and only an overview is presented here.

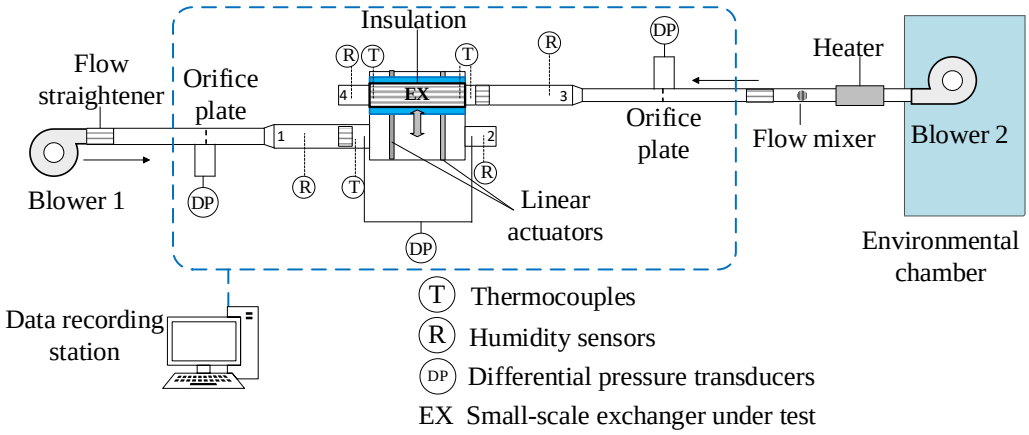

Figure 4.1. Schematic of the small-scale FBR test facility.

Calibrated T-type thermocouples, capacitive humidity sensors, and orifice plates with differential pressure transducers are used to measure the temperature, humidity, and flow rates of airstreams, respectively. The uncertainties associated with various measurements and their calibration ranges are presented in Table 4.1. The measured temperatures are recorded using a computer-controlled National Instruments data acquisition system.

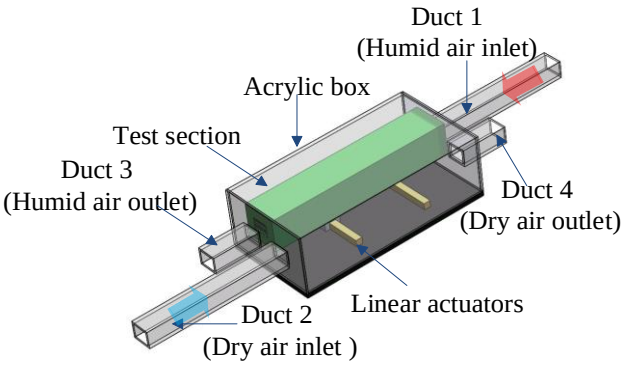

Figure 4.2. Schematic of the FBR test section.

Table 4.1. Instruments specifications and calibration details.

Measurements	Device type	Calibration range	Total uncertainty
Temperature	Omega T-type/ (0.08 mm wire dia.)	-40 – 40°C	±0.2°C
Flow rate	Validyne differential pressure transducer	0-860 Pa	±8 Pa
Humidity	Honeywell capacitive type	15-85% at 25°C and 35°C	±1.5 %

4.4.2 Desiccant coated small-scale exchanger

The small-scale exchanger comprises twenty-six desiccant coated aluminum plates (Al 3003), as shown in Figure 4.3. Each plate is 20 cm long, 8 cm wide, and 0.69 mm thick. The equally spaced plate constitutes twenty-five flow channels with a hydraulic diameter of 4.08 mm. 3D printed side frames made of ABS plastic are used to assemble the plates at an equal distance.

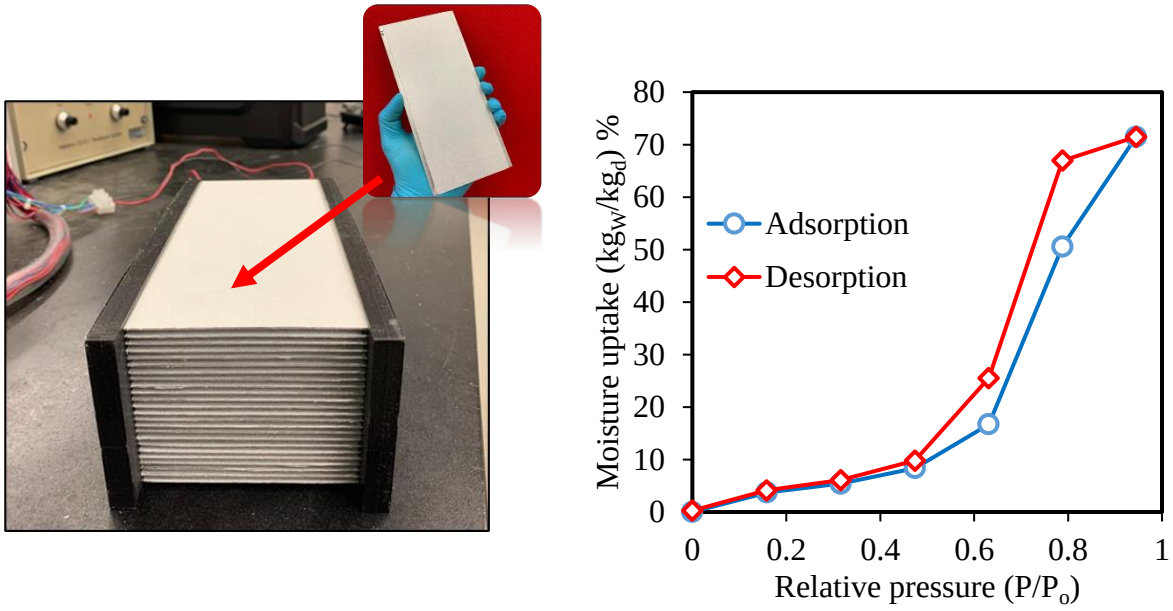

(a) (b)

Figure 4.3. (a) Desiccant coated small-scale exchanger and (b) sorption isotherm of silica gel at 25°C.

The silica gel desiccant was coated on both sides of the aluminum sheets. Usually, binders are employed in the industrial coating process to assure the bonding between desiccants and substrates. This results in multilayer desiccant coating with reduced interaction between water vapor and active sorption sites due to pore blockage [88]. Unlike industrial coating methods, the sieving method [22], [24], [90] developed at the University of Saskatchewan is used in this study, and thus assured a uniform monolayer desiccant coating on the aluminum plates. Images of the coated plate surface were obtained using Hitachi FEG-SEM SU6600 scanning electron microscope (SEM) and are shown in two different magnification levels of 1 mm and 400 μm in Figure 4.4. The SEM image also confirms the monolayer desiccant-coating. In this method, a 3M Super 77 spray adhesive is applied on both sides of aluminum sheets, and the non-adhesive side of an annealed aluminum tape (0.035 mm thick) is attached to the sheet surface. Afterward, the silica gel particles are uniformly sieved (200 mesh screen) over the plate's adhesive surface and gently pressed to

enable surface binding. Finally, the loosely bounded silica gel particles are removed using a pressurized air jet. The physical properties of desiccants and details of desiccant coating are reported in Table 4.2.

Table 4.2. Physical properties and coating mass of desiccants.

Material	Density* (kg/m^3)	Average particle size* (μm)	Mass of coating (g)	Desiccant mass/coated area (mg/cm^2)	Desiccant/matrix mass ratio (%)
Silica gel	350	150	45.36	5.67	4.81

*Data from manufacturer catalog

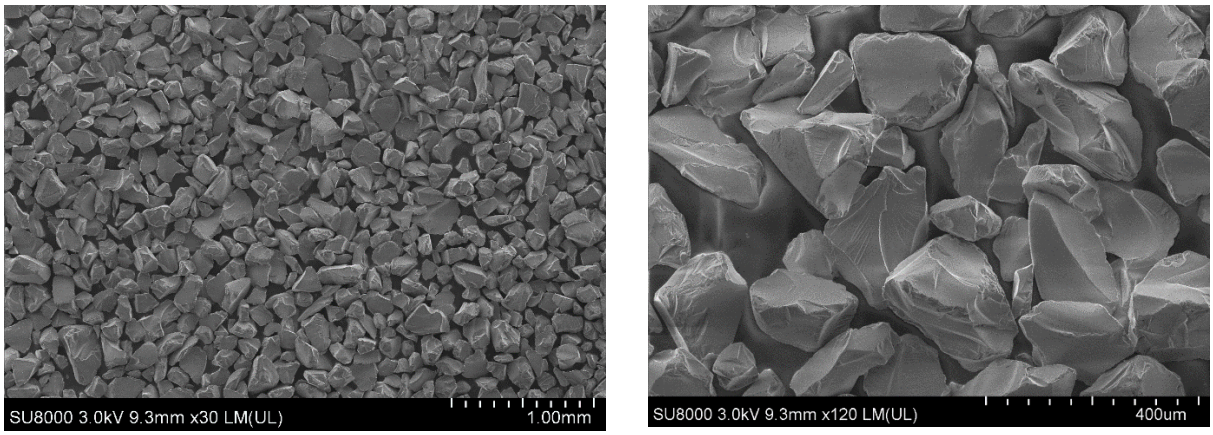

(a) (b)

Figure 4.4. SEM images of desiccant-coated exchanger plates (a) 1 mm and (b) 400 μm magnification levels.

The sorption isotherm provides the adsorption-desorption characteristics of desiccants as a function of relative humidity or water vapor pressure. Experiments on silica gel were performed using the Gravimetric Analyzer system (IGA-002, manufacturer: Hiden Isochema Ltd., United Kingdom). The IGA-002 consists of a microbalance with a resolution of 0.1 μg and uncertainty of ±1 μg. About 30 mg of sieved silica gel was loaded in the sample holder for this experiment. The sample holder is isolated from the surroundings using an ultra-high vacuum stainless-steel reactor. The temperature of the desiccant sample was accurately measured and controlled using a water

bath with an accuracy of ± 0.1˚C. The desiccant sample was degassed and dried at 60˚C under vacuum (≈10^{-7} mbar) for 6 hours and was held isothermally at 25°C. The sorption measurements were acquired at 25°C for different relative humidity ranging from 0-95%, as shown in Figure 4.3 (b). The maximum moisture uptake is 0.715 kg_w/kg_d. The sorption curve represents type IV, which is common for mesoporous materials [96], and the hysteresis loop observed is due to the capillary condensation within the mesopores.

4.4.3 Location and arrangements of sensors

During the operation, the exchanger is exposed to both humid and dry air streams; therefore, the outlet air humidity and temperature vary continuously. The sensors must respond quickly to measure the outlet air properties accurately. Capacitive humidity sensors and T-type thermocouples are arranged in two different locations at the test section and inside the ducts, as shown in Figure 4.5. The sensors placed in the test section (at the inlet and outlet of the exchanger) move with the exchanger and are called exchanger sensors (or Ex. Sensors). The exchanger sensors measure the air humidity/temperature at the exchanger inlets during one period and measure the exchanger outlet air humidity/temperature in the next period.

Four thermocouples and relative humidity sensors are placed at each inlet and outlet duct and are called duct sensors. The duct sensors are stationary and are always exposed to the same airstream. For instance, the sensors located in duct ④ will measure the exchanger outlet air properties during one period and measure the air inlet properties during the subsequent period.

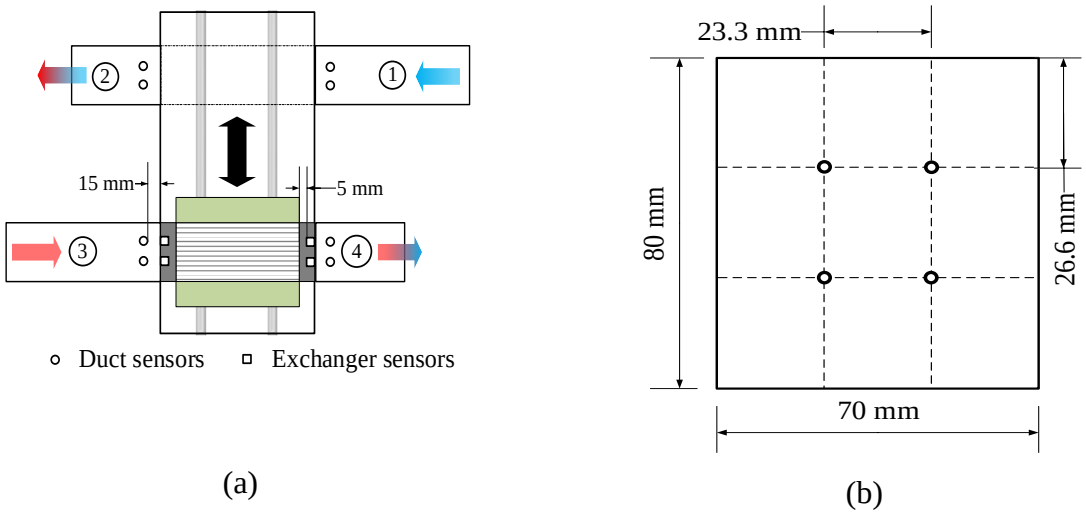

Figure 4.5. Schematic of the test facility showing the (a) locations of thermocouples and humidity sensors and (b) their spatial arrangements at the exchanger inlet and outlet.

4.4.4 Performance parameters

The heat and moisture transfer performance of FBRs is quantified using sensible, latent, and total effectiveness. The effectiveness of an FBR is defined as the ratio of the energy transfer rate between the exchanger and the airstream to the maximum possible energy transfer rate. Effectiveness depends on the capacity rate of the working fluid, physical and thermal properties of the desiccant materials, heat/moisture transfer area, and the period. Equation (4.1) is used to determine the effectiveness of a small-scale FBR during heating (and/or humidification), and cooling (and/or dehumidification) periods [14]. Ideally, the effectivenesses determined using the outlet temperature and humidity ratios during both periods must be equal if there is no heat/moisture interaction between the exchanger and the surroundings. However, in experiments, the measured data may vary due to experimental uncertainties, even if there is no heat/moisture interaction with surroundings. Therefore, the average of the effectiveness values is considered for the analysis, which also reduces the experimental uncertainty [29].

$$\varepsilon = \frac{C_1}{C_{min}} \frac{(X_1 - \overline{X}_2)}{(X_1 - X_3)} = \frac{C_3}{C_{min}} \frac{(\overline{X}_4 - X_3)}{(X_1 - X_3)}, \quad (4.1)$$

where ε represents sensible, latent, or total effectiveness (ε_s, ε_l, or ε_t), X_1, $\overline{X}_2$, X_3 and $\overline{X}_4$ indicate dry bulb temperature (for sensible effectiveness), humidity ratio (latent effectiveness), and enthalpy (total effectiveness) of the airstream at the ducts 1, 2, 3, and 4, respectively. C_1 and C_3 are the capacity rates of the hot and cold airstreams and C_{min} is the minimum of C_1 and C_3. Since the temperature and humidity of the outlet airstreams vary with time, the time-averaged outlet parameter determined using Eq. (4.2) is used for effectiveness estimation [14],

$$\overline{X} = \frac{1}{P} \int_0^P X(t) dt, \quad (4.2)$$

where $X(t)$ is the instantaneous outlet air temperature or humidity, and P is the total period.

4.4.5 Bag sampling method (BSM)

ASHRAE 84 [12] and CSA C439-18 [13], [23] suggest air sampling at the FBR outlets as an alternate method to measure the average humidity ratio over a period. In this method, a sample of the outlet air stream is collected in a bag during the entire adsorption/desorption period, and the bag is allowed to reach an equilibrium state. The average humidity ratio of this sample can then be determined by measuring the equilibrium relative humidity and temperature, and latent effectiveness can be calculated using this average humidity ratio.

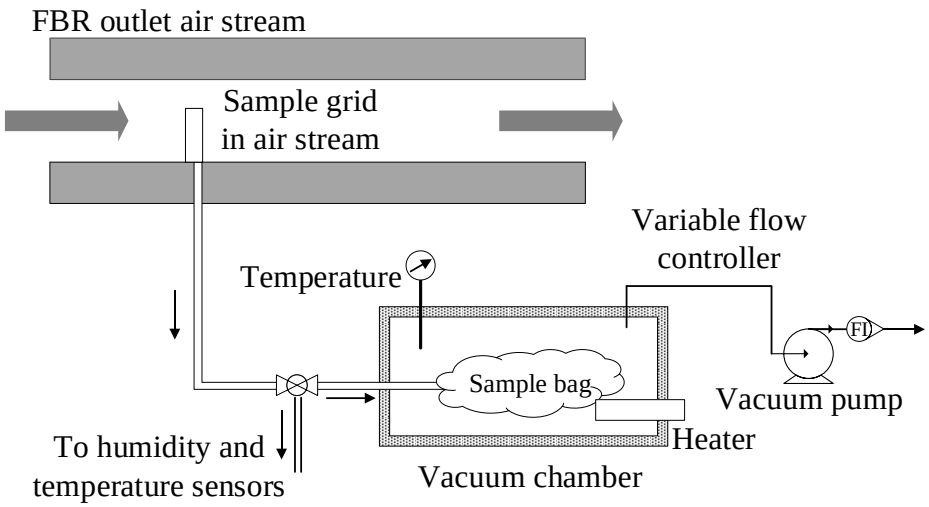

Figure 4.6. Bag sampling setup for humidity measurement.

The schematic and photograph of the experimental setup developed for the bag sampling method are shown in the Figure 4.6 and Figure 4.7. The setup consists of a heated sampling line, a vacuum chamber with a heating pad, a vacuum pump, and a variable flow controller to adjust the sampling air flow rate. The sampling line and vacuum chamber are kept at 5°C above the dew point temperature of the air sample to avoid the possibility of water vapor condensation during the operation [12]. During the sampling process, a vacuum is created inside the box by the vacuum pump, which draws air into the sampling bag without allowing it to flow through the vacuum pump. This arrangement prevents the contamination of the sample. The specifications and details of the sampling setup are listed in Table 4.3.

Table 4.3. Instrumentation for bag sampling method.

Sl. No	Instrument	Specification/Manufacturer
1	Vacuum box	Xitech Instruments Inc. Model 1062 Maximum vacuum filling rate: 6 L/min
2	Sampling line heater	Omega flexible heaters, FGR 030 Maximum temperature: 480°C
3	Variable flow controller	Rotameter, Dwyer, 0-10 L/min, ±0.5 L/min
4	Heating Pad	BV Vacs Temperature range: -45°C to 120°C
5	PID controller	Omega PID controller CN 7500
6	Sampling bags	0.5 L Tedlar bag water vapor permeability: 9-57 g/m^2/day 0.5 L Multilayer foil bag water vapor permeability: 0.0006 g/m^2/day

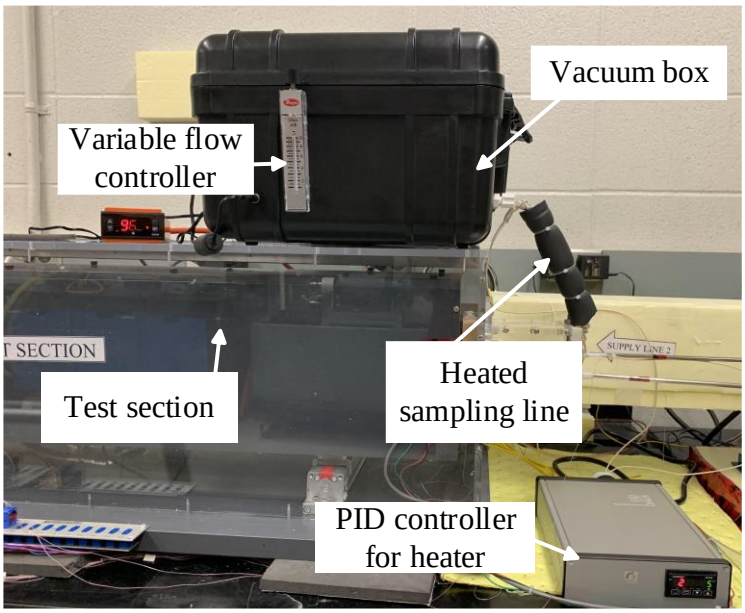

Figure 4.7. Photograph of bag sampling setup.

Sampling procedure: The sampling procedure is critical to get accurate average humidity measurements of air at the FBR outlet. Once the test facility reaches quasi-steady state [74] and

the sampling line attains a constant temperature (5°C higher than dew point temperature of the sample), the sample collection process starts from the beginning of any adsorption/desorption period by turning on the vacuum pump and stops at the end of the same period. It should also be noted that, for double-core exchangers (as shown in Figure 1.1), the sampling can be performed continuously over consecutive periods as they contain two exchangers that provide supply air continuously. After the sampling process, the bags are kept within the vacuum box (not less than 5 min) allowing air to mix and reach an equilibrium. The sampled air from the bag is ejected through a measuring line consist of humidity and temperature sensors.

The equilibrium humidity and temperature measurements during the analysis of the sampled air are shown in Figure 4.8 (a) and (b). The humidity and temperature sensors attached to the sampling line are exposed to ambient conditions before the sample analysis is initiated. The humidity sensor takes approximately 15 s (0-15 s in Figure 4.8 (a)) to measure the true relative humidity of the air sample, and it records constant measurements after the initial transient region. This transient region (highlighted in Figure 4.8 (a)) at the beginning of analysis is due to the slow response of the humidity sensor. The absolute humidity of the collected sample is determined using three different criteria, as reported in Table 4.4. Typically, the difference between absolute humidity results estimated using criteria 2 and 3 lies within the experimental uncertainty. However, there is a possibility of humidity measurements variations due to leakages or random variations in temperatures inside the bag. Therefore, criterion 2 has been used to determine the average humidity ratio during the sampling process. It should also be noted that the temperature of sampled air remains nearly constant and equal to the surroundings during this analysis.

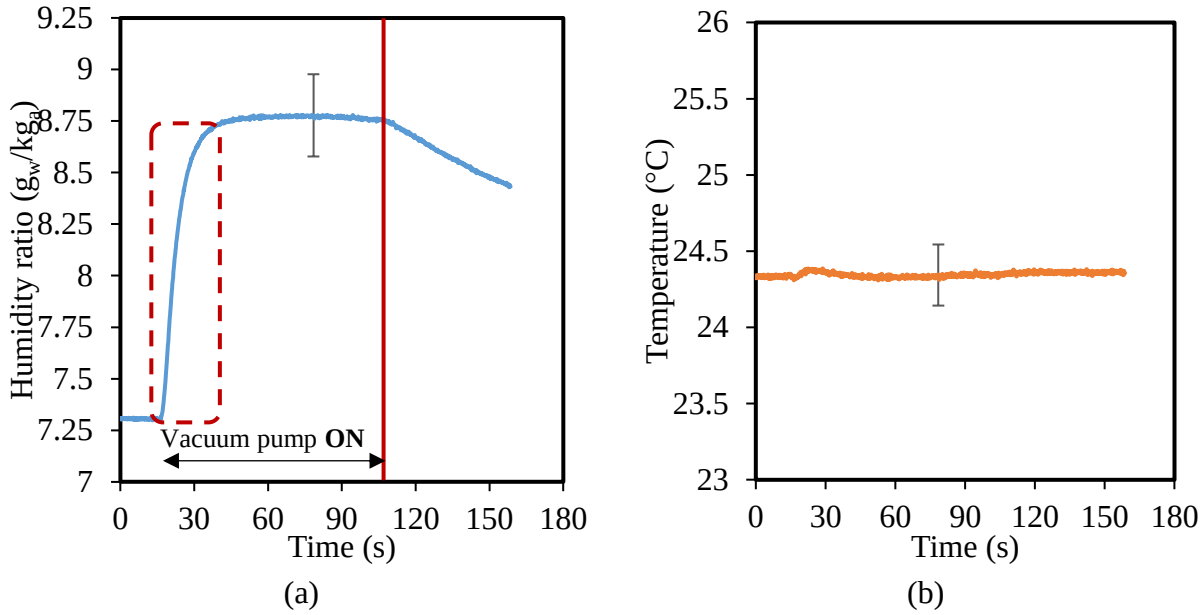

Figure 4.8. Measured (a) humidity ratio and (b) temperature of sampled air during the sample analysis.

Table 4.4. Comparison of different criteria used to estimate the average humidity during the bag sampling analysis.

No.	Criteria and description	Measured humidity ratio ($\overline{W}$) ($U_{\overline{W}} = 0.2$ g_w/kg_{air})
1	Average humidity ratio is determined by the temporal average of sensor measurements during the entire period of sampling analysis (vacuum pump ON in Figure 4.8(a))	8.42
2	Average humidity ratio is determined by temporal average of sensor measurements satisfying $\left\|\frac{W_i - W_f}{W_f}\right\| \leq 0.01$ where W_i is the instantaneous humidity at time 'i' during the sample analysis and W_f is the humidity corresponding to the time at which the vacuum pump is turned off (end of the sampling process)	8.75

3	Maximum or minimum humidity ratio during the sampling analysis (maximum; when $W_{surroundings} < W_{sample}$ and minimum; when $W_{surroundings} > W_{sample}$)	8.78

Tedlar bags [97] and multilayer foil bags [98] are used for collecting the air during the sampling process. Tedlar bags are made of polyvinyl fluoride, an inert plastic material, and are recommended for single-use applications. The multilayer foil bags are inert, moisture-tight, and reusable. In order to verify the accuracy of the BSM, a constant humidity air is supplied through supply line 1 without placing the exchanger in the test section.

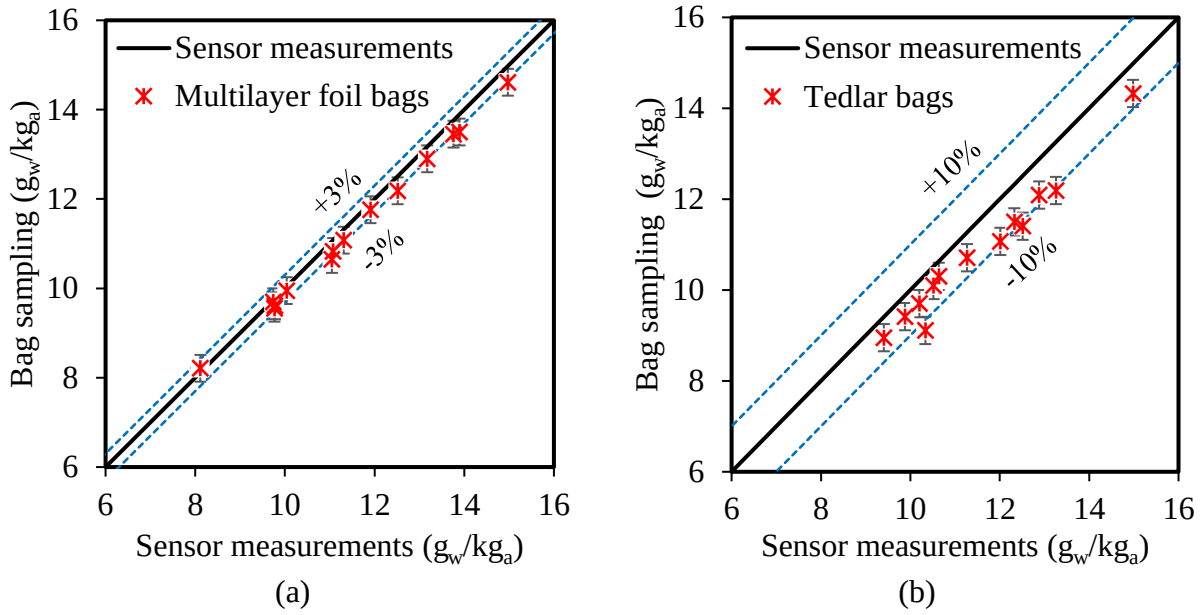

Figure 4.9. BSM results (average humidity) from (a) Multilayer foil bags (b) Tedlar bags.

Figure 4.9 shows the humidity ratio measurements using Tedlar and multilayer foil bags. The difference between the sensor measurements and the BSM is less than 3% for foil bags for all the cases, whereas it is as high as 10% for Tedlar bags. The humidity ratio measured from the sensors and multilayer foil bags falls within the experimental uncertainty limits. The moisture loss in the

Tedlar bag could be due to the adsorption of water vapor by the Tedlar material, the humidity gradient between the bag and the surroundings, resulting in diffusion of water vapor to the environment, or moisture condensation at the valve opening. The practical challenges in implementing BSM are included in Appendix D of this thesis.

4.5 UNCERTAINTY ANALYSIS

The total uncertainty (U) in a measurement is determined from systematic (B_x) and random (P_x) uncertainties for 95% confidence intervals according to the ASME PTC standard 19.1 [53].

$$U = \sqrt{P_x{}^2 + B_x{}^2} \tag{4.3}$$

The random uncertainties (P_x) associated with all measured parameters are determined using Eq. (4.4),

$$P_x = \frac{t_s \cdot SD}{N}, \tag{4.4}$$

where t_s is the student t- factor at a 95% confidence interval for a degree of freedom of (N-1), and SD is the standard deviation of the measurements. Calibration and data reduction errors are included in the systematic uncertainty. The overall uncertainty in latent effectiveness is determined using the method of uncertainty propagation rules as follows [54],

$$U_R = \left[\sum_{i=1}^{j} \left(\frac{\partial R}{\partial p_I} U_{p_i}\right)^2\right]^{0.5}, \tag{4.5}$$

where U_R, U_{p_I}, and $\partial R / \partial p_I$ are the overall uncertainty, uncertainty associated with measurement property P_i and the sensitivity coefficient of measurement property P_i, respectively.

4.6 VERIFICATION OF TEST RESULTS

The proposed experimental method is verified using a validated numerical model and a correlation from the literature. The model and correlation are summarized in the following subsections.

4.6.1 Numerical model

In the FBR, the two airstreams alternatively flow through the heat exchanger, which consists of numerous channels. Thus, the governing equations, assumptions, and boundary conditions will be presented for a representative channel. The schematic of the cross-section of the representative channel is shown in Figure 4.10. During the hot and humid period, energy is absorbed (solid lines in Figure 4.10) into the matrix, which is then released to the cold and dry airflow in the subsequent period (dashed line in Figure 4.10)). The 1-D governing equations introduced by Simonson and Besant [30], [57] for energy wheels are adopted in this model.

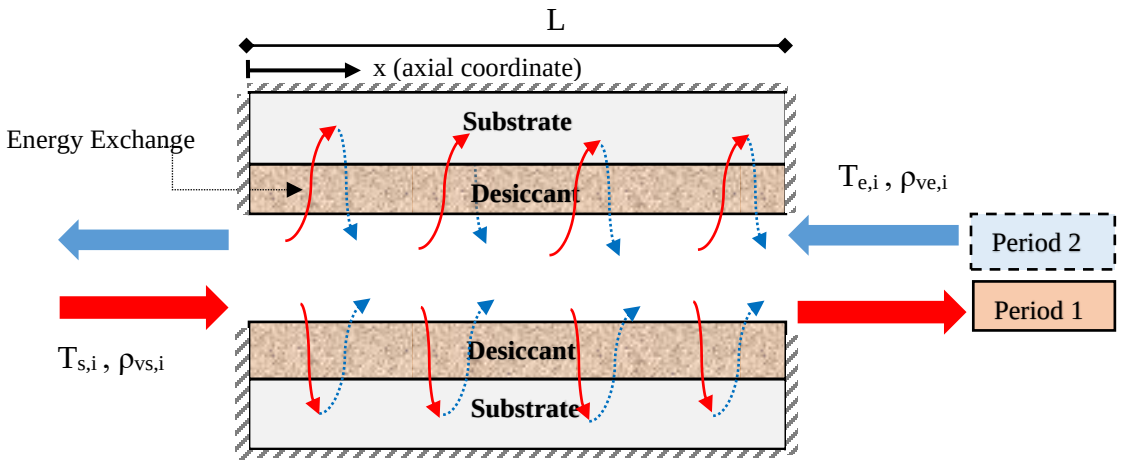

Figure 4.10. Schematic of the numerical domain considered for modeling the moisture transfer process in FBRs.

The conservation of mass in the air stream results in two continuity equations for water vapor and dry air as follows:

$$A_g \frac{\partial \rho_v}{\partial t} + \frac{\partial}{\partial x}\left(\rho_v V_{ch} A_g\right) + \dot{m}' = 0 \tag{4.6}$$

$$\frac{\partial \rho_a}{\partial t} + \frac{\partial}{\partial x}\left(\rho_a V_{ch}\right) = 0 \tag{4.7}$$

where V_{ch}, $\dot{m}'$, A_g ρ_v and ρ_a are mean airflow velocity, rate of phase change per unit of length, the cross-sectional area of the channel, and the density of water vapor and dry air, respectively. The conservation of mass for the desiccant is as follows:

$$\dot{m}' = \rho_{(d,dry)} A_d \frac{\partial W}{\partial t}, \tag{4.8}$$

where $\rho_{(d,dry)}$, A_d and W are the density of dry desiccant, the surface area of desiccant, and mass fraction of water in the desiccant, respectively. The energy conservation equations for coupled heat and moisture transfer in regenerators for the airstream and matrix are as follows:

$$\rho_g C_{P_g} A_g \frac{\partial T_g}{\partial t} + V_{ch} \rho_g C_{P_g} A_g \frac{\partial T_g}{\partial x} - \dot{m}' h_{ad} \eta + h \frac{A_{ht}}{L} (T_g - T_m) = 0 \tag{4.9}$$

$$\rho_m C_{P_m} A_m \frac{\partial T_m}{\partial t} - \dot{m}' h_{ad} (1 - \eta) - h \frac{A_{ht}}{L} (T_g - T_m) = \frac{\partial}{\partial x} \left(k_m A_m \frac{\partial T_m}{\partial x} \right) \tag{4.10}$$

where t, x, C_p, k, h, L and T are time, axial coordinate, specific heat, thermal conductivity, convective heat transfer coefficient, length of channel and temperature, respectively. Subscripts 'g' and 'm' are used to represent the gas and matrix (desiccant and aluminum) variables, respectively. A_{ht} and A_m represent the heat transfer surface area and cross-sectional area of the exchanger plate, respectively. Heat and mass transfer at the ends of the channel is assumed to be negligible, and appropriate boundary conditions have been applied to solve Eqs. (4.6)–(4.10) numerically. Further details on the numerical procedure and validations are provided in [85].

4.6.2 Literature correlation

The regenerator correlation developed by Simonson and Besant [30] is used to predict the effectiveness of the FBRs (Eqs. (4.11)-(4.13)). The sensible, latent, and total effectiveness are expressed as a function of number of transfer unit (NTU_o), heat capacity rate ratio (Cr*), maximum moisture content (W_m), average relative humidity ($ø_{avg}$), the slope of sorption isotherm $\left[\frac{\partial u}{\partial \varphi}\right]_{\varphi\ ave}$,

operating condition factor (H*) and fraction of the phase change energy that is delivered directly to the air (η). The correlations accurately predict the sensible, latent and total effectiveness within ±2.5% for $3 \leq Cr^* \leq 10$ and $2 \leq NTU_o \leq 10$, $0.1 \leq W_m \leq 0.5$, $0 \leq \eta \leq 0.1$, $-6 \leq H^* \leq 6$, $1 \leq \frac{Cr^*}{Cr_m^*} \leq 5$, C=1, and $C^* = 1$ conditions [30], [88]. The effect of axial heat conduction through the matrix is accounted by following the method reported by Shah [14]:

$$\varepsilon_L = \frac{NTU_o}{1+NTU_o}\left[1 - \frac{1}{0.54\,(Cr_m^*)^{0.86}}\right] \times \left[1 - \frac{1}{(NTU_o)^{0.51}(Cr^*)^{0.54}H^*}\right] \tag{4.11}$$

$$\varepsilon_S = \frac{NTU_o}{1+NTU_o}\left(1 - \frac{1}{7.5Cr^*}\right) - \left[\frac{0.26\left(\frac{Cr^*}{W_m Cr_m^*}\right)^{0.28}}{7.2\,(Cr^*)^{1.53} + \frac{210}{(NTU_o)^{2.9}} - 52} + \frac{0.31\eta}{(NTU_o)^{0.68}}\right] H^* \tag{4.12}$$

$$\varepsilon_t = \frac{\varepsilon_s + \varepsilon_l H^*}{1+H^*} \tag{4.13}$$

where,

$$Cr^* = \frac{MC_{p,m}/P}{\dot{m}c_{P,a}}, \qquad 3 \leq Cr^* \leq 10 \tag{4.14}$$

$$Cr_m^* = \frac{M_{d,dry}/P}{\dot{m}_a} \tag{4.15}$$

$$Cr_{mt}^* = (Cr_m^*)^{0.58}\, W_m^{0.33} \left(\left[\frac{\partial u}{\partial \varphi}\right]_{\varphi\ ave}\right)^{0.2} (Cr^*)^{1.13} \left[\frac{e^{\frac{1482}{T_{ave}}}}{47.9} - 1.26\,(\varphi_{ave})^{0.5}\right]^{4.66} \tag{4.16}$$

$$H^* = 2500\frac{\Delta W}{\Delta T}, \quad -6 \leq H^* \leq 6\,. \tag{4.17}$$

4.7 RESULTS

The experiments are conducted at two different conditions based on the inlet properties of the air streams as follows:

(1) Isothermal tests: The temperatures of both inlet airstreams are the same with different humidity ratios (i.e., $\Delta T_{inlet} = 0$, $\Delta W_{inlet} \neq 0$). For this case, the moisture exchange through the FBR is quantified using latent effectiveness.

(2) Non-isothermal tests: The experiments are performed in such a way that the humidity and temperature of both inlet airstreams are different ($\Delta T_{inlet} \neq 0$, $\Delta W_{inlet} \neq 0$) and in this case, heat and moisture will be transferred simultaneously between the exchanger and airstreams. The sensible, latent, and total effectiveness are used to quantify the performance of the FBR.

To measure the time-varying (transient) humidity and temperature at the FBR outlets accurately, the temperature and humidity sensors must respond faster than the FBR. Therefore, the response (or time constants) of the humidity and temperature sensors are measured when they are exposed to a step-change in inlet humidity (isothermal) and temperature (non-isothermal) test conditions.

4.7.1 Sensor time constants

The response time of instruments indicates how fast they can respond to a change in the input conditions and is quantified using time constant. For the case of humidity sensors, the time constant refers to the time required for it to attain 63.2% of the final humidity value when exposed to a step-change in the inlet humidities. Figure 4.11 shows the transient response of humidity sensors when exposed to a step-change in humidity ratio (i.e., $\Delta T = 0$, $\Delta W \neq 0$). The sensors located inside the test section (exchanger sensors) are used to measure the time constants. It should be noted that these experiments are performed without placing the exchanger inside the test section as it influences the response of the humidity sensors. In these experiments, the inlet humidity was changed by 30%, and the face velocity and temperature of the airstreams were maintained at 1.8 m/s and 23 °C, respectively. The test data were correlated with an exponential function shown in

Eq. (4.18) using the trust region optimization algorithm in MATLAB R2013a. The least-square technique is used to fit the test data with the calculated humidity values. The time constant values and the coefficient of determination (R^2) are reported in Table 4.5, and the high value of R^2 confirms the close fitting of the exponential function to the experiment data.

$$f(t) = \begin{cases} 1 - e^{-\frac{t}{\tau}} \\ e^{-\frac{t}{\tau}} \end{cases} \tag{4.18}$$

Table 4.5. Humidity sensor time constant data for a step-change in inlet temperature.

	ΔRH_{step}	Time constant (s)	R^2
Step increase	30 ± 1.5%	5.09	0.981
Step decrease		5.14	0.983

The transient response of the humidity and temperature sensors at the FBR outlet is also measured when they are exposed to a step-change in humidity and temperature (i.e., $\Delta T \neq 0$, $\Delta W \neq 0$). Figure 4.12 (a) shows the measured normalized humidity ratio and temperature response at the test section outlet. The humidity sensor's behavior is significantly different in this experiment compared to the isothermal tests (i.e., $\Delta T = 0$, $\Delta W \neq 0$). The measured outlet humidity ratio is nearly 1.5 times higher than the inlet humidity ratio for the initial 5 to 50 s, which is theoretically incorrect. Typically, the time constant of humidity sensors is specified for isothermal conditions. This unexpected response at non-isothermal conditions may be attributed to the change in dielectric constant of capacitive humidity sensor because of the simultaneous changes in humidity and temperature. Similar behavior for capacitive humidity sensors has been reported previously in the literature [99]. Figure 4.12 (b) shows the transient response of the thermocouples for the same experiment. The step-change in relative humidity did not influence the temperature measurements as the outlet temperature quickly follows the inlet conditions.

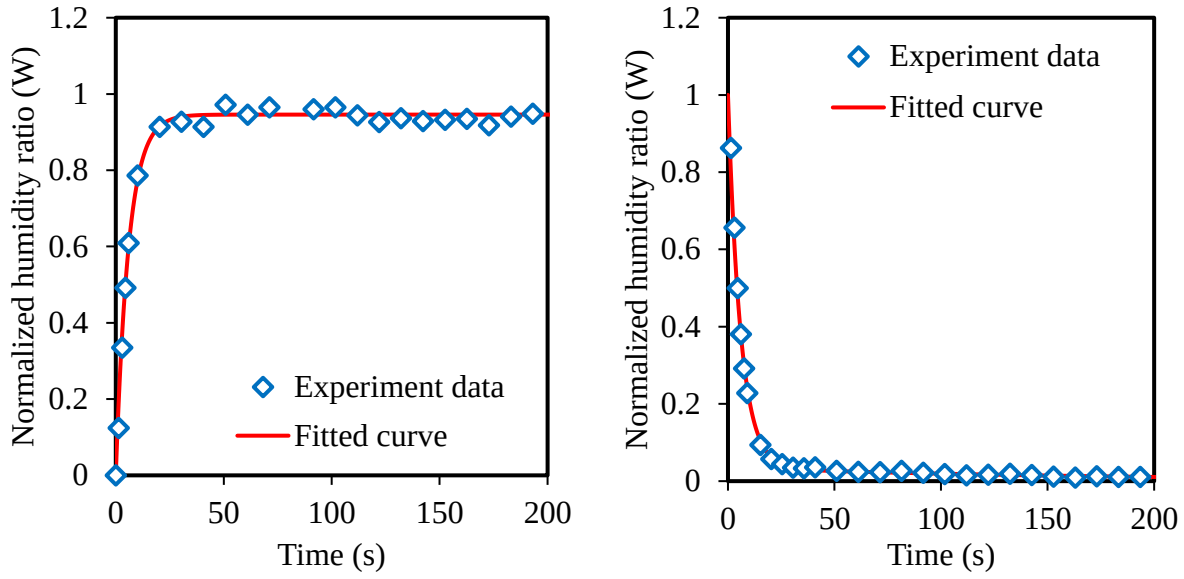

Figure 4.11. The response of humidity sensors when they exposed to a step change in humidity conditions (ΔT_{step} = 0°C, ΔRH_{step} = 30%).

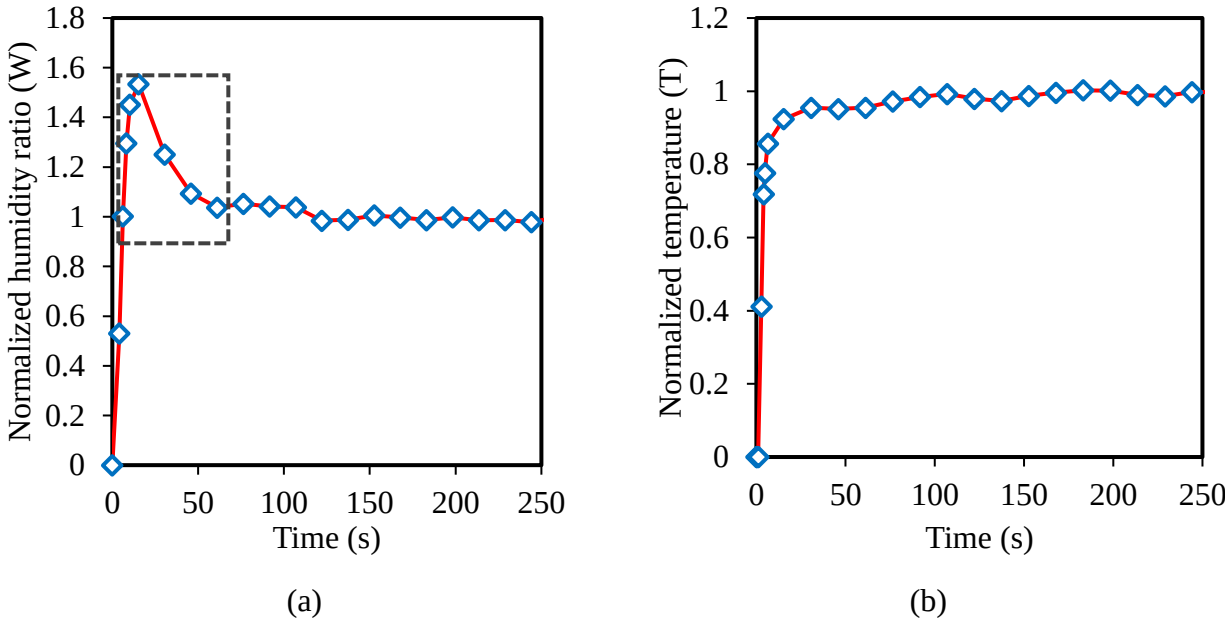

Figure 4.12. The response of (a) humidity and (b) temperature sensors when they are exposed to a step increase in humidity and temperature conditions (ΔT_{step} = 12°C, ΔRH_{step} = 30%).

4.7.2 Isothermal test results ($\Delta T = 0$, $\Delta RH \neq 0$)

4.7.2.1 Test facility water vapor and energy balances

Water vapor and energy balances were performed in every experiment to ensure that the moisture and energy were conserved within the experimental uncertainty limits. According to ASHRAE Standard 84 [12], [100], the experiments should satisfy Eqs. (4.19) and (4.20) for the operating conditions with no condensation and frost formation.

$$\text{Water vapor: } \left|\frac{\dot{m}_1 W_1 - \dot{m}_2 W_2 + \dot{m}_3 W_3 - \dot{m}_4 W_4}{(\dot{m}_1, \dot{m}_2)_{min}\ (W_1 - W_3)}\right| < 0.2 \tag{4.19}$$

$$\text{Total energy: } \left|\frac{\dot{m}_1 h_{e_1} - \dot{m}_2 h_{e_2} + \dot{m}_3 h_{e_1} - \dot{m}_4 h_{e_4}}{(\dot{m}_1, \dot{m}_2)_{min}\ (h_{e_1} - h_{e_3})}\right| < 0.2 \tag{4.20}$$

Equations. (4.19) and (4.20) represent that the latent effectiveness and total effectiveness determined during adsorption/desorption should be within ±20% agreement. Figure 4.13 shows the latent effectiveness during the adsorption and desorption periods determined from the exchanger and duct sensor measurements for several test conditions. The maximum difference between the effectiveness estimated from adsorption and desorption is ±9% for the exchanger sensors and ±7% for the duct sensors, respectively. The experimental uncertainty in latent effectiveness is ±5-7% depending on the test conditions. Similarly, an energy balance was also performed to calculate the total effectiveness using Eq. (4.1) and it was found that the results from the exchanger and duct sensors during adsorption and desorption were within ± 10% agreement. The differences in water vapor mass and energy balances could be due to the experimental uncertainties and heat/ moisture interaction between the exchanger and surroundings.

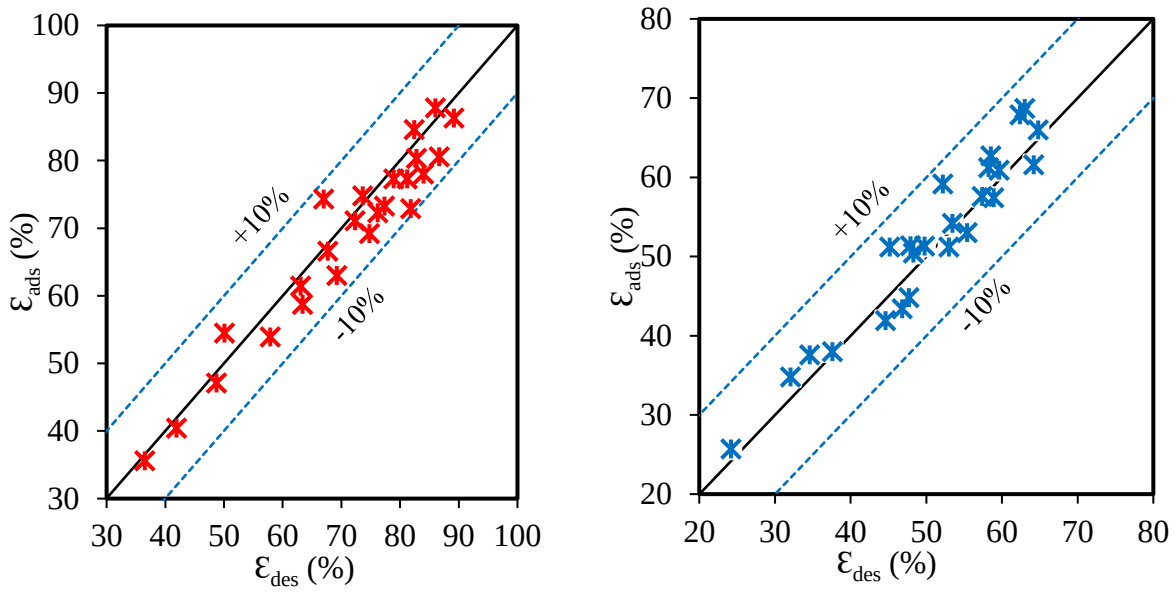

Figure 4.13. Test facility water vapor mass balance from (a) exchanger sensors and (b) duct sensors measurements.

4.7.2.2 Humidity measurements and latent effectiveness

Humidity sensor measurements: During moisture transfer experiments, the humidity at the outlets of the FBR varies with time and reaches a quasi-steady state condition, after which it follows a periodic humidity profile. The FBR outlet humidity during the adsorption and desorption periods measured using the exchanger and duct sensors is presented in Figure 4.14. During the adsorption period, the desiccant adsorbs water vapor from the airstream, and thus the humidity at the outlet is lower than at the inlet. The maximum moisture transfer occurs at the beginning of the period. As time progresses, desiccants gradually get saturated and attain equilibrium with the inlet airstream. During the desorption period, the desiccant releases the stored water vapor to the incoming dry airstream, resulting in the humidification of dry inlet air.

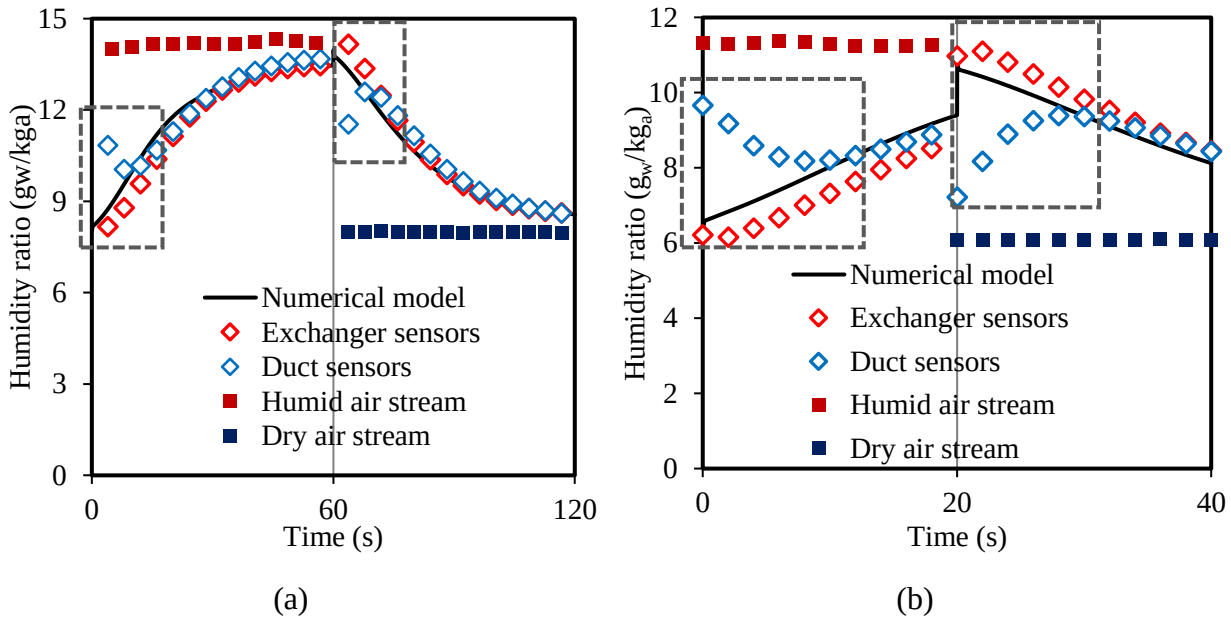

Figure 4.14. Comparison of the humidity profiles obtained from the duct and exchanger sensors with the numerical model for two different operating conditions ((a) face velocity, V_f : 1.15 m/s, period, P: 60 s (b) face velocity, V_f: 1.15 m/s, period, P: 20 s).

At the beginning of each period, Figure 4.14 (a) and (b)), the humidity measurements from the exchanger and duct sensors are different, and gradually they approach similar values within the experimental uncertainties. This deviation in the initial transient region (highlighted with dashed rectangles in Figure 4.14) is due to the slow response of the humidity sensors and the conditions they were exposed to during the previous period. Prior to the adsorption period shown in Figure 4.14, the exchanger sensors were exposed to the dry air stream, and the duct sensors were exposed to the humid air stream. A similar observation has been previously reported for the outlet temperature measurements of FBRs [74], [101], [102]. The effect of temperature transients on the sensible effectiveness was eliminated by fitting a linear curve to the temperature profile [74], [101]. However, the same procedure cannot be applied here due to non-linear humidity outlet profiles and challenges in identifying the transient region.

The latent effectiveness obtained from the duct and exchanger sensor measurements during the quasi-steady state operation of the FBR is shown in Figure 4.15 (a). For a period of 60 s, the latent effectiveness determined from the duct sensors and exchanger sensors agrees within experimental uncertainty bounds. However, the difference increases for shorter operating periods. For example, the difference in effectiveness is about 23% for a period of 15 s as shown in Figure 4.15 (b). As explained previously, the humidity sensor's transient response causes incorrect humidity measurements at the beginning of each period and results in significant errors in the computation of latent effectiveness.

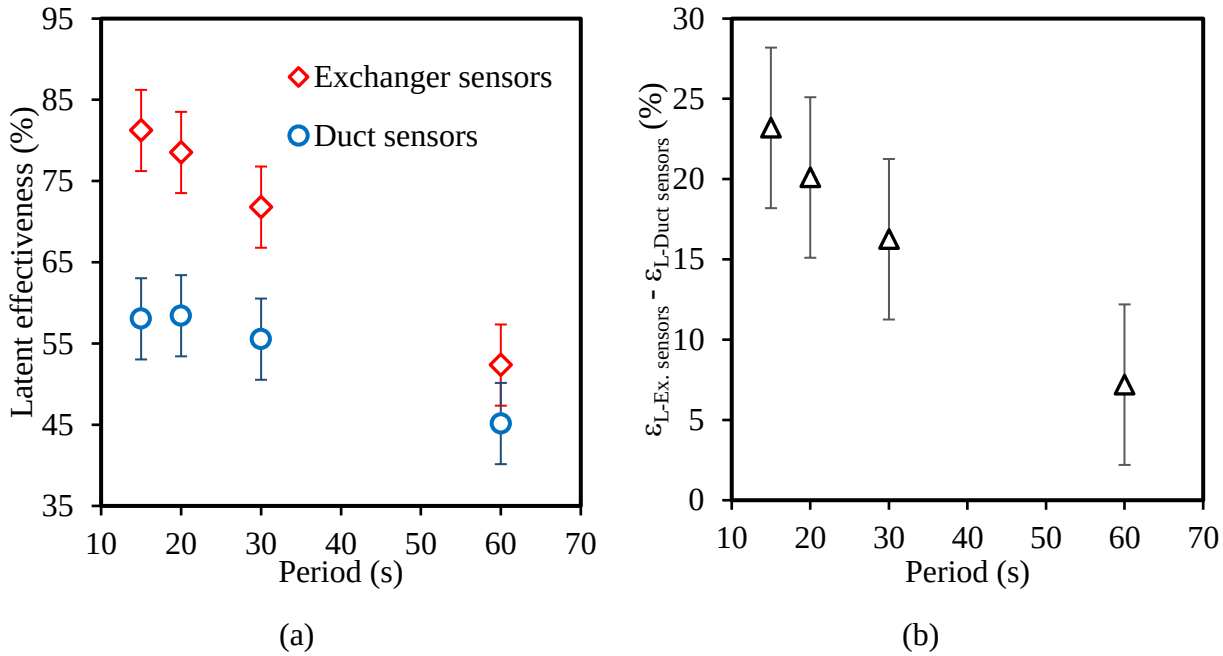

Figure 4.15. Latent effectiveness determined from the exchanger and duct sensors and their differences at different periods.

Bag sampling method (BSM) results: The slow response of the humidity sensors causes errors in latent effectiveness estimation, as explained in the previous section. ASHRAE 84 [12] and CSA C439-18 [13] test standards recommend the BSM for accurate relative humidity measurements at the FBR outlets. The latent effectiveness obtained through the BSM will not have any transient

errors, as it is not based on instantaneous humidity measurements. The BSM measures the equilibrium humidity only after the samples attain an equilibrium condition (i.e., humidity of the sample remains constant with time), and these measurements are used to determine the latent effectiveness. The guidelines provided by the test standards were followed during the sampling process and the latent effectiveness estimated from six different adsorption and desorption periods is shown in Figure 4.16. It is clear from Figure 4.16 that the latent effectiveness results agree with each other within the experimental uncertainty limits. The repeated sampling confirms the repeatability of the BSM and reduces the random uncertainty in the humidity measurements. It should also be noted that criterion 2 (described in Table 4.4) is used for estimating the average humidity ratio, which is also used in the latent effectiveness calculations.

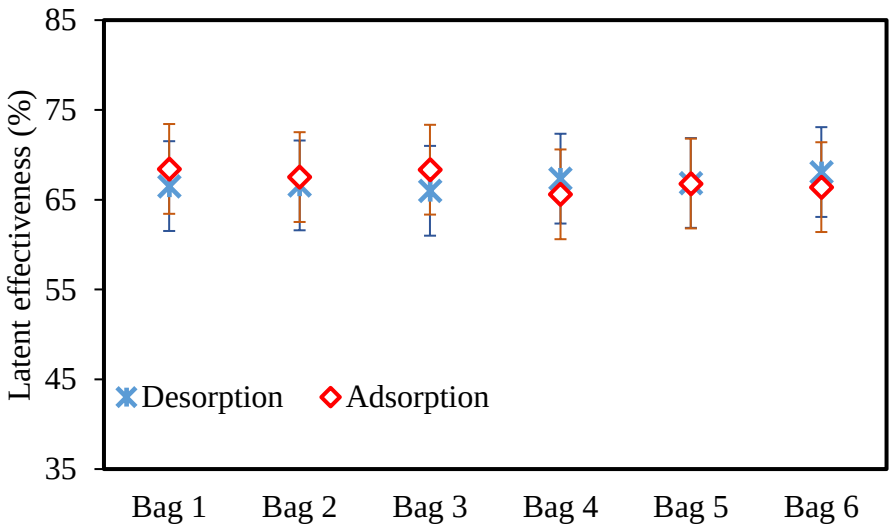

Figure 4.16. Latent effectiveness obtained from the BSM during adsorption and desorption.

Sensor measurements correction: From analyzing several experimental and numerical humidity profiles, it is inferred that the initial transient behavior of the humidity sensors adversely affects the duct and exchanger sensor measurements. The duct sensors always measure lower values and the exchanger sensors measure higher values than the actual humidity obtained from the numerical

model. Therefore, an average of the duct and exchanger sensor measurements could minimize the effect of these sensor transients. Figure 4.17 shows the comparison of latent effectiveness obtained from the average sensor measurements (average of duct and exchanger sensors), numerical model, and BSM. The maximum difference between average effectiveness from the numerical model and the BSM is approximately 3%. This method is verified by repeating experiments for different test conditions ranging from 350 L/min to 700 L/min (face velocity, V_f : 1-2 m/s, NTU_o: 1.8 – 4).

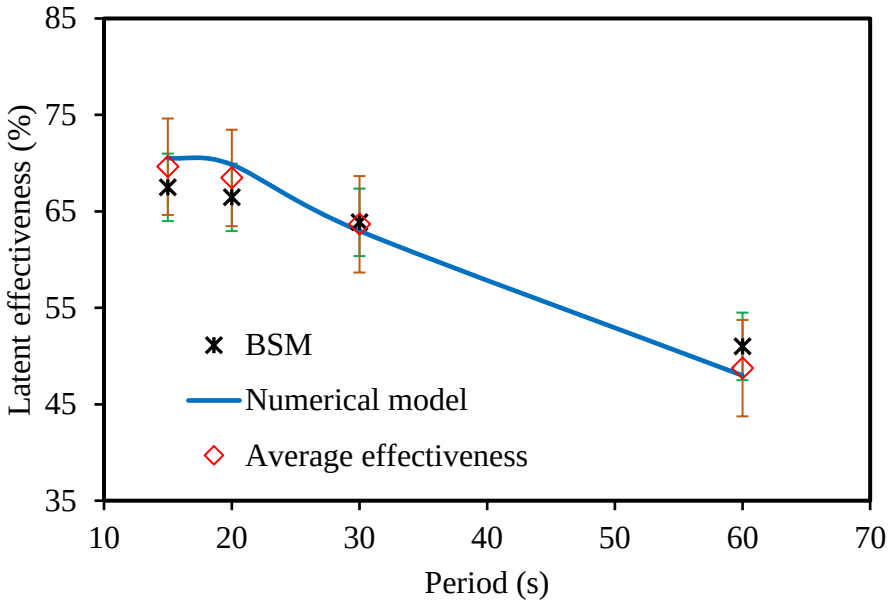

Figure 4.17. Comparison of latent effectiveness between average of sensor measurements, numerical model, and BSM.

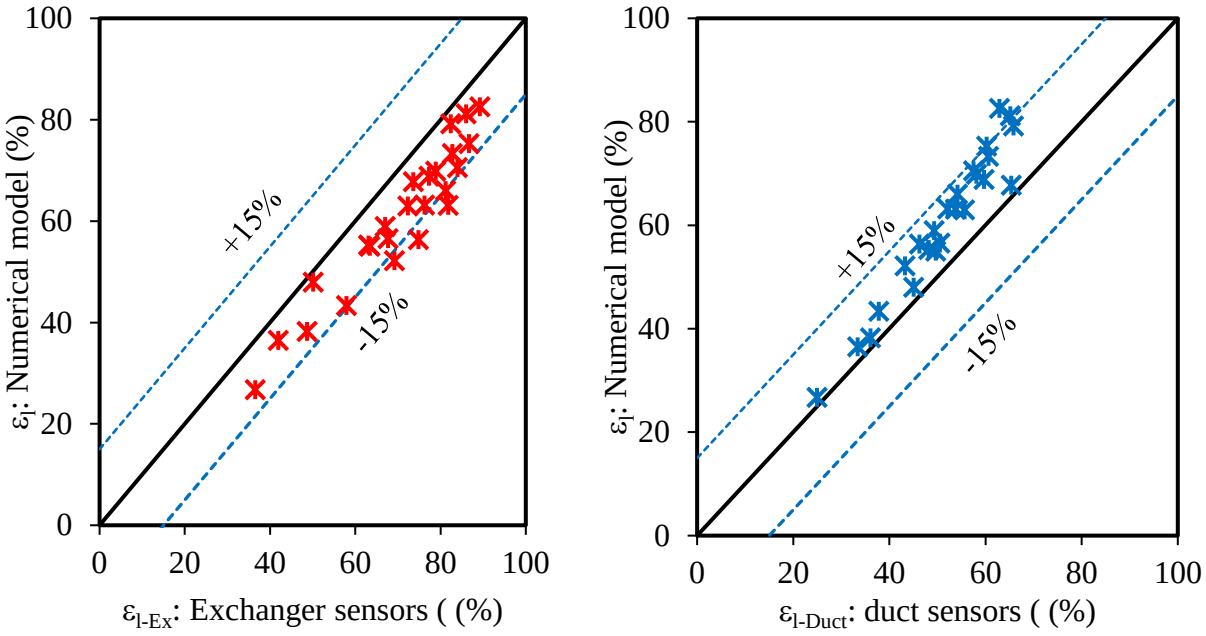

Figure 4.18. Comparison of latent effectiveness obtained from (a) exchanger sensors and (b) duct sensors with numerical model.

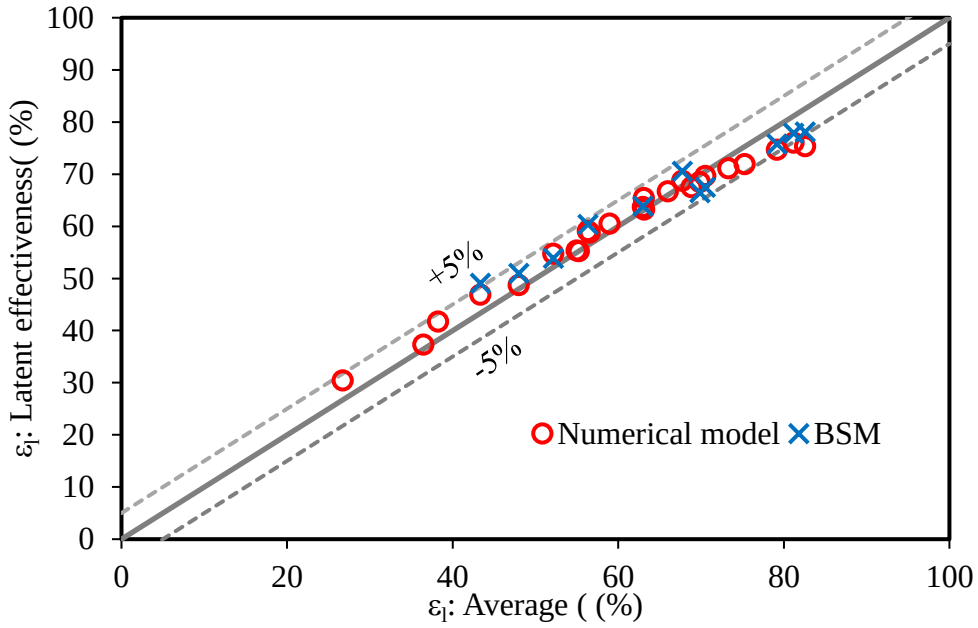

Figure 4.19. Comparison of average latent effectiveness (average of $\varepsilon_{l\text{-}duct}$ and $\varepsilon_{l\text{-}Ex}$) with BSM and numerical model.

Figure 4.18 shows the comparison of latent effectiveness obtained from the duct (Figure 4.18 (a)) and exchanger sensors (Figure 4.18 (b)) with numerical results for different test conditions (face velocity: 1-2 m/s, NTU_o: 1.8 – 4). The exchanger sensors always overpredict and the duct sensors underpredict the latent effectiveness with a maximum deviation of 15-20% (approximately) when compared to the numerical model. The average latent effectiveness (average of duct and exchanger sensors) is in good agreement within ±5% with the effectiveness determined from the BSM numerical results shown in Figure 4.19. Both the BSM and averaging methods can predict latent effectiveness accurately. However, unlike the BSM, the sensors can perform real-time monitoring and provide instantaneous outlet humidity profiles without additional instrumentation.

4.7.2.3 Comparison of test results using nondimensional performance parameters

The physical dimensions and actual flow rates in full-scale FBRs can differ from the small-scale exchanger and test conditions. The results from small-scale experiments cannot be applied directly to full-scale FBR units. However, the small-scale and full-scale exchanger's latent effectiveness will be the same when both operate at the same NTU_o, Cr^*, H^* and Cr^*_m conditions. The NTU_o, Cr^*, H* and Cr^*_m of full-scale FBRs can be achieved in small-scale tests by varying flow rate, exchanger length, number of plates, inlet flow conditions and amount of desiccant coating.

Figure 4.20 shows the latent effectiveness comparison between the numerical model, BSM and sensor measurements for two different NTU_o conditions. Sorption isotherm data and physio-geometrical properties of the exchanger are used in the model, and the results agree within ±3.5 % with the test data for all tested conditions. The difference between numerical results and experiments could be due to (i) sensor transients and experimental uncertainty, (ii) simplified assumptions in the numerical model such as one-dimensional heat and moisture transfer and instantaneous diffusion of water vapor in the desiccant coated plates, and (iii) uncertainties in the

thermophysical properties of desiccant materials. The maximum deviation from the BSM with experiments and the numerical model is less than 4% for all the test conditions. These deviations could be because of the loss/gain of water vapor from the surroundings or condensation during the sampling process, experimental uncertainties, or sensor transients. The good agreement between the numerical results with test data and the BSM confirms the validity of these test methods. The uncertainty in latent effectiveness is approximately 4.5-7% depending on the test conditions. This method can be used in the future for latent effectiveness testing of FBRs and for developing new desiccant materials for building energy recovery systems.

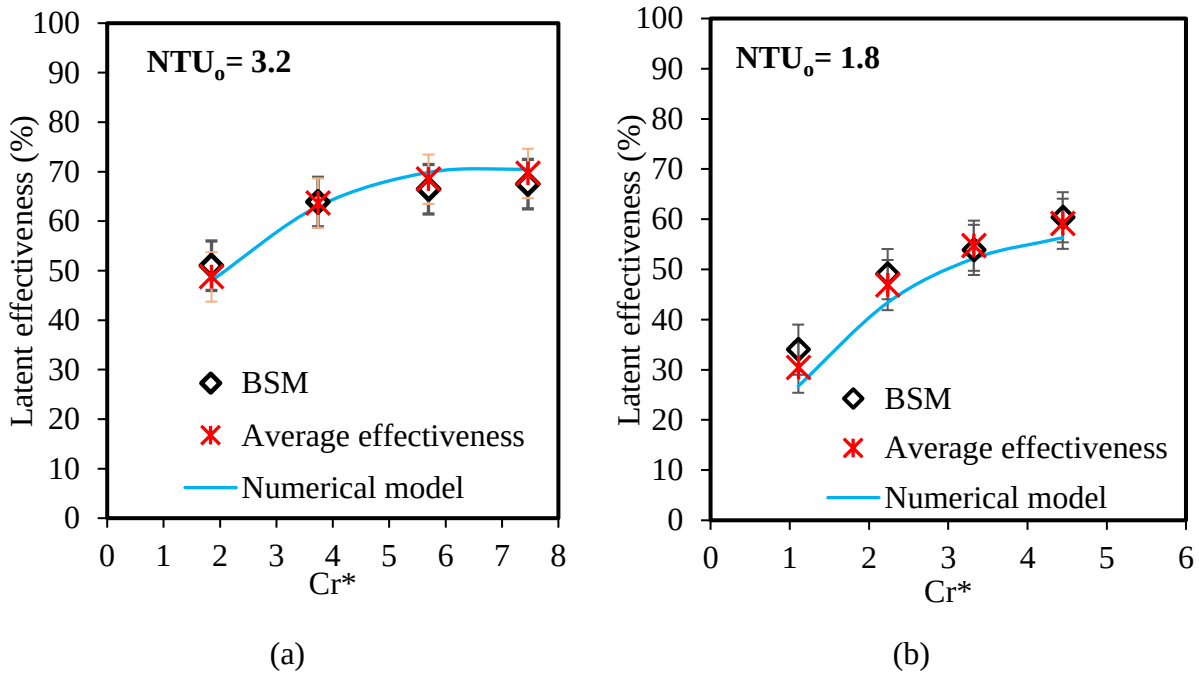

Figure 4.20. Comparison of latent effectiveness obtained from experiments with numerical model, literature correlation [30] and the BSM.

4.7.2.4 Applicability literature correlation for FBRs

Simonson and Besant have developed correlations for sensible, latent, and the total effectiveness of regenerators using more than 600 simulated data points [30], [103], [104] and validated for $2 < NTU_o < 10$ and $3 < Cr^* < 10$. This correlation is applied to determine the latent effectiveness of

the desiccant coated small-scale exchanger. The thermophysical properties of the exchanger and desiccants, the sorption isotherm, and the test conditions are the required inputs for the correlation. The description of correlation parameters with their values for the small-scale exchanger is listed in Table 4.6.

Figure 4.21 shows the comparison of the test results with the correlation from the literature. There is a nearly 10% difference observed between the test data and correlation. It should be noted that the slope and the maximum moisture uptake estimated for this analysis are based on the entire range of P/P_o (0 to 1). However, the FBR never operates in the entire range of P/P_o; hence two modifications are applied to this correlation based on the FBRs test condition:

1. The slope of the sorption curve $\left(\frac{\partial u}{\partial \phi}\right)_{\varphi \text{ ave}}$ is evaluated by fitting a linear curve on the operating region of the sorption isotherm.
2. The maximum moisture uptake (W_m) is calculated by fitting a linear curve to the sorption isotherm (corresponds to the operating region) and extrapolating it to the P/P_o=1 condition.

Table 4.6. Input to literature correlation parameters for the small-scale exchanger.

Parameter	Symbol (unit)	Values	References
Convective heat transfer coefficient	h (W/m^2 K)	62 ± 0.5	Ref. [28]
Total area of heat transfer	A_s (m^2)	0.48 ± 0.008	Measured
Mass of coated matrix	M (g)	987	Measured
Specific heat capacity of matrix	$c_{p,m}$ (J/kg K)	893	Al-3003
Total mass of dry desiccant coated on the matrix	$M_{d,\,dry}$ (g)	45	Measured
Maximum moisture content of desiccant	W_m (g/g)	0.2	Figure 4.3

Average relative humidity	$\emptyset_{ave}$	0.45	Measured
Slope of sorption isothermal average relative humidity	$\left(\frac{\partial u}{\partial \emptyset}\right)_{\varphi\ ave}$	0.21	Fig. 7
Operating condition factor	H*	H*>>1	ΔT = 0°C

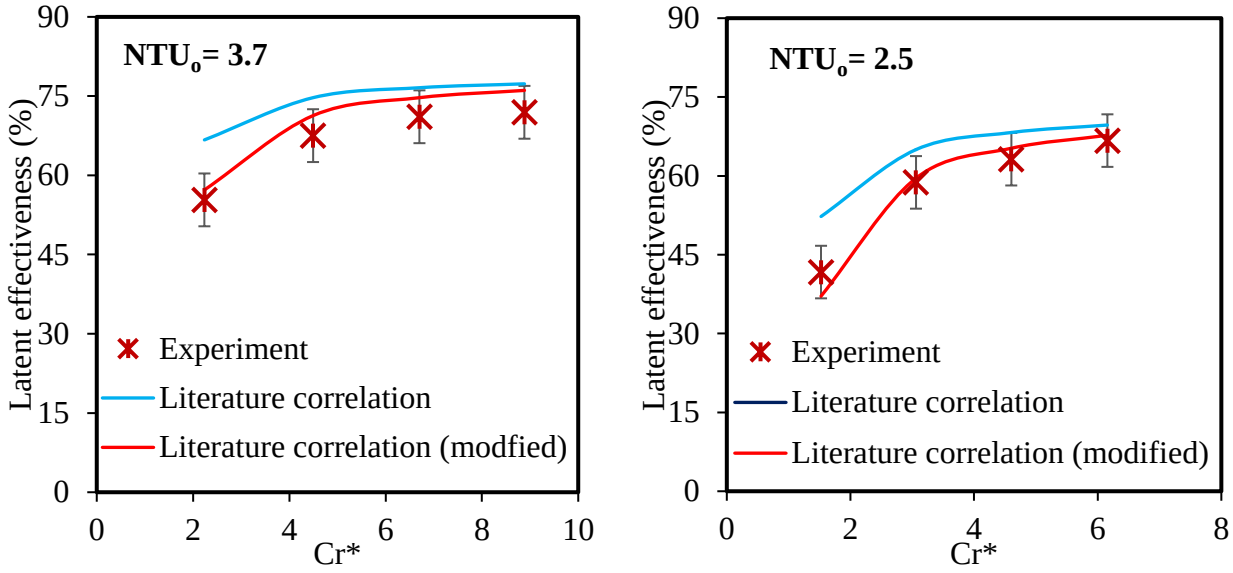

(a) (b)

Figure 4.21. Comparison of the latent effectiveness obtained from experiment and the correlation in the literature.

The latent effectiveness estimated from the correlation, experiment data, and modified literature correlation for NTU_o of 2.5 and 3.7 is shown in Figure 4.21(a) and (b). The modified correlation results agree with the test data within the experimental uncertainty limits for its applicability range. The discrepancy between the original correlation and test data is more than the test uncertainties in most conditions, whereas the modified correlation agrees within ±6 % for all the tested conditions. The difference between the correlation and test data could be due to simplified assumptions in the correlation such as the mass transfer area is taken to be the same as that of the plate area, the possibility of Lewis number (Le) > 1 because of the highly porous structure of silica

gel, and the uncertainties related to the experiments. The modified correlation can be successfully used to evaluate the performance of silica gel coated FBRs for HVAC applications.

4.7.2.5 Uncertainty analysis

ASHRAE standard 84 [12] recommends a maximum uncertainty level of 7% for the latent effectiveness of energy exchangers. For the small-scale experiments presented in this chapter (effectiveness evaluation from sensor measurements), the uncertainty in latent effectiveness results from systematic uncertainties in relative humidity, temperature, and flow rate measurements. A detailed uncertainty analysis was carried out using literature correlation [18] and considering instrumentation uncertainty. The latent effectiveness of the FBR is predicted for different operating conditions using the correlation and, the humidity at FBR outlets is calculated from Eq. (4.1). The uncertainty in humidity and mass flow rates are propagated using Eq. (4.2) for determining the uncertainty in latent effectiveness. For this analysis, the ΔRH and temperature of the airstreams are assumed to be 30% and 25°C, respectively. The uncertainty in temperature, humidity ratio and mass flow rates are ±0.2°C, ±0.2 g_w/kg_a and ±2 - 0.6% (corresponding to face velocity, V_f = 1-2.5 m/s), respectively.

The contribution of the uncertainty in mass flow rate and humidity ratio to the overall uncertainty is shown in Figure 4.22 (a). The uncertainty in latent effectiveness due to systematic uncertainty in the mass flow rate increases from 0.5-4% while NTU_o changes from 2 to 5. For a given exchanger, higher NTU_o conditions are achieved by reducing the mass flow rate. As the mass flow rate decreases, the pressure drop across the orifice plate reduces, which increases the uncertainty in flow rate, further increasing the uncertainty in latent effectiveness. The contribution of uncertainty in humidity ratio on the latent effectiveness is shown in Figure 4.23 (b). The uncertainty due to systemic error in humidity measurements contributes nearly 4-4.5% to the

uncertainty of the latent effectiveness regardless of NTU_o. condition. The uncertainty in flow rate and humidity ratio equally contributes to overall uncertainties at high NTU_o conditions, whereas the uncertainty in humidity ratio has a high impact at lower NTU_o conditions.

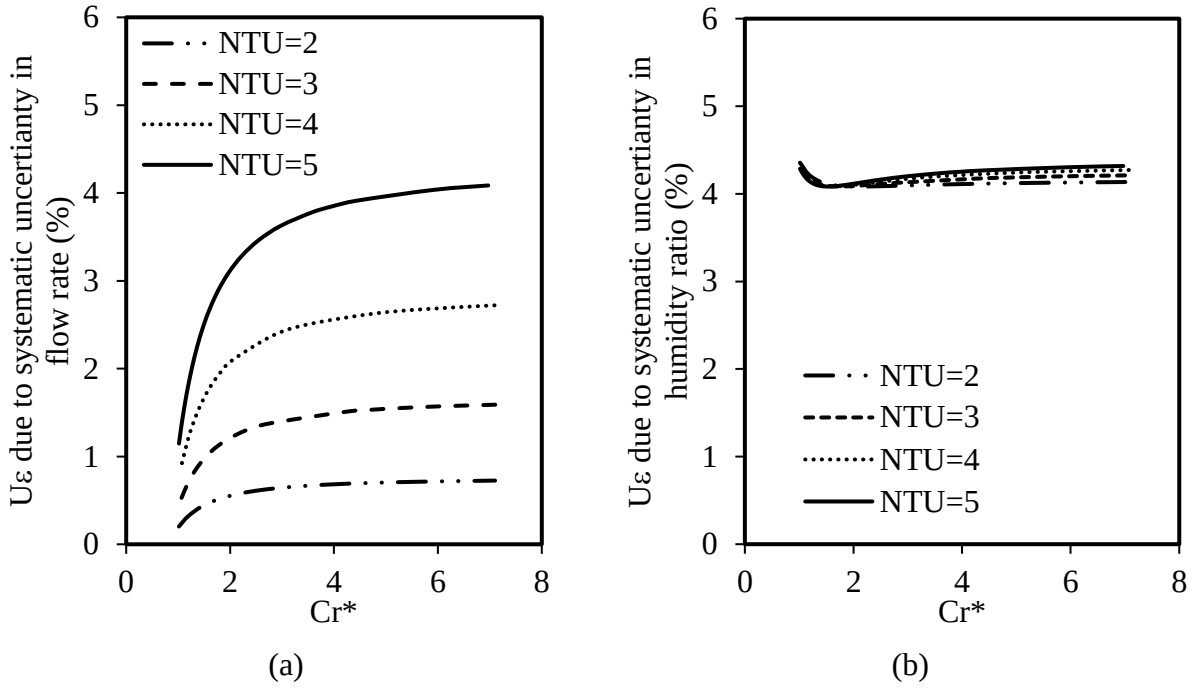

Figure 4.22. Uncertainty in latent effectiveness due to systematic uncertainty in (a) flow rate and (b) humidity measurements.

The total uncertainty in latent effectiveness is determined by combining the systematic uncertainty from the humidity ratio and mass flow rates. Figure 4.23 shows the uncertainty in latent effectiveness as a function of NTU_o and Cr*. The uncertainty in latent effectiveness increases from 4-6% depending on the test conditions. The higher uncertainty in high NTU_o conditions is due to the increase in uncertainty in mass flow rate, as explained previously. It should also be noted that the analysis is carried out using the correlation which is valid for $3 \leq Cr^* \leq 10$ and $2 \leq NTU_o \leq 10$ conditions. Therefore, the uncertainty values for lower Cr* conditions shown in Figure 4.23 need not be accurate. From the uncertainty analysis, it is confirmed that the small-scale testing

method explained in this study can generate test results within the uncertainty limits specified by ASHRAE standard 84.

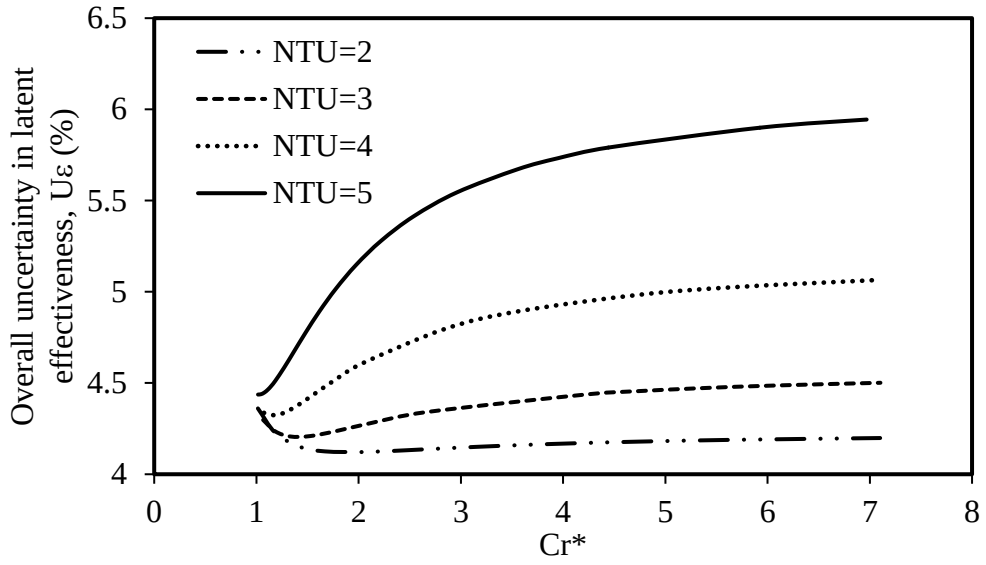

Figure 4.23. Overall Uncertainty in latent effectiveness for different NTU_o and Cr^* conditions.

4.7.3 Non-isothermal test results ($\Delta T \neq 0$, $\Delta W \neq 0$)

In practical operating conditions, the humidity and temperature of inlet airstreams are different; hence, both heat and moisture transfer occur simultaneously between the exchanger and airstreams, and the outlet humidity and temperature vary with time. The response of the humidity sensor is very slow during these non-isothermal conditions (τ = 35 s – 140 s) [45] and is expected to cause significant errors in effectiveness estimation. The following sections discuss the results from combined heat and moisture transfer experiments.

4.7.3.1 FBR humidity and temperature profiles

Figure 4.24 shows the inlet and outlet humidity and temperature profiles during the combined heat and moisture transfer tests (i.e., non-isothermal conditions; $\Delta T \neq 0$, $\Delta W \neq 0$). Unlike isothermal

tests, significant differences are observed in the outlet humidity measured by the duct and exchanger sensors during the entire operating period. As explained in Section 4.7.2.2, the slow response of the humidity sensors during non-isothermal conditions causes this discrepancy in humidity sensor measurements. However, the outlet temperatures measured by the duct and exchanger sensors are in good agreement within the experimental uncertainty after the initial 3 s (Figure 4.24 (b)). The initial deviation in sensor measurements (0-3s) is due to the response of thermocouples as reported in Section 2.10.2 of Chapter 2.

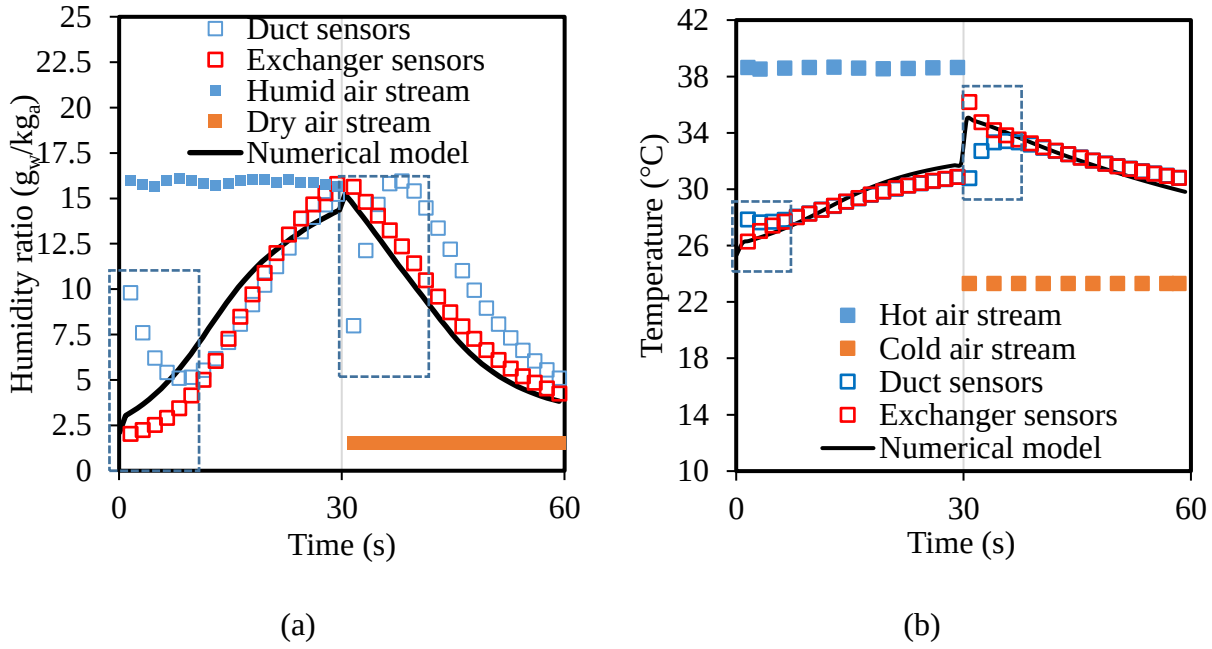

(a) (b)

Figure 4.24. Comparison of (a) humidity and (b) temperature profiles of airstreams obtained from duct and exchanger sensors with the model (face velocity: 1.15 m/s, period: 30 s).

4.7.3.2 Determination of sensible, latent, and total effectiveness

Sensible and latent effectiveness: The sensible effectiveness of the FBR is determined from the time-averaged temperatures measured at the FBR inlets and outlets using Eq. (4.1). The temperature measurements during the initial transient region (Figure 4.4 (b)) are corrected by taking the average of the exchanger and duct sensor measurements (average effectiveness). It

should be noted that the back-fit method explained in Chapter 2 of this thesis cannot be used in this case as the temperature profiles are not linear since these experiments include the heat of sorption from the desiccants. The sensible effectiveness test results agree with the numerical model and the correlation within ±5% as shown in Figure 4.25 (a), which confirms the validity of this method. The literature correlation is modified in combined heat and moisture transfer experiments in the same way as explained in Section 4.7.2.4 and presented as the correlation in Figure 4.25 and Figure 4.26.

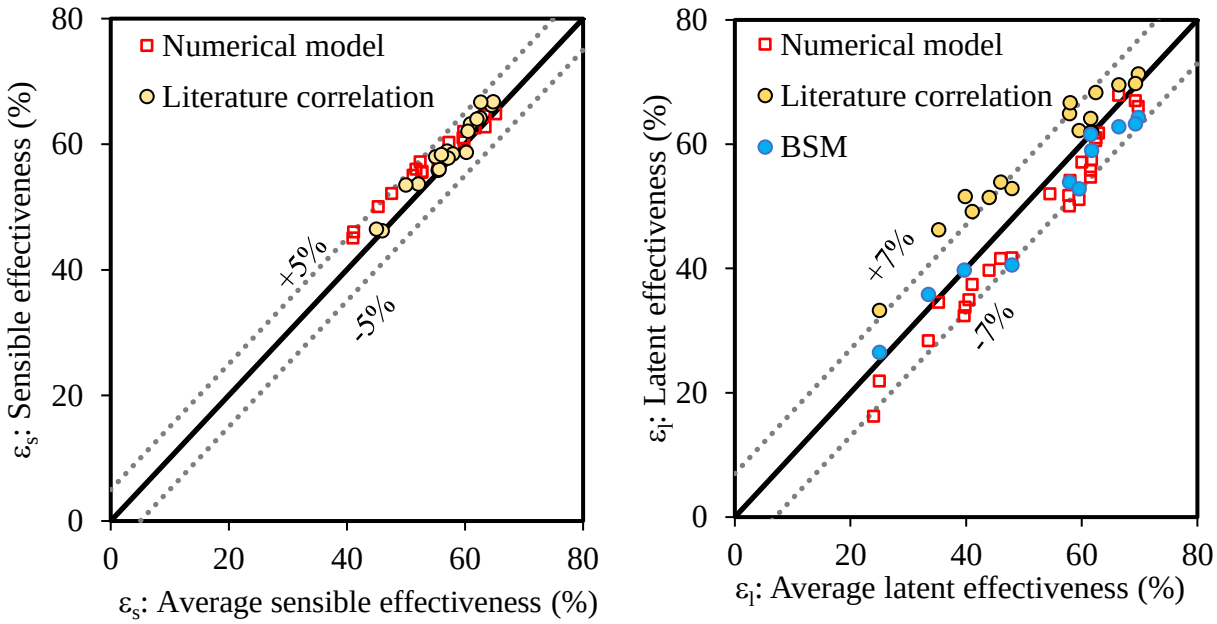

Figure 4.25. Comparison of average (a) sensible and (b) latent effectiveness with numerical model and literature correlation.

The latent effectiveness is determined using the sensor measurements and BSM. Nearly 10% difference is observed in latent effectiveness determined from the exchanger and duct sensor measurements, and this difference is due to the slow response of the humidity sensors. Similar to the sensible effectiveness estimation, the humidity measurements during the initial transient region (as highlighted in Figure 4.24 (a)) are corrected by taking the average of the exchanger and duct

sensor measurements (average effectiveness). The average latent effectiveness agrees with the numerical model and BSM within ±7% uncertainty as shown in Figure 4.25 (b). The deviation in sensible and latent effectiveness between the numerical model and correlation, from the experiments could be due to the heat loss/heat gain to the surroundings during the tests and the assumption of equal distribution of phase change energy to the airstream and the exchanger plates in the model.

Total effectiveness: Simonson and Besant have shown that the sensible, latent, and total effectiveness are functions of the operating conditions [30]. By knowing the values of operating condition factor (H*), sensible and latent effectiveness, the total effectiveness can be determined using Eq. (4.13) [30], [104].

In this chapter, the total effectiveness is evaluated using three different approaches as follows:

1. Average total effectiveness: The temperature and humidity measurements of the exchanger and duct sensors are used to determine the enthalpy values at the exchanger inlets and outlets; subsequently, the total effectiveness is calculated using Eq. (4.1). The total effectiveness of the FBR is determined by averaging the exchanger sensors' ($\varepsilon_{t\text{-Ex. sensors}}$) and duct sensors' ($\varepsilon_{t\text{-Duct sensors}}$) total effectiveness values.

2. Based on BSM latent effectiveness and average sensible effectiveness: The total effectiveness is estimated using the sensible effectiveness, latent effectiveness, and H* using Eq. (4.11), where the sensible and latent effectiveness are based on temperature measurements and the BSM, respectively.

3. Based on average sensible and latent effectiveness: The total effectiveness is estimated using the average sensible effectiveness, latent effectiveness, and H* using Eq. (4.11),

where the sensible and latent effectiveness are based on temperature and humidity sensor measurements (from the exchanger and duct sensors), respectively.

Figure 4.26 shows the comparison of total effectiveness obtained from the various test methods with the numerical model and correlation. The uncertainty in total effectiveness varies from ±6% to ±8%, depending on the test conditions. The total effectiveness from all the experimental approaches agrees with the numerical model and literature correlation within the experimental uncertainty limits. As already explained, the errors in the transient humidity measurements cause errors in the enthalpy calculation, resulting in incorrect estimation of total effectiveness. The assumptions in the numerical model such as 1-D direction of heat and moisture, instantaneous diffusion of water vapor in desiccants, equal distribution of phase change energy to the airstream and the exchanger, heat /moisture interaction between the airstreams and the exchanger, and the humidity sensor transients could be the reasons for the discrepancies in test results with the numerical model. The average sensible, latent, and total effectiveness determined from the sensor measurements for different tests, including detailed test conditions, are reported in Table E.1 of Appendix E. More detailed investigations are required to determine the validity of this method for a wide range of non-isothermal operating conditions.

In some FBR experimental designs, the duct sensor measurements are not possible because of the exchanger configuration (or arrangement), e.g., the single-core configuration presented in ASHRAE standard 84 [12]; it is recommended to use the BSM for humidity measurements (isothermal tests) and temperature sensor measurements for sensible effectiveness (non-isothermal tests) in those cases.

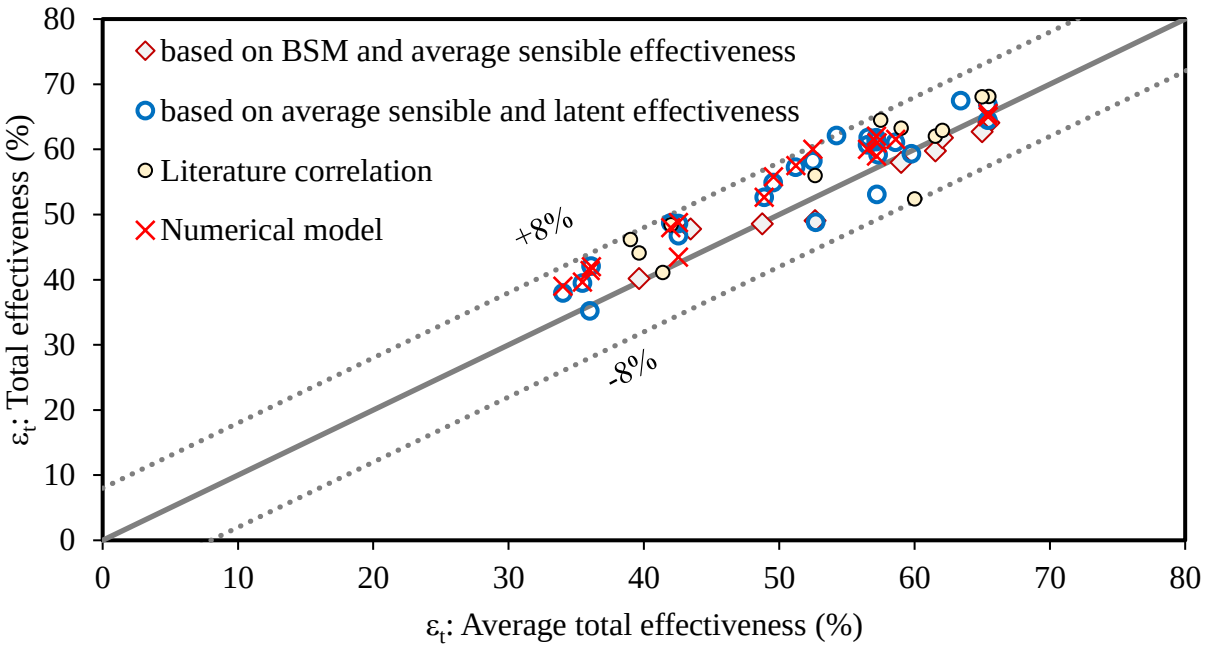

Figure 4.26. Comparison of average total effectiveness obtained from experiments with those from the numerical model and literature correlation.

The test methods for performance evaluation of FBRs for isothermal and non-isothermal test conditions with the typical uncertainty values are presented in Table 4.7. The suitable methods must be selected based on the test conditions and the availability of instrumentation. The advantages of sensor measurements are that they provide instantaneous outlet humidity measurements and eliminate the cost of instrumentation related to the BSM. More studies will need to be conducted in the future to understand the transient behavior of humidity sensors in non-isothermal conditions.

Table 4.7. Summary of test methods and uncertainties for the performance evaluation of FBRs.

Test conditions	Performance parameter	Test method	Uncertainty
Isothermal ($\Delta T = 0$, $\Delta W \neq 0$)	ε_l	1. Average (ε- Ex. sensors and ε- Duct sensors) 2. Bag sampling method	≤6%
Non-Isothermal ($\Delta T \neq 0$, $\Delta W \neq 0$)	ε_s	1. Average (ε- Ex. sensors and ε- Duct sensors)	≤5%
	ε_l	1. Average (ε- Ex. sensors and ε- Duct sensors) 2. Bag sampling method	≤7%
	ε_t	1. Average (ε- Ex. sensors and ε- Duct sensors) 2. $\varepsilon_t = \frac{\varepsilon_s + \varepsilon_l H^*}{1 + H^*}$ 3. where ε_s is the average sensible effectiveness, ε_l is the latent effectiveness from sensor measurements or the BSM and H* is the operating condition factor.	≤8%

4.8 CONCLUSIONS

This chapter introduced new experimental methods for evaluating the sensible, latent, and total effectiveness of desiccant-coated fixed-bed regenerators (FBRs). The experiments were performed on a small-scale, silica gel-coated exchanger that was moved periodically between two air streams. The bag sampling method (BSM) for humidity measurements suggested by ASHRAE 84 and CSA C 439-18 standards was also implemented and verified. The test methods for evaluating sensible, latent, and total effectiveness are summarized below.

Sensible effectiveness: The effectiveness values obtained from temperature sensors that move with the exchanger (exchanger sensors) and are stationary in the ducts (duct sensors) are averaged to determine the sensible effectiveness. The linear backfit method presented in Chapter 2 could

not be applied for desiccant-coated FBRs since the temperature profiles are no longer linear during coupled heat and moisture transfer due to the heat of adsorption and desorption. The advantage of averaging exchanger and duct sensors is that it does not require any curve fitting or extrapolation. However, all test facilities may not have both duct and exchanger sensors, which limits the application of this method.

Latent effectiveness: The latent effectiveness is determined at isothermal and non-isothermal test conditions by two different approaches: (i) the bag sampling method (BSM) and (ii) the average effectiveness obtained from temperature and humidity sensors that move with the exchanger (exchanger sensors) and that are stationary in the ducts (duct sensors). The main advantage of the BSM is that it eliminates errors due to sensor transients; however, BSM is cumbersome and also requires additional instrumentation such as vacuum pumps and sampling bags. Similar to the sensible effectiveness estimation, the average of the humidity and temperature sensor measurements from the exchanger and duct sensors is used to determine the latent effectiveness.

Total effectiveness: The total effectiveness is evaluated using (i) the relationship between sensible effectiveness, latent effectiveness, and operating condition factor (H*) (it should be noted that the latent effectiveness could be obtained from either the BSM or sensor measurements), and (ii) the average of effectiveness values obtained from the temperature and humidity sensors that move with the exchanger (exchanger sensors) and that are stationary in the ducts (duct sensors).

The proposed methods are verified using a numerical model and a correlation from the literature, and the test data agree with the model and correlation within the experimental uncertainties. The slight discrepancies in outlet humidity profiles and effectiveness could be mainly due to the slow response of the humidity sensors. The agreement between experimental data and the numerical

model confirms that the proposed small-scale testing is a promising method to evaluate the latent effectiveness of FBRs.

CHAPTER 5

SUMMARY, CONCLUSIONS, CONTRIBUTIONS AND FUTURE WORK

The main goal of this thesis is to develop test methods to determine the performance of fixed-bed regenerators (FBRs). The key hypothesis is that the effectiveness of full-scale FBRs can be predicted by testing a similar small-scale FBR (or exchanger). The hypothesis is verified by developing an experimental facility and testing small-scale exchangers in the facility. The major benefits of the proposed methodology compared to conventional full-scale testing are (i) low cost per test, (ii) full-scale exchangers are not needed (important during product development) and (iii) better control on operating conditions due to the reduced size of the ducting and low volume of conditioned air flow. This chapter presents a summary of the research, conclusions, major contributions of the thesis, and potential areas of future research for FBRs.

5.1 SUMMARY AND CONCLUSIONS

The selection of suitable methods for performance testing of FBRs depends on the configuration of the test facility and the availability of instrumentation. In this thesis, a test facility was designed in such a way that the transient temperature and humidity outlet measurements can be captured using sensors located at the outlet of the exchanger, which move with the exchanger as it moves between airstreams (exchanger sensors or Ex. sensors) and sensors located in the stationary ducts (duct sensors). In addition, the bag sampling method (BSM) was implemented to determine the average humidity at the FBR outlets. The test methods developed in the thesis to evaluate the sensible, latent, and total effectiveness of FBRs (presented in Chapters 2, 3, and 4) are based on the temperature and humidity sensor measurements and the BSM. The proposed test methods are summarized in Tables 5.1 and 5.2.

Table 5.1. Summary of test methods and uncertainties for the performance evaluation of FBRs (heat transfer only).

Test conditions	Performance parameter	Test method	Uncertainty range	Chapter
Non-Isothermal ($\Delta T \neq 0$, $\Delta W = 0$)	ε_s	1. Linear backfit method: Effectiveness evaluation based on corrected Ex. sensors or Duct sensors. 2. Average (ε- Ex. sensors and ε- Duct sensors)	≤5%	2,3

Table 5.2. Summary of test methods and uncertainties for the performance evaluation of desiccant coated FBRs (heat and moisture transfer).

Test conditions	Performance parameter	Test method	Uncertainty range	Chapter
Isothermal ($\Delta T = 0$, $\Delta W \neq 0$)	ε_l	1. Average (ε- Ex. sensors and ε- Duct sensors) 2. Bag sampling method	≤6%	4
Non-Isothermal ($\Delta T \neq 0$, $\Delta W \neq 0$)	ε_s	1. Average (ε- Ex. sensors and ε- Duct sensors)	≤5%	
	ε_l	1. Average (ε- Ex. sensors and ε- Duct sensors) 2. Bag sampling method	≤7%	
	ε_t	1. Average (ε- Ex. sensors and ε- Duct sensors) 2. $\varepsilon_t = \frac{\varepsilon_s + \varepsilon_l H^*}{1 + H^*}$ where ε_s is the average sensible effectiveness, ε_l is the latent effectiveness from sensor measurements or the BSM and H* is the operating condition factor.	≤8%	

It should be noted that in some experimental designs, it might not be possible to have duct sensors due to the arrangement of exchangers (e.g., test facility presented in refs [12], [43]) and in those cases, it is recommended to use the linear backfit method for sensible effectiveness and the BSM for latent effectiveness determination.

5.1.1 Objective 1: To develop an experimental facility to evaluate the sensible effectiveness of fixed-bed regenerators

In this thesis, an experimental facility is developed to test the heat transfer performance of FBRs. The design, principle of operation, and mass and energy balances of the facility were presented in detail in Chapter 2. A small-scale parallel-plate exchanger was used to verify the test facility and methods. Unlike other energy exchangers, FBRs are transient devices, i.e., the outlet air temperature varies with time in a periodic pattern. The errors in outlet temperature measurements due to the slow response of temperature sensors were identified and corrected. The sensible effectiveness results obtained from the facility were verified with a validated numerical model and two literature correlations. In addition, the instantaneous outlet temperature profiles were also compared with the numerical model. Major conclusions and outcomes related to the first objective are given below:

- The developed test facility can be successfully used to determine the sensible effectiveness of FBRs. The facility and instrumentation can operate at 0.8-2.5 m/s face velocity, –30 °C to +45 °C supply air temperature and can accommodate exchangers up to 1 m long.
- It is found that the slow response (time constant) of sensors results in errors in the measured FBR outlet temperature profile, and the error depends on the location of the sensors (duct or exchanger sensors). The errors due to the slow response of the sensors are corrected by backfitting a linear curve to the outlet temperature profile.
- The uncertainty in sensible effectiveness will be less than 5% when the backfitting method is applied for the operating conditions likely to be used in small-scale testing.

Objective 2: To develop testing methodologies to predict the sensible effectiveness and uncertainty of full-scale FBRs from small-scale tests.

Since the physical dimensions and operating conditions of full-scale and small-scale FBRs are different, test results from small-scale FBRs cannot be directly applied to predict the performance of full-scale FBRs. In Chapter 3, two new methods were developed to extrapolate the small-scale test results to full-scale FBRs. The uncertainty in sensible effectiveness from the two methods was also presented. The major conclusions related to this objective are:

- Two methods, namely direct and predictive methods, were developed and the results were verified with the field test results.
- In the direct method, the sensible effectiveness of full-scale FBRs was determined by testing similar small-scale FBRs. To apply this method, the number of transfer units, heat capacity rate ratio, and longitudinal heat conduction parameters (NTU_o, Cr* and λ) of the small-scale FBRs should be the same as that of the full-scale FBRs. Uncertainty analysis showed that the sensible effectiveness of full-scale FBRs could be predicted with ±3.5% for typical FBR operating conditions.
- The predictive method requires a numerical model in addition to small-scale test data. The average heat transfer coefficient from the small-scale tests is used in a numerical model to extrapolate the results to full-scale FBRs. This method requires only an optimum number of tests, and the sensible effectiveness can be predicted within ±5% uncertainty for typical FBR operating conditions.
- The proposed test methods are used to determine the effects of corrugation angle and corrugation depth on the heat transfer coefficient and sensible effectiveness of FBRs. The

heat transfer coefficient and effectiveness increase as the corrugation angle increases from (β-29) ° to β°. Increasing the corrugation angle from β° to (β+21) ° did not cause any significant changes. The heat transfer coefficient and effectiveness also increase with corrugation depth.

Objective 3: To develop testing methodologies to predict the latent and total effectiveness and uncertainty of desiccant-coated full-scale FBRs from small-scale tests.

Test methods were developed to evaluate the effectiveness of FBRs for the cases of (i) isothermal ($\Delta T = 0$, $\Delta W \neq 0$) and (ii) non-isothermal operating conditions ($\Delta T \neq 0$, $\Delta W \neq 0$). A silica gel coated small-scale exchanger was used to develop the test methods. The errors in FBR outlet measurements due to the slow response of the humidity sensors were identified, and their impact on sensible, latent, and total effectiveness was investigated. The key conclusions from this objective are summarized as follows:

For isothermal tests:

- The latent effectiveness of FBRs can be predicted accurately using the average measurements of the humidity and temperature sensors located at two different locations (duct sensors and exchanger sensors).
- The bag sampling method (BSM) for humidity measurements should be implemented to determine the average outlet humidity ratio and the latent effectiveness. Suitable instrumentation and sampling procedures are recommended for BSM analysis.
- The latent effectiveness results obtained from the experiments were verified with a validated numerical model and the results were in good agreement within the experimental uncertainty limits.

- The uncertainty in latent effectiveness determined from the sensor measurements and the BSM will be ±7% for the operating conditions likely to be used in small-scale testing.

For non-isothermal tests:

- The sensible, latent, and total effectiveness were successfully determined at non-isothermal test conditions using sensor measurements and the BSM.
- The response of the humidity sensors was significantly affected by the simultaneous change in temperature and humidity and resulted in 15-20% errors in latent and total effectiveness estimation. The errors are reduced by averaging the measurements of the humidity and temperature sensors placed at two different locations (duct sensors and exchanger sensors)
- Methods were developed to determine the total effectiveness of FBRs based on the temperature and humidity sensor measurements, and the BSM. The test results agreed with the numerical data within the experimental uncertainty limits.

5.2 CONTRIBUTIONS

The outcomes of this research contribute towards the development and testing of FBRs for HVAC applications. The main contributions of this Ph.D. thesis are listed below:

- A novel experimental facility was developed to test FBR temperature and humidity outlet conditions. The facility was used to test exchangers with different plate configurations and geometries and can also be used in the future to test potential desiccant materials for FBR applications.

- New test methods were developed to determine the (i) sensible effectiveness, (ii) latent effectiveness, and (iii) total effectiveness of FBRs for HVAC applications.
- The uncertainty bounds of sensible and latent effectiveness for typical small-scale test conditions were quantified, and the methods met the uncertainty requirements specified in ASHRAE standard 84.
- This thesis verified the use of transient humidity averaging technique called the bag sampling method (BSM) introduced by ASHRAE 84 and CSA C 439-18 test standards for FBR experiments.

5.3 FUTURE WORK

Performance evaluation of FBRs at extreme climatic conditions

- The test methods developed in this thesis can be implemented or modified to study the effect of extreme operating conditions such as condensation and frosting on the performance of FBRs. This will provide an insight into the effects of condensation or frost formation on the thermo-hydraulic performance of FBRs and the mechanism of frost formation in FBRs. It is also expected that the exchanger geometry and period will have an impact on the performance of the FBRs at extreme climatic conditions, which is not known in the literature.
- It is suggested to study the durability of FBR desiccant coatings and the impact of contaminants on their moisture transfer capacity. This can be done through accelerated testing, which will provide insight on (i) the factors having a significant contribution to the aging of desiccants, (ii) the effect of thermal cycling on sorption capacity, and (iii) durability of desiccant coating in FBRs.

Development of new desiccant materials

Since desiccant materials are required in FBRs for moisture transfer, it is important to develop desiccants having high moisture adsorption capacity. On the other hand, no studies have identified the best desiccant candidates for FBRs. Suitable candidates can be identified through material selection, characterization, and testing in the small-scale facility. A systematic test protocol can be developed for choosing potential desiccants for HVAC applications.

CFD modelling and flow channel optimization of FBRs

The flow structures and patterns inside the FBR channels strongly influence its thermo-hydraulic performance. Commercial CFD packages can be used to model the flow channels of the FBR with various shapes (e.g., triangular, sinusoidal, and hexagonal) to understand the flow behavior. Subsequently, it is recommended to identify the optimum configuration suitable for FBRs for the highest heat and moisture transfer. It is also recommended to investigate the effects of flow-maldistribution on the thermo-hydraulic performance of FBRs. The flow maldistribution could be due to the variations in channel geometry as well as the configuration of the damper directing air flow in and out of the exchangers."

Small-scale testing of desiccant beds

Desiccant-coated exchangers are widely employed in many applications for humidification and dehumidification processes. It is recommended to extend this work to study the performance of FBRs at desiccant drying test conditions using the facility and the method presented in this thesis. Additional modifications are required in the facility to incorporate the regeneration process in desiccant beds. Test methods and potential desiccant candidates will be the possible outcomes of this research.

Small-scale testing of FBRs for pressure drop evaluation

Pressure drop is also an important performance indicator for FBRs as they are made of corrugated plates. It is recommended to study the influence of scaling on pressure drop measurements. The initial tests found that the sidewalls/boundaries of small-scale FBRs significantly influence the pressure drop measurements. The impact of scaling on pressure drop measurements can be evaluated by testing FBRs with different frontal areas.

REFERENCES

[1] L. Pérez-Lombard, J. Ortiz, and C. Pout, “A review on buildings energy consumption information,” *Energy and Buildings*, vol. 40, no. 3, pp. 394–398, 2008.

[2] Natural Resources Canada, “Energy Efficiency Trends in Canada - 1990 to 2013,” 2016. https://www.nrcan.gc.ca/maps-tools-and-publications/publications/energy-publications/10734 (accessed Jun. 06, 2020).

[3] Natural Resources Canada, “Energy Use Data Handbook 1990–2015.” http://oee.nrcan.gc.ca (accessed Jun. 06, 2020).

[4] S. K. Brown, M. R. Sim, M. J. Abramson, and C. N. Gray, “Concentrations of volatile organic compounds in indoor air - a review,” *Indoor Air*, vol. 4, no. 2, pp. 123–134, 1994.

[5] D. Enescu, “A review of thermal comfort models and indicators for indoor environments,” *Renewable and Sustainable Energy Reviews*, vol. 79, pp. 1353–1379, 2017.

[6] Natural Resources Canada, “Codes Canada,” 2011. https://nrc.canada.ca/en/certifications-evaluations-standards/codes-canada (accessed Apr. 10, 2020).

[7] L. Aditya *et al.*, “A review on insulation materials for energy conservation in buildings,” *Renewable and Sustainable Energy Reviews*, vol. 73, pp. 1352–1365, 2017.

[8] S. Kubba, *Handbook of Green Building Design and Construction*. Amsterdam: Elsevier, 2012.

[9] M. T. Fauchoux, C. J. Simonson, and D. A. Torvi, “The effect of energy recovery on perceived air quality, energy consumption, and the economics of an office building,” *ASHRAE Transactions*, vol. 113, no. 2, pp. 436–448, 2007.

[10] ASHRAE, *ASHRAE Handbook-HVAC Systems and Equipment*. Atlanta, 2020.

[11] Tempeff North America, “The Dual Core Difference.”

https://www.tempeffnorthamerica.com/dual-core-heat-recovery/ (accessed May 17, 2020).

[12] ANSI/ASHRAE, *Standard 84, Method of testing air-to-air heat/energy exchangers*. Atlanta, 2020.

[13] Canadian Standards Association, *Standard laboratory methods of test for rating the performance of heat/energy-recovery ventilators*. Canada: CSA Group, 2018.

[14] R. K. Shah and D. P. Sekulic, *Fundamentals of Heat Exchanger Design*, no. 3. Hoboken: John Wiley & Sons, Inc., 2003.

[15] D. G. Moghaddam, P. Lepoudre, G. Ge, R. W. Besant, and C. J. Simonson, "Small-scale single-panel liquid-to-air membrane energy exchanger (LAMEE) test facility development, commissioning and evaluating the steady-state performance," *Energy and Buildings*, vol. 66, pp. 424–436, 2013.

[16] F. Fathieh, "A Novel transient testing method for heat/energy wheel components," PhD thesis, University of Saskatchewan, Saskatoon, 2016.

[17] Air-Conditioning Heating and Refrigeration Institute, *Performance Rating of Air-to-Air Exchangers for Energy Recovery Ventilation Equipment*. Arlington, United States: AHRI, 2013.

[18] O. O. Abe, Y. H. Wang, C. J. Simonson, R. W. Besant, and W. Shang, "Transient temperature measurements and characteristics for temperature sensors and energy wheels," *ASHRAE Transactions*, vol. 112, no. 2, pp. 76–89, 2006.

[19] O. O. Abe, R. W. Besant, C. J. Simonson, and W. Shang, "Relationship between energy wheel speed and effectiveness and its transient response, part I: Mathematical development of the characteristic time constants and their relationship with effectiveness," *ASHRAE Transactions*, vol. 112, no. 2, pp. 89–102, 2006.

[20] Y. Wang, R. W. Besant, C. J. Simonson, and W. Shang, “Application of humidity sensors and an interactive device,” *Sensors and Actuators, B: Chemical*, vol. 115, no. 1, pp. 93–101, 2006.

[21] W. Shang, “Evaluation of enegry wheel performance,” PhD thesis, University of Saskatchewan, Saskatoon, 2002.

[22] M. Shakouri, E. N. Krishnan, A. H. Karoyo, L. Dehabadi, L. D. Wilson, and C. J. Simonson, “Water vapor adsorption–desorption behavior of surfactant-coated starch particles for commercial energy wheels,” *ACS Omega*, vol. 4, no. 11, pp. 14378–14389, 2019.

[23] M. Shakouri, E. N. Krishnan, L. Dehabadi, A. H. Karoyo, C. J. Simonson, and L. D. Wilson, “Vapor adsorption transient test facility for dehumidification and desorption studies,” *International Journal of Technology*, vol. 9, no. 6, pp. 1092–1102, 2018.

[24] W. O. Alabi, A. H. Karoyo, E. N. Krishnan, L. Dehabadi, L. D. Wilson, and C. J. Simonson, “Comparison of the moisture adsorption properties of starch particles and flax fiber coatings for energy wheel applications,” *ACS Omega*, vol. 5, no. 16, pp. 9529–9539, 2020.

[25] W. M. Kays and A. L. London, *Compact heat exchangers*, Third edit. New York: McGraw-Hill, Inc, 1984.

[26] O. Büyükalaca and T. Yilmaz, “Influence of rotational speed on effectiveness of rotary-type heat exchanger,” *Heat and Mass Transfer*, vol. 38, no. 4–5, pp. 441–447, 2002.

[27] P. Worsøe-Schmidt, “Effect of fresh air purging on the efficiency of energy recovery from exhaust air in rotary regenerators,” *International Journal of Refrigeration*, vol. 14, no. 4, pp. 233–239, 1991.

[28] R.K. Shah and A. L. London, *Advances in Heat Transfer, Laminar Flow Forced Convection in Ducts*. New York: Academic Press, 1978.

[29] C. J. Simonson, C. Dustin, and R. W. Besant, "Determining the performance of energy wheels: Part 1 - Experimental and numerical methods," *ASHRAE Transactions*, vol. 105, no. 1, pp. 174–187, 1999.

[30] C. J. Simonson and R. W. Besant, "Energy wheel effectiveness: part II—correlations," *International Journal of Heat and Mass Transfer*, vol. 42, no. 12, pp. 2171–2185, 1999.

[31] A. A. Rabah, "Experimental investigation on the performance of a lithium chloride wheel," *Thermal Science*, vol. 16, no. 4, pp. 1137–1150, 2012.

[32] J. W. Jeong and S. A. Mumma, "Practical thermal performance correlations for molecular sieve and silica gel loaded enthalpy wheels," *Applied Thermal Engineering*, vol. 25, no. 5–6, pp. 719–740, 2005.

[33] D. Ghadiri Moghaddam, R. W. Besant, and C. J. Simonson, "A methodology for scaling a small-scale energy exchanger performance results to a full-scale energy exchanger," *International Journal of Heat and Mass Transfer*, vol. 82, pp. 555–567, 2015.

[34] M. A. El-Rifai and N. E. Taymour, "Temperature transients in fixed bed heat regenerators," *Chemical Engineering Science*, vol. 29, no. 8, pp. 1687–1694, 1974.

[35] V. Vakiloroaya, B. Samali, A. Fakhar, and K. Pishghadam, "A review of different strategies for HVAC energy saving," *Energy Conversion and Management*, vol. 77, pp. 738–754, 2014.

[36] R. Kheiri, H. Ghaebi, M. Ebadollahi, and H. Rostamzadeh, "Thermodynamic modeling and performance analysis of four new integrated organic Rankine cycles (A comparative study)," *Applied Thermal Engineering*, vol. 122, pp. 103–117, 2017.

[37] H. R. B. Ajdari and S. M. Sadrameli, “Theoretical and experimental studies of a thermal regenerator for heat recovery in aluminum meltingfurnaces,” in *Light Metals 2015*, M. Hyland, Ed. Cham: Springer International Publishing, 2015, pp. 439–443.

[38] A. V. Koshel’nik, T. N. Pugachova, O. V. Kruglyakova, V. G. Pavlova, and O. V. Dolobovskaya, “Increasing the operating efficiency of regenerative heat-exchangers of glass furnaces,” *Glass and Ceramics (English translation of Steklo i Keramika)*, vol. 76, no. 1–2, pp. 68–71, 2019.

[39] C. C. Chang, J. De Liang, and S. L. Chen, “Performance investigation of regenerative total heat exchanger with periodic flow,” *Applied Thermal Engineering*, vol. 130, pp. 1319–1327, 2018.

[40] C. H. Chen, P. C. Huang, T. H. Yang, Y. C. Chiang, and S. L. Chen, “Polymer/alumina composite desiccant combined with periodic total heat exchangers for air-conditioning systems,” *International Journal of Refrigeration*, vol. 67, pp. 10–21, 2016.

[41] Y. A. Aristov, I. V Mezentsev, and V. A. Mukhin, “A new approach to heat and moisture regeneration in the ventilation system of rooms. I. Laboratory prototype of the regenerator,” *Journal of Engineering Physics and Thermophysics*, vol. 79, no. 3, pp. 569–576, 2006.

[42] M. Justo Alonso, P. Liu, H. M. Mathisen, G. Ge, and C. Simonson, “Review of heat/energy recovery exchangers for use in ZEBs in cold climate countries,” *Building and Environment*, vol. 84. pp. 228–237, 2015.

[43] M. I. Nizovtsev, V. Y. Borodulin, V. N. Letushko, and A. A. Zakharov, “Analysis of the efficiency of air-to-air heat exchanger with a periodic change in the flow direction,” *Applied Thermal Engineering*, vol. 93, pp. 113–121, 2016.

[44] M. Czachorski, J. Wurm, W. M. Worek, J. Mierke, and P. Brillhart, “Dynamic testing of desiccant matrices and computerized evaluation of performance maps,” *ASHRAE Transactions*, vol. 103, no. 1, pp. 833–840, 1997.

[45] Y. Wang, C. J. Simonson, R. W. Besant, and W. Shang, “Transient humidity measurements: Part I - Sensor calibration and characteristics,” *IEEE Transactions on Instrumentation and Measurement*, vol. 56, no. 3, pp. 1074–1079, 2007.

[46] F. Fathieh, R. W. Besant, R. W. Evitts, and C. J. Simonson, “Determination of air-to-air heat wheel sensible effectiveness using temperature step change data,” *International Journal of Heat and Mass Transfer*, vol. 87, pp. 312–326, 2015.

[47] F. Fathieh, R. W. Besant, R. W. Evitts, and C. J. Simonson, “Effects of Heat Loss/Gain on the Transient Testing of Heat Wheels,” *Journal of Thermal Science and Engineering Applications*, vol. 8, no. 3, p. 031003, 2016.

[48] ISO, *International Standard: ISO 5167-1 Measurement of fluid flow by means of pressure differential devices inserted in circular cross-section conduits running full--Part 1: General principles and requirements*. Geneva, 2003.

[49] ISO, *International Standard: ISO 5167-2, Measurement of fluid flow by means of pressure differential devices inserted in circular cross section conduits running full--part 2 Orifice plates*. Geneva, 2003.

[50] Hart Scientific, *9105 / 9107 Dry-well Calibrator User’s Guide*. Utah, 2002.

[51] Thunder Scientific® Corporation, “Model 1200 Mini ‘Two-Pressure’ Humidity Generator.” https://www.thunderscientific.com/humidity_equipment/model_1200.html (accessed Oct. 21, 2019).

[52] G. Druck, “DPI 605 Precision Portable Pressure Calibrator.”

http://www.testequipmentdepot.com/druck/pressure-calibrators/dpi605.htm (accessed Oct. 21, 2019).

[53] ASME/ANSI, *Performance Test Code 19.1 Test Uncertainty: Instruments and Apparatus*. New York, 1998.

[54] R.S. Figliola; D.E. Beasley, *Theory and Design for Mechanical Measurements*, 4th ed. New Jersey: John Wiley & Sons Inc, Hoboken, 2006.

[55] H. Ramin, E. Krishnan, and C. J. Simonson, "Fixed bed regenerators for HVAC applications," in *Proceedings of the 27th CANCAM*, Aug. 2019, pp. 1–6.

[56] C. Simonson and R. Besant, "Heat and moisture transfer in desiccant coated rotary energy exchangers: Part I. Numerical model," *HVAC&R Research*, vol. 3, no. 4, pp. 325–350, 1997.

[57] C. J. Simonson and R. W. Besant, "Energy wheel effectiveness: Part I-development of dimensionless groups," *International Journal of Heat and Mass Transfer*, vol. 42, no. 12, pp. 2161–2170, 1999.

[58] H. K. Versteeg and W. Malalasekera, *An Introduction to Computational Fluid Dynamics : the Finite Volume Method*, 6th ed. Harlow, England: Pearson Education Ltd., 2007.

[59] T. Yilmaz and O. Büyükalaca, "Design of regenerative heat exchangers," *Heat Transfer Engineering*, vol. 24, no. 4, pp. 32–38, 2003.

[60] G. D. Bahnke and C. P. Howard, "The effect of longitudinal heat conduction on periodic-flow heat exchanger performance," *Journal of Engineering for Gas Turbines and Power*, vol. 86, no. 2, pp. 105–117, 1964.

[61] H. Ramin, E. N. Krishnan, A. Gurubalan, W. O. Alabi, and C. J. Simonson, "A transient numerical model for sensible fixed-bed regenerator in HVAC applications," *International*

Journal of Heat and Mass Transfer, vol. 177, p. 121550, 2021.

[62] V. S. Gullapalli and B. Sundén, "CFD simulation of heat transfer and pressure drop in compact brazed plate heat exchangers," *Heat Transfer Engineering*, vol. 35, no. 4, pp. 358–366, 2014.

[63] J. E. O. Brien and E. M. Sparrow, "Corrugated-duct heat transfer, pressure drop, and flow visualization," *Journal of Heat Transfer*, vol. 104, pp. 410–416, 1982.

[64] S. D. Hwang, H. H. Kim, H. H. Cho, and S. B. Chen, "Heat Transfer in Wavy Duct With Different Corrugation Angle," in *Heat Transfer, Volume 4*, 2002, vol. 4, pp. 63–70.

[65] Dovic and Svaic, "Influence of chevron plates geometry on performances of plate heat exchangers," *Tehnicki Vjesnik*, vol. 14, pp. 37–45, 2007.

[66] A. D. Ochoa, J. W. Baughn, and A. R. Byerley, "A new technique for dynamic heat transfer measurements and flow visualization using liquid crystal thermography," *International Journal of Heat and Fluid Flow*, vol. 26, no. 2, pp. 264–275, 2005.

[67] S. Harikrishnan and S. Tiwari, "Effect of skewness on flow and heat transfer characteristics of a wavy channel," *International Journal of Heat and Mass Transfer*, vol. 120, pp. 956–969, 2018.

[68] L. Z. Zhang, "Turbulent three-dimensional air flow and heat transfer in a cross-corrugated triangular duct," *Journal of Heat Transfer*, vol. 127, no. 10, pp. 1151–1158, 2005.

[69] L. C. Yang, Y. Asako, Y. Yamaguchi, and M. Faghri, "Numerical prediction of transitional characteristics of flow and heat transfer in a corrugated duct," *Journal of Heat Transfer*, vol. 119, no. 1, pp. 62–69, 1997.

[70] J. Fernández-Seara, F. J. Uhía, J. Sieres, and A. Campo, "A general review of the Wilson plot method and its modifications to determine convection coefficients in heat exchange

devices," *Applied Thermal Engineering*, vol. 27, no. 17–18, pp. 2745–2757, 2007.

[71] M. De Paepe and A. Janssens, "Thermo-hydraulic design of earth-air heat exchangers," *Energy and Buildings*, vol. 35, pp. 389–397, 2003.

[72] M. De Paepe, A. Willems, and A. Zenner, "Experimental determination of the heat transfer coefficient of a plate-fin heat exchanger," *Heat Transfer Engineering*, vol. 26, no. 7, pp. 29–35, 2005.

[73] H. Huisseune, S. De Schampheleire, B. Ameel, and M. De Paepe, "Comparison of metal foam heat exchangers to a finned heat exchanger for low Reynolds number applications," *International Journal of Heat and Mass Transfer*, vol. 89, pp. 1–9, 2015.

[74] E. N. Krishnan, H. Ramin, M. Shakouri, L. D. Wilson, and C. J. Simonson, "Development of a small-scale test facility for effectiveness evaluation of fixed-bed regenerators," *Applied Thermal Engineering*, vol. 174, p. 115263, 2020.

[75] H. Ramin, E. N. Krishnan, W. O. Alabi, and C. J. Simonson, "Temperature measurement correction for the determination of the effectiveness of fixed-Bed regenerators (FBRs) for HVAC applications," *ASHRAE Transactions*, vol. 126, pp. 366–374, 2020.

[76] H. Martin, "A theoretical approach to predict the performance of chevron-type plate heat exchangers," *Chemical Engineering and Processing: Process Intensification*, vol. 35, no. 4, pp. 301–310, 1996.

[77] W. W. Focke, J. Zachariades, and I. Olivier, "The effect of the corrugation inclination angle on the thermohydraulic performance of plate heat exchangers," *International Journal of Heat and Mass Transfer*, vol. 28, no. 8, pp. 1469–1479, 1985.

[78] A. Muley and R. M. Manglik, "Experimental study of turbulent flow heat transfer and pressure drop in a plate heat exchanger with chevron plates," *Journal of Heat Transfer*,

vol. 121, no. 1, pp. 110–117, 1999.

[79] G. Gasier and V. Kottke, “Effects of wavelength and inclination angle on the homogeneity of local heat transfer coefficients in plate heat exchangers,” in *Proceedings of 11th International Heat Transfer Conference,* 1998, pp. 203–208.

[80] J. Stasiek, M. W. Collins, M. Ciofalo, and P. E. Chew, “Investigation of flow and heat transfer in corrugated passages - I. Experimental results,” *International Journal of Heat and Mass Transfer*, vol. 39, no. 1, pp. 149–164, 1996.

[81] B. Sundén, “Flow and Heat Transfer Mechanisms in Plate-and-Frame Heat Exchangers,” in *Heat Transfer Enhancement of Heat Exchangers*, Dordrecht: Springer Netherlands, 1999, pp. 185–206.

[82] K. Sarraf, S. Launay, and L. Tadrist, “Complex 3D-flow analysis and corrugation angle effect in plate heat exchangers,” *International Journal of Thermal Sciences,* vol. 94, pp. 126–138, 2015.

[83] C. Zimmerer, P. Gschwind, G. Gaiser, and V. Kottke, “Comparison of heat and mass transfer in different heat exchanger geometries with corrugated walls,” *Experimental Thermal and Fluid Science*, vol. 26, no. 2–4, pp. 269–273, 2002.

[84] D. Dović, B. Palm, and S. Švaić, “Generalized correlations for predicting heat transfer and pressure drop in plate heat exchanger channels of arbitrary geometry,” *International Journal of Heat and Mass Transfer*, vol. 52, no. 19–20, pp. 4553–4563, 2009.

[85] H. Ramin, E. N. Krishnan, and C. J. Simonson, “Effectiveness of fixed-bed regenerators for energy recovery in buildings applications,” *E3S Web of Conferences,* vol. 172, p. 09001, 2020.

[86] L. A. Sphaier and W. M. Worek, “Analysis of heat and mass transfer in porous sorbents

used in rotary regenerators," *International Journal of Heat and Mass Transfer*, vol. 47, no. 14–16, pp. 3415–3430, 2004.

[87] A. Jedlikowski, P. Kanaś, and S. Anisimov, "Heat and mass transfer inside the rotary heat exchanger operating under high speed rotor conditions," *International Journal of Heat and Mass Transfer*, vol. 152, p. 119558, 2020.

[88] F. Fathieh *et al.*, "Determination of air-to-air energy wheels latent effectiveness using humidity step test data," *International Journal of Heat and Mass Transfer*, vol. 103, pp. 501–515, 2016.

[89] F. Fathieh, M. Nezakat, R. W. Evitts, and C. J. Simonson, "Effects of physical and sorption properties of desiccant coating on performance of energy wheels," *Journal of Heat Transfer*, vol. 139, no. 6, p. 062601, 2017.

[90] M. A. Hossain, A. H. Karoyo, L. Dehabadi, F. Fathieh, C. J. Simonson, and L. D. Wilson, "Starch particles, energy harvesting, and the 'goldilocks Effect,'" *ACS Omega*, vol. 3, no. 4, pp. 3796–3803, 2018.

[91] E. Cerrah, C. McCague, and M. Bahrami, "Sorbent based enthalpy recovery ventilator," *Energy and Buildings*, vol. 211, p. 109755, 2020.

[92] W. A. Belding, M. P. F. Delmast, and W. D. Holemans, "Desiccant aging and its effects on desiccant cooling system performance," *Applied Thermal Engineering*, vol. 16, no. 5, pp. 447–459, 1996.

[93] E. Cerrah and M. Bahrami, "Disc-type sorbent enthalpy recovery ventilator (SERV)," in *The Second Pacific Rim Thermal Engineering Conference*, 2019, pp. 1–5.

[94] E. N. Krishnan, H. Ramin, A. Gurubalan, W. O. Alabi, and C. J. Simonson, "Methodologies for Predicting the Effectiveness of Full-Scale Fixed-Bed Regenerators

From Small-Scale Test Data," *Journal of Thermal Science and Engineering Applications*, vol. 13, no. 5, p. 051019, 2021.

[95] Y. Wang, C. J. Simonson, R. W. Besant, and W. Shang, "Transient humidity measurements: Part II - Determination of the characteristics of an interactive device," *IEEE Transactions on Instrumentation and Measurement*, vol. 56, no. 3, pp. 1080–1086, 2007.

[96] R. Haul, "Adsorption, surface area and porosity," *Berichte der Bunsengesellschaft für physikalische Chemie*, vol. 86, no. 10, pp. 957–957, 1982.

[97] SKC air sampling solutions, "SKC Tedlar bags," 2019. https://www.skcinc.com/catalog/index.php (accessed Jul. 21, 2019).

[98] Millipore Sigma, "Gas Sampling Bags & Samplers," 2020. https://www.sigmaaldrich.com/analytical-chromatography/air-monitoring/gas-sampling-bags.html (accessed Oct. 15, 2020).

[99] V. I. Kaplya, E. V. Kaplya, and A. A. Silaev, "Identification of the transient response of a capacitive relative humidity sensor," *Measurement Techniques*, vol. 62, no. 12, pp. 1099–1105, 2020.

[100] M. Rafati Nasr, F. Fathieh, D. Kadylak, R. Huizing, R. W. Besant, and C. J. Simonson, "Experimental methods for detecting frosting in cross-flow air-to-air energy exchangers," *Experimental Thermal and Fluid Science*, vol. 77, pp. 100–115, 2016.

[101] E. N. Krishnan, H. Ramin, and C. J. Simonson, "Performance testing of fixed-bed regenerators for HVAC applications," in *Proceedings of the 2nd Pacific Rim Thermal Engineering Conference*, 2019, pp. 1–5.

[102] H. Ramin, E. N. Krishnan, G. Annadurai, W. O. Alabi, and C. J. Simonson, "Transient

sensor errors and their impact on fixed-bed regenerator (FBR) testing standards," *Science and Technology for the Built Environment*, vol. 27, no. 5, pp. 656–678, 2021.

[103] C. J. Simonson and R. W. Besant, "Heat and moisture transfer in desiccant coated rotary energy exchangers: Part II. validation and sensitivity studies," *HVAC and R Research*, vol. 3, no. 4, pp. 351–368, 1997.

[104] C. J. Simonson and R. W. Besant, "Energy wheel effectiveness: Part I-development of dimensionless groups," *International Journal of Heat and Mass Transfer*, vol. 42, no. 12, pp. 2161–2170, 1999.

[105] I. Gherasim, M. Taws, N. Galanis, and C. T. Nguyen, "Heat transfer and fluid flow in a plate heat exchanger part I. Experimental investigation," *International Journal of Thermal Sciences*, vol. 50, no. 8, pp. 1492–1498, 2011.

[106] M. Faizal and M. R. Ahmed, "Experimental studies on a corrugated plate heat exchanger for small temperature difference applications," *Experimental Thermal and Fluid Science*, vol. 36, pp. 242–248, 2012.

[107] T. S. Khan, M. S. Khan, M. C. Chyu, and Z. H. Ayub, "Experimental investigation of single phase convective heat transfer coefficient in a corrugated plate heat exchanger for multiple plate configurations," *Applied Thermal Engineering*, vol. 30, no. 8–9, pp. 1058–1065, 2010.

[108] H. B. Luan, J. P. Kuang, Z. Cao, Z. Wu, W. Q. Tao, and B. Sundén, "CFD analysis of two types of welded plate heat exchangers," *Numerical Heat Transfer; Part A: Applications*, vol. 71, no. 3, pp. 250–269, 2017.

[109] E. N. Krishnan, H. Ramin, G. Annadurai, and C. J. Simonson, "Influence of plate geometry on sensible effectiveness of fixed-bed regenerators," in *Proceedings of the 7th*

International Conference on Fluid Flow, Heat and Mass Transfer (FFHMT'20), 2020, pp. 1–7.

[110] X. Zhu and F. Haglind, "Relationship between inclination angle and friction factor of chevron-type plate heat exchangers," *International Journal of Heat and Mass Transfer*, vol. 162, p. 120370, 2020.

[111] X. Zhu, J. H. Walther, D. Zhao, and F. Haglind, "Transition to chaos in a cross-corrugated channel at low Reynolds numbers," *Physics of Fluids*, vol. 31, no. 11, p. 114107, 2019.

[112] J. E. Hesselgreaves, R. Law, and D. A. Reay, "Surface Types and Correlations," in *Compact Heat Exchangers*, Amsterdam: Elsevier, 2017, pp. 221–274.

[113] E. M. Sparrow and L. M. Hossfeld, "Effect of rounding of protruding edges on heat transfer and pressure drop in a duct," *International Journal of Heat and Mass Transfer*, vol. 27, no. 10, pp. 1715–1723, 1984.

[114] L. Tovazhnyansky, P. Kapustenko, and V. A. Tsibulnic, "Heat transfer and hydraulic resistance in channels of plate heat exchangers," *Energetika*, vol. 9, pp. 123–125, 1980.

[115] O. P. Arsenyeva, L. Tovazhnyansky, P. Kapustenko, and G. Khavin, "The generalized correltaion for friction factor in criss cross flow channels of plate heat exchangers," *Chemical Engineering Transactions*, vol. 25, pp. 399–404, 2011.

[116] M. Ciofalo, J. Stasiek, and M. W. Collins, "Investigation corrugated of flow and heat transfer Numerical simulations," *International Journal of Heat and Mass Transfer*, vol. 39, no. 1, pp. 165–192, 1996.

[117] O. P. Arsenyeva, L. L. Tovazhnyanskyy, P. O. Kapustenko, and O. V. Demirskiy, "Heat transfer and friction factor in criss-cross flow channels of plate-and-frame heat exchangers," *Theoretical Foundations of Chemical Engineering*, vol. 46, no. 6, pp. 634–

641, 2012.

[118] B. Thonon, R. Vidil, and C. Marvillet, “Recent research and developments in plate heat exchangers,” *Journal of Enhanced Heat Transfer*, vol. 2, no. 1–2. pp. 149–155, 1995.

[119] S. Cariou and J.-M. Guillot, “Double-layer Tedlar bags: a means to limit humidity evolution of air samples and to dry humid air samples,” *Analytical and Bioanalytical Chemistry*, vol. 384, no. 2, pp. 468–474, 2005.

APPENDIX A

COPYRIGHT PERMISSIONS

The copyright permissions for the published and co-authored manuscripts documented in this thesis are presented in Appendix A. For all manuscripts that are included in a thesis, the College of Graduate and Postdoctoral Studies (CGPS) requires a written request from the publisher, *i.e.*, copyright holder (for published manuscripts) and from co-author(s) (for unpublished manuscripts). The permission for using the published and unpublished manuscripts in this thesis are documented in following subsections.

A.1 PERMISSION FOR MANUSCRIPTS USED IN CHAPTERS 2, 4, AND APPENDIX B

The manuscripts included in Chapters 2, 4 and Appendix B are published online by Elsevier. Elsevier permits authors to include the published/accepted articles in a thesis or dissertation without a written permission. The below shown statement has been directly taken from the Elsevier website.

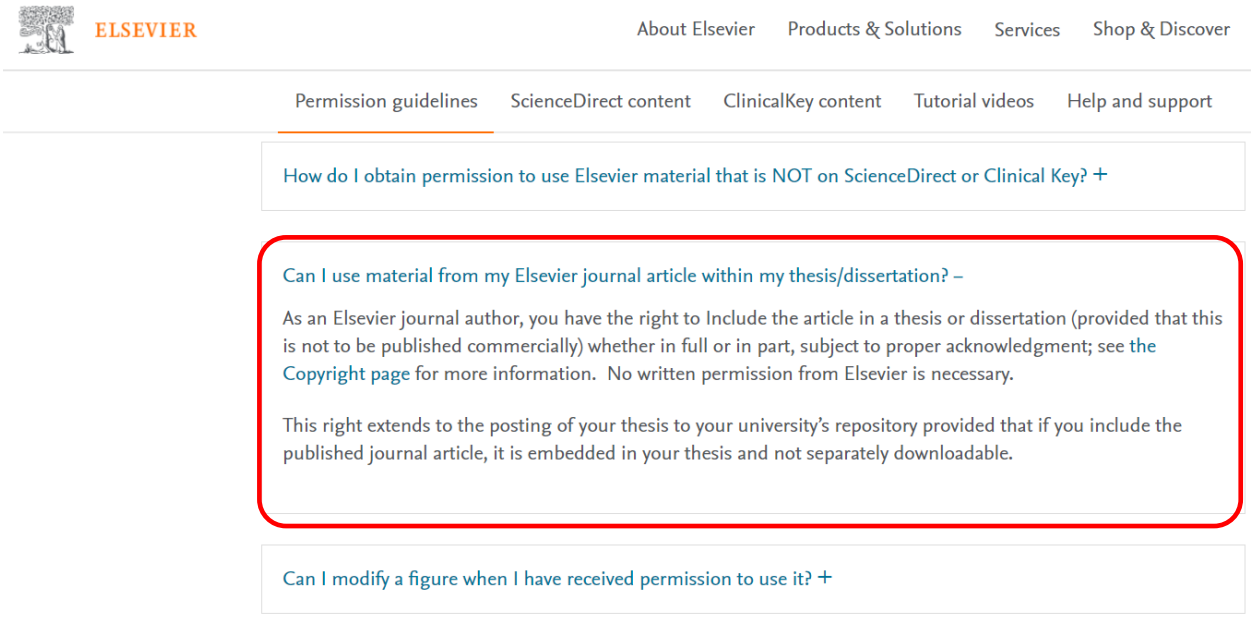

Source: https://www.elsevier.com/about/policies/copyright/permissions

(Accessed: April 18, 2021)

A.2 PERMISSION FOR MANUSCRIPT USED IN CHAPTER 3

Krishnan, Easwaran

From: Beth Darchi <DarchiB@asme.org>
Sent: Tuesday, June 22, 2021 1:07 PM
To: Krishnan, Easwaran
Subject: RE: REG: Permission request to include published manuscript in PhD Thesis

Dear Mr. Krishnan,
It is our pleasure to grant you permission to use **all or any part of** the ASME paper "Methodologies for Predicting the Effectiveness of Full-Scale Fixed-Bed Regenerators From Small-Scale Test Data," by Easwaran N. Krishnan, Hadi Ramin, A. Gurubalan, Wahab O. Alabi, Carey J. Simonson, J. Thermal Sci. Eng. Appl. Oct 2021, 13(5), cited in your letter for inclusion in a Ph. D. thesis to be published by the University of Saskatchewan, Canada.

Permission is granted for the specific use as stated herein and does not permit further use of the materials without proper authorization. Proper attribution must be made to the author(s) of the materials. **Please note**: if any or all of the figures and/or Tables are of another source, permission should be granted from that outside source or include the reference of the original source. ASME does not grant permission for outside source material that may be referenced in the ASME works.

As is customary, we request that you ensure full acknowledgment of this material, the author(s), source and ASME as original publisher.

Many thanks for your interest in ASME publications.

Sincerely,

Beth Darchi
Publishing Administrator
ASME
2 Park Avenue
New York, NY 10016-5990

APPENDIX B

THERMO-HYDRAULIC PERFORMANCE OF TRIANGULAR CROSS-CORRUGATED FLOW PASSAGES

This appendix provides the thermo-hydraulic characteristics of seven different triangular cross corrugated flow passages (or small-scale exchangers). The sensible effectiveness and heat transfer coefficient results of the corrugated exchangers reported in Chapter 3 are extended to Nusselt number and friction factor calculations. The effects of corrugation angle, corrugation depth and length of the exchanger on Nusselt number and friction factor are reported. Moreover, generalized correlations for Nusselt number and friction factor are developed based on the experimental data. The results are also compared with available results from the open literature.

The manuscript included in this appendix was published in international communications in heat and mass transfer. The first author (Mr. Easwaran N. Krishnan) conducted experiments, analyzed the data, and wrote the manuscript. Mr. Hadi Ramin (Ph.D. student) and Dr. A. Gurubalan (postdoctoral fellow) carefully reviewed the manuscript and provided the comments. Prof. Carey J. Simonson (supervisor) guided this work and critically reviewed the paper.

EXPERIMENTAL INVESTIGATION ON THERMO-HYDRAULIC PERFORMANCE OF TRIANGULAR CROSS-CORRUGATED FLOW PASSAGES

Easwaran N. Krishnan, Hadi Ramin, A. Guruabalan and Carey J. Simonson

(Published in International Communications in Heat and Mass Transfer in March 2021)

B.1 ABSTRACT

Heat exchangers made of corrugated flow passages generally have better thermo-hydraulic performance compared to parallel flow passages. The corrugation angle (β), corrugation pattern, and the ratio of depth to pitch (h_{ch}/P_{ch}) are critical geometrical parameters influencing the heat transfer and pressure drop in corrugated flow passages. This paper experimentally investigates heat transfer and pressure drop characteristics of triangular-shaped cross-corrugated flow passages for the range of $25°<\beta<75°$ and $0.13<h_{ch}/P_{ch}<0.36$. Experiments are performed using representative compact heat exchangers in a small-scale test facility. This study also reports the effects of plate geometry on heat transfer and pressure drop and provides correlations for the average Nusselt number and friction factor. A detailed comparison of test data with relevant literature is also presented. Results of this study will be useful to manufactures and designers for developing high-performance heat exchangers.

B.2 INTRODUCTION

Plate heat exchangers and fixed-bed regenerators are commonly used in many applications such as power plants, food, and chemical industries because of their compactness, high performance, and ease of cleaning [55], [80], [102], [105]. The geometry of metallic plates of these exchangers significantly influences its thermo-hydraulic performance. Studies have shown that cross corrugations in plates improve the heat transfer by 20-30% since it generates turbulence at low

Reynolds numbers [106]–[109]. Manufacturers have specifically designed corrugation patterns and stacking arrangements to achieve a high heat transfer rate with minimum pumping power.

The critical design parameters which affect the heat transfer and pressure drop in cross corrugated plates are corrugation angle (β), corrugation pattern, and the ratio of depth to pitch (h_{ch}/P_{ch}) of the plates [65], [77]–[80]. Several experimental and CFD investigations have reported the fundamental nature of the flow for sinusoidal cross-corrugated passages [62], [65], [67], [77], [79], [82], [108], [110] and shown that the fluid never attains a fully developed condition because of the sudden changes in direction due to corrugations and continuous deterioration of the boundary layer [82], [111]. In addition to mixing, the small hydraulic diameter and secondary flow formation (Görtler vortices) also contribute to the enhanced thermo-hydraulic performance of corrugated plates [112]. Focke et al. [77] and Zimmer et al. [83] categorized the flow patterns inside the cross corrugated flow channels into furrow flow or zig-zag flow, longitudinal or corkscrew flow, and mixing flow at low, intermediate, and high corrugation angles, respectively. Later, Kifah [82] showed that the Reynolds numbers or mass flow rates would also affect the transition of flow structures by CFD analysis.

Focke et al. [77] developed correlations for Coburn j factor and friction factor as a function of Reynolds number and suggested that the heat transfer is maximum at corrugation angles 72° to 80°. However, Gasier and Kottke [79] experimentally showed that optimum corrugation angles for maximum heat transfer would also depend on the ratio of corrugation depth to pitch. Later, Dovic and Svaic [65] validated the results of Gasier and Kottke [79] using flow visualization techniques. Sparrow and Hossfeld's investigation concludes that rounding of sharp edges of corrugations results in an 8-18% drop in Nusselt number [113] depending on the Reynolds number. Dovic and Svaic have proposed generalized correlations for friction factor and Nusselt number by modeling

a single unit cell of the flow channel [84]. Their predictions have a maximum of 20-25% deviation from the experimental results. Muley and Manglik [78] also investigated the performance of plate heat exchangers having 30° and 60° corrugation angles and developed correlations for Nusselt number and friction factor as functions of corrugation angle and area enlargement ratio. The heat transfer and pressure drop predictions from the reported correlations have significant discrepancies [7,11,19–21]. These could be due to insufficient test data and plate geometry information, test uncertainties, and complexities modeling the flow. Most studies on cross corrugated flow passages were focused on sinusoidal cross corrugated flow channels and their applications on plate heat exchangers. However, only a few works [114], [115] were focused on heat transfer characteristics and pressure drop in triangular cross corrugated flow channels.

The objective of this paper is to study the thermo-hydraulic performance of triangular cross corrugated flow channels. Experiments are performed on seven representative compact exchangers. The effects of corrugation angle and ratio of corrugation depth on heat transfer and pressure drop are investigated. Correlations for the average Nusselt number and friction factor are also developed based on the test data. Finally, the test results are compared with similar results from the literature.

B.3 EXPERIMENTAL METHODOLOGY

B.3.1 Test facility

A small-scale test facility is used to measure the thermo-hydraulic performance of corrugated flow passages (or exchangers), as shown in Figures B.1 and B.2. The exchanger is exposed to hot and cold airstreams alternatively with the help of a computer-controlled linear actuator unit. The duration for which the exchanger is exposed to hot and cold airstreams are called hot and cold periods, respectively. The exchanger stores heat from the airstream during the hot period and

release the stored heat in the subsequent cold period. The inlets and outlets of the cold and hot airstreams are numbered as 1, 2, 3, and 4 in Figure. B.1.

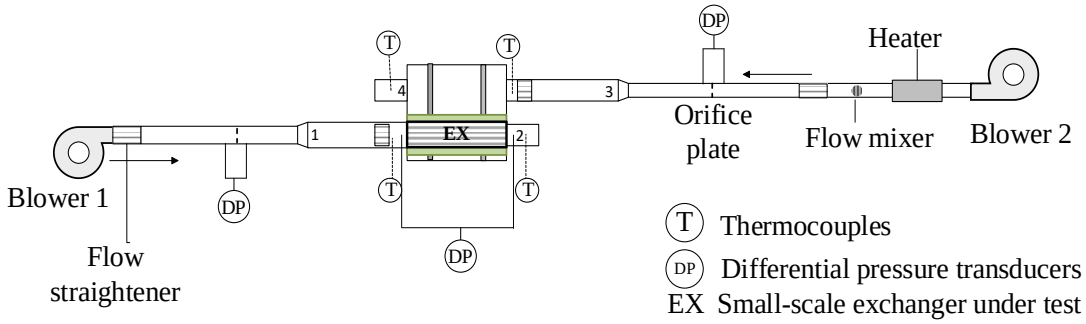

Figure B.1 Experimental facility to measure heat transfer and pressure drop in triangular cross-corrugated flow passages.

The design and development of the test facility are reported in our previous publications in detail [74], [101]. The flow rate, temperature, and pressure drop across the exchanger are measured using orifice plates, T-type thermocouples, and pressure transducers. The orifice plates are designed and installed according to the ISO standard 5167 guidelines [48]. The uncertainty in mass flow rates is evaluated from the uncertainty in pressure drop measurements across the orifice plates. The instrumentation details and their uncertainties are reported in Table B.1. The overall heat balance was evaluated in all experiments, and the maximum difference between effectiveness changes was less than 5%. This difference could be due to the heat interaction between the test section and surroundings and the measurement uncertainties.

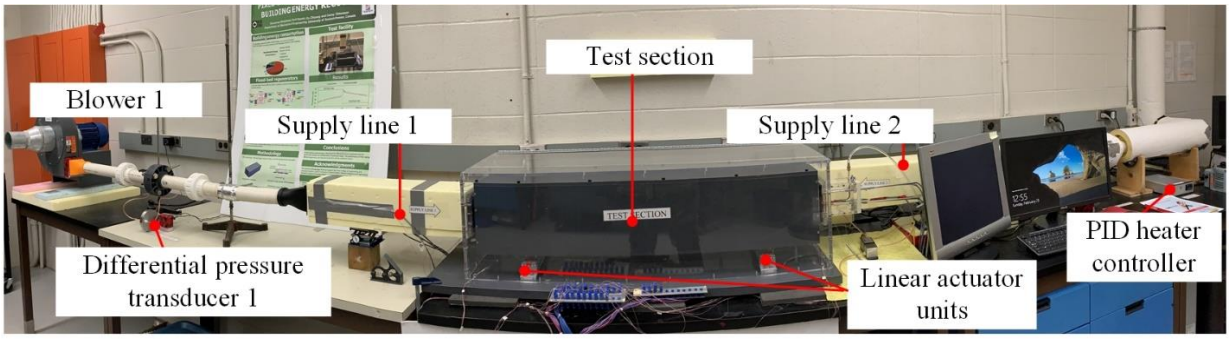

Figure B.2. Photograph of experimental facility.

Table B.1. Instruments specifications and calibration details.

Instrument	Measurement parameter	Manufacturer	Model	Calibration range	Total uncertainty
Thermocouples	Temperature	Omega	T- type	-20°C to 40°C	±0.2°C
Differential pressure transducer 1	Pressure drop across the exchanger	Validyne	DP 17	0-430 Pa	± 4 Pa
Differential pressure transducer 2	Pressure drop across the orifice plate	Validyne	DP 17	0-860 Pa	± 8 Pa

B.3.2 Exchanger geometry and performance parameters

The exchanger plates are made of corrugated aluminum sheets, and the arrangement of two consecutive plates is shown in Figure B.3. Both sides of the exchangers are covered with Styrofoam insulations, which act as sidewalls and reduce the exchanger's heat interaction with the surroundings. The corrugated plates are manufactured following industrial standards by Tempeff Inc. [11], and the deviations in corrugation depths in individual plates are less than 0.5%. Detailed geometrical specifications of plates and exchangers are provided in Table B.2. The authors could not reveal exact corrugation angles since it is patented information owned by the manufacturer

[11]. Therefore, corrugation angles are specified with reference to the standard corrugation angle (β°), i.e., exchangers can be arranged in increasing order of corrugation angles as EXs 4, 1, and 5.

Table B.2. Geometrical properties of corrugated exchangers.

	Corrugation angle (β°)	h_{ch}/P_{ch}	L/h_{ch}	Number of flow channels (n_f)	Channel hydraulic diameter (m)
EX 1	β	0.13	49	14	0.0082
EX 2	β	0.13	116	14	0.0082
EX 3	β	0.13	232	14	0.0082
EX 4	(β –29)	0.13	50	14	0.0082
EX 5	(β+21)	0.13	52	14	0.0082
EX 6	β	0.25	73	9	0.0130
EX 7	β	0.36	59	7	0.0167

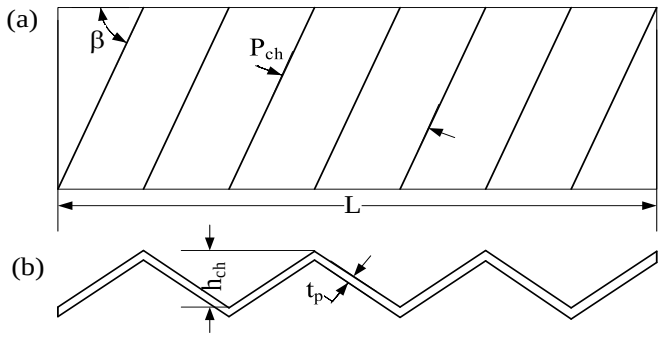

Figure B.3. Geometry of corrugated plates (a) top view (b) side view.

The corrugated plate geometry is defined by pitch (P_{ch}): distance between two adjacent peaks or valleys measured perpendicular to the direction of corrugation, depth of corrugation (h_{ch}) and the thickness of plates (t_p). It should also be noted that the length and width of the plates are reported using their dimensions measured before providing corrugations.

The hydraulic diameter (D_h) of corrugated flow channels is defined in such a way that assuming it as parallel flow channels having channel width and height are equal to the noncorrugated plate width and corrugation depth. The Reynolds number (Re) is determined using the channel velocity (V_{ch}) and hydraulic diameter and is given in Eq. (B.1).

$$\mathrm{Re}=\frac{\rho V_{ch} D_h}{\mu} \tag{B.1}$$

Where ρ and μ are the density and dynamic viscosity of the air, respectively.

Pressure drop and heat transfer coefficients are the important thermo-hydraulic performance parameters in the flow passages. The pressure drop is reported using the non-dimensional friction factor correlation [28], as presented in Eq. (B.2).

$$f=\frac{|\Delta P| D_h}{\rho L V_{ch}^2/2} \tag{B.2}$$

To determine the heat transfer coefficient, the exchangers are exposed to the hot and cold airstreams (36°C and 24°C) alternatively, and the sensible effectiveness during hot and cold exposure periods (εhot and εcold) is calculated using Eqs. (B.3) and (B.4), respectively.

$$\varepsilon_{hot}=\frac{C_1}{C_{min}}\frac{(T_1-\overline{T}_2)}{(T_1-T_3)} \tag{B.3}$$

$$\varepsilon_{cold}=\frac{C_2}{C_{min}}\frac{(\overline{T}_4-T_3)}{(T_1-T_3)} \tag{B.4}$$

where T_1 and T_3 are the temperatures of the hot and cold inlet airstreams, and $\overline{T}_2$ and $\overline{T}_4$ are the time-averaged air temperatures at the exchanger outlets, respectively. C_1 and C_2 are the heat capacity rates of hot and cold airstreams, respectively and C_{min} is the minimum of C_1 and C_2. Then the overall number of transfer units (NTU_o) is determined using the experimental

effectiveness with Kays and London correlation [14]. Subsequently, the heat transfer coefficient and Nusselt number are calculated using Eqs. (B.5) and (B.6).

$$NTU_o = \frac{1}{\min((C)_1,(C)_2)}\left[\frac{1}{1/(hA_{ht})_1 + 1/(hA_{ht})_2}\right] \quad (B.5)$$

$$Nu = \frac{hD_h}{k_f} \quad (B.6)$$

Where h and k_f are the average heat transfer coefficient and thermal conductivity of air. The detailed method of evaluating heat transfer coefficients and their uncertainty is reported in our previous publication [94].

B.3.3 Uncertainty analysis

The overall uncertainty in measurements is estimated from random (Px) and bias (Bx) uncertainties for 95% confidence interval according to ASME PTC standard 19.1 [53] as given in Eq. (B.7):

$$U = \sqrt{P_x^2 + B_x^2} \quad (B.7)$$

Random uncertainty is determined using Eq. (B.8)

$$P_x = \frac{t\,SD}{N} \quad (B.8)$$

Where t and SD are student t-factor for 95% confidence interval for a degree of freedom of (N-1) and standard deviation. Bias uncertainty includes the calibration and data reduction errors. More details on instrumentation and uncertainty analysis are reported previously [74].

The experimental uncertainties in Reynolds number, friction factor, and Nusselt number were calculated from the uncertainties in flow rate, pressure drop, and temperature measurements

according to the uncertainty propagation equation (Eq. (B.9)) and are included with respective results.

$$U_R = \left[\sum_{i=1}^{j}\left(\frac{\partial R}{\partial p_i} U_{p_i}\right)^2\right]^{0.5} \tag{B.9}$$

where U_R, U_{pi}, and $\partial R/\partial p_i$ are the total uncertainty, uncertainty in individual measurement Pi and the sensitivity coefficient of measurement Pi, respectively.

B.4 RESULTS AND DISCUSSIONS

In this section, the effects of the corrugation angle, the ratio of corrugation depth to pitch, length of the plate on average Nusselt number, and friction factor are reported. Different sets of correlations are developed for the average Nusselt number and friction factor based on the test data. It should be noted that the average Nusselt number is written as Nusselt number from here onwards.

B.4.1 Effect of corrugation angle

The effect of corrugation angle on the friction factor and Nusselt number are investigated using EXs 1, 4, and 5, and the results are compared in Figure B.4. As depicted in Table B.2, these exchangers have similar geometry but different corrugation angles. Among these three exchangers, EXs 4 and 5 have the least and highest corrugation angles. Similar to parallel plate EXs (where the flow is assumed to be laminar), the friction factor of corrugated EXs decreases with an increase in Reynolds number for the tested conditions, as shown in Figure B.4 (a). From Figure B.4 (a) and (b), the Nusselt number and friction factor are highest for EX 1(β°) compared to EX 4 (β–29°) and EX 5 (β+21°).

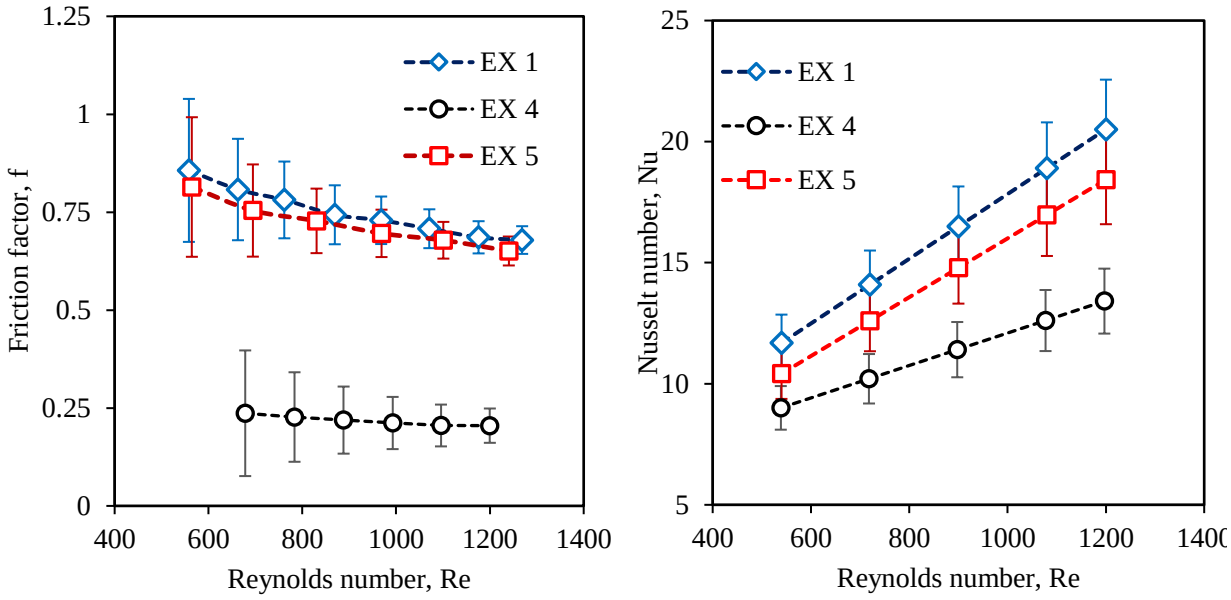

(a) (b)

Figure B.4. Effect of corrugation angle on (a) friction factor and (b) Nusselt number of triangular cross-corrugated exchangers.

The complex three-dimensional flow through the cross corrugated channels strongly influences the heat transfer process. At low corrugation angles (EX 4: β–29°), the majority of flow follows the direction of corrugations and gets reflected at the sidewalls of the exchanger, and this type of flow is known as furrow flow, which is very similar to ordinary duct flow as reported by [77], [82], [83]. At a higher corrugation angle (EX 5: β+21°), most of the fluid follows a parallel zig-zag pattern in the longitudinal direction (along the exchanger length) and is called longitudinal wavy flow [83]. It should also be noted that the presence of more contact points between the adjacent plates at high corrugation angles causes flow separation and reduces the heat transfer [79]. The high heat transfer performance at intermediate corrugation angle (EX 1: β°), is due to the mixing of longitudinal and furrow flows (mixing flow), which induces secondary swirls in the flow along the direction of corrugations [65], [83]. The findings of the present study are also in agreement with the literature conclusions, i.e., the highest Nusselt number is reported for EX 1, which has the

intermediate corrugation angle. Therefore, based on the above-tested h_{ch}/P_{ch}, ratio, the plates with intermediate corrugation angles have superior performance than plates with the highest and lowest corrugation angles. This also confirms the literature data, i.e., for sinusoidal corrugations, the optimum corrugation angles for maximum heat transfer are approximately 42°, 60°, and 70° for h_{ch}/P_{ch} of 0.14, 0.2 and, 0.27, respectively [65], [79].

B.4.2 Effect of corrugation depth to pitch (h_{ch}/P_{ch}) ratio

The effect of h_{ch}/P_{ch} ratio on friction factor and Nusselt number are studied using EXs 1, 6, and 7 and shown in Figure B.5 (a) and (b). Unlike parallel flow channels (where the flow is fully developed), the friction factor and Nusselt number of corrugated EXs increases with an increase in h_{ch}/P_{ch} ratio (or channel height). The highest and lowest Nusselt numbers are observed for EXs 7 and 1, respectively, which indicates that the heat transfer rate increases with an increase in corrugation depth (or h_{ch}/P_{ch} ratio). At higher corrugation depths (EX 7), the furrow component of the flow is significant, and as the corrugation angle increases, the longitudinal wavy flow becomes dominant [79]. Effective mixing of the furrow and longitudinal flow at higher corrugation depths and intermediate corrugation angles results in higher heat transfer rates [65], [84]. Results from the present study are also in agreement with the findings of Dovic and Svaic [65], [84], Zimmerer et al. [83], and Gasier and Kottke [79], i.e., an increase in corrugation depth at intermediate corrugation angles leads to high heat transfer.

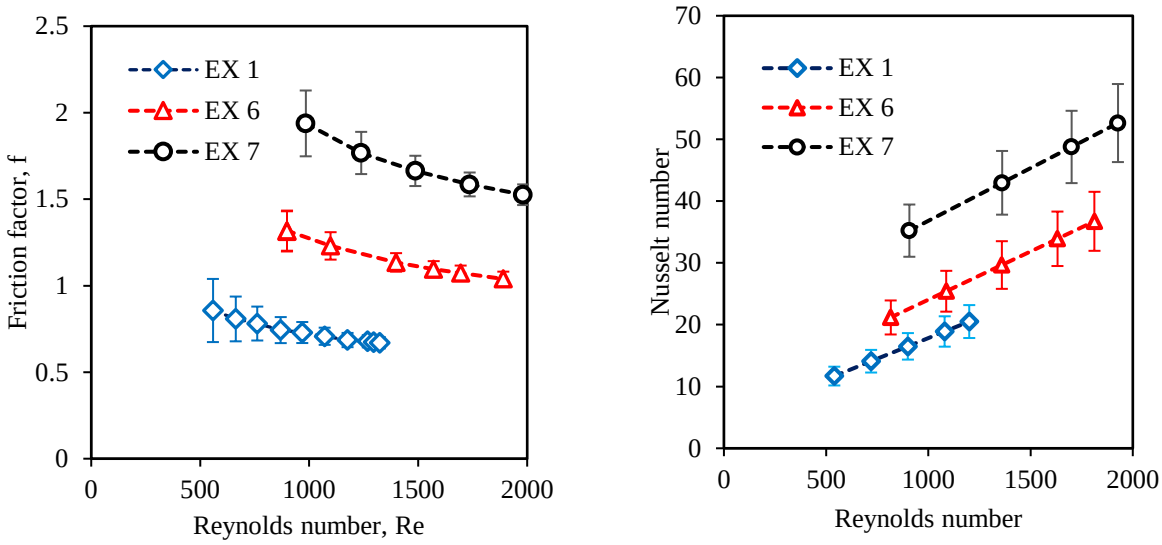

Figure B.5. Effect of corrugation depth to pitch ratio on (a) friction factor and (b) Nusselt number of triangular cross-corrugated exchangers.

B.4.3 Effect of plate length

All tested EXs have an aspect ratio of 0.05 (ratio of corrugation depth to channel width), and the tests were performed in exchangers with closed sidewalls. Unlike parallel plate EXs, the boundary layer separation and mixing of fluids due to complex flow patterns occur throughout the length of flow in corrugated EXs. The effect of the exchanger length (in the direction of airflow) on the heat transfer and friction factor has been studied using EXs 1, 2, and 3, and the results are presented in Figure B.6 (a) and (b). It is found that the friction factor of EX 1 is lower than the other two exchangers, especially at lower Reynolds numbers. However, all the results are within the experimental uncertainties. Similarly, the maximum deviation in the Nusselt number for the three tested exchangers is less than 15%. Therefore, it is reasonable to conclude that the plate length has no significant effect on the friction factor and Nusselt number.

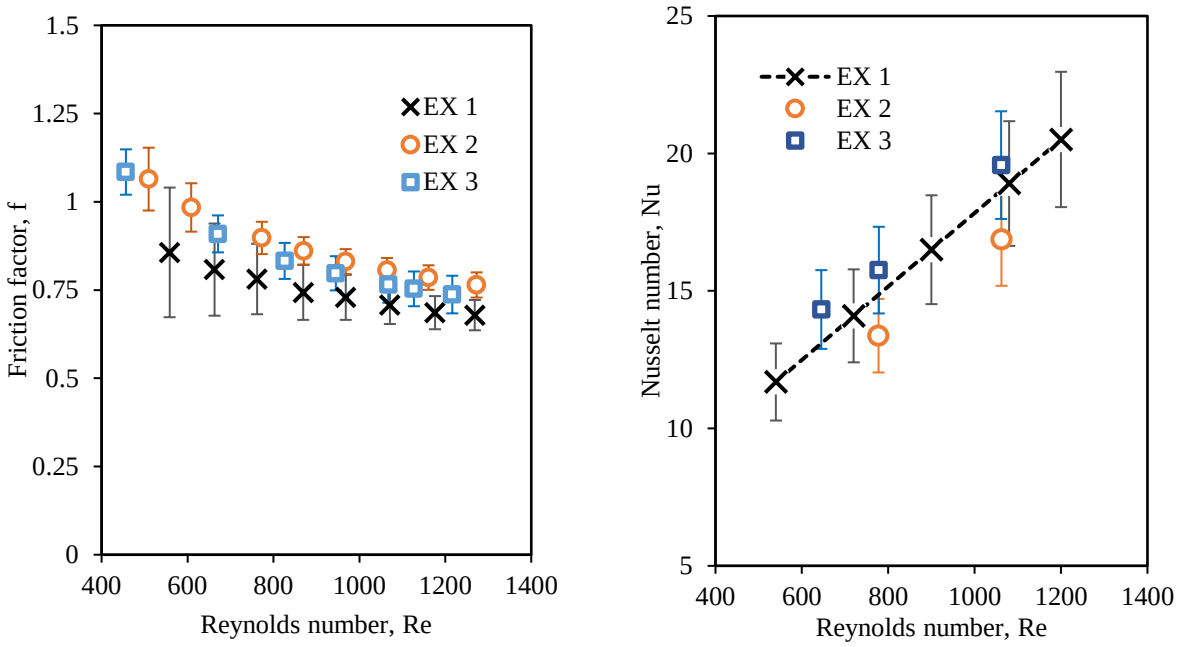

(a) (b)

Figure B.6. Effect of plate length on the (a) friction factor and (b) Nusselt number of triangular cross-corrugated exchangers.

The hydraulic diameter measurements of flow channels are critical as it affects Reynolds number, Nusselt number, and friction factor estimations. The effect of uncertainty in hydraulic diameter measurements on these results is evaluated by an uncertainty analysis using Eq. B.9. The analysis has been performed for the test conditions corresponding to the Reynolds number 640 ± 13. Figure B.7 shows the change in relative uncertainty in Reynolds number, Nusselt number, and Friction factor for 0-4% deviations in hydraulic diameter. It can be inferred that a 4% deviation in hydraulic diameter measurements increases the relative uncertainty in Reynolds number, Nusselt number, and Friction factor by 2%, 0.6%, and 0.4%, respectively. It should also be noted that the contribution of uncertainty in pressured drop (across the exchanger), flow rate, and heat transfer coefficient measurements contribute predominantly to the overall uncertainty in friction factor, Nusselt number, and Reynolds number, respectively.

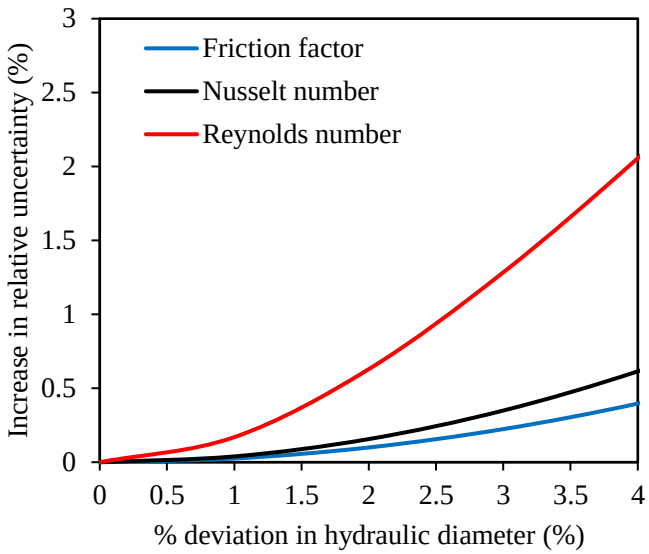

Figure B.7. Effect of % deviation in hydraulic diameter in overall uncertainty of friction factor, Nusselt number, and Reynolds number.

B.4.4 Correlations for friction factor and Nusselt number

Empirical correlations for friction factor and Nusselt number are developed for the exchangers considered for studying the effect of corrugation angle and depth as functions of Re (Eqs. (B.10) and (B.11)) using least square curve fit methods. The fitting coefficients a, b, and coefficient of determination of fit (R^2) are reported in Table B.3. The correlation results and experimental data agree with each other within ±5% for the friction factor and Nusselt number. The comparison between test data and predictions are also plotted in Figure B.8.

$$f_p = a_1 Re^{n_1} \tag{B.10}$$

$$Nu_p = a_2 Re^{n_2} Pr^{1/3} \tag{B.11}$$

Table B.3. Correlation Coefficients of friction factor and Nusselt number (Eqs. (B.10) and (B.11))

EX	Friction factor			Nusselt number		
	a_1	n_1	R^2	a_2	n_2	R^2
EX 1	4.791	0.369	0.996	0.146	0.713	0.999
EX 4	2.901	0.369	1.000	0.217	0.698	0.997
EX 5	4.707	0.278	0.993	0.851	0.561	0.999
EX 6	11.598	0.320	0.999	0.410	0.507	0.999
EX 7	16.163	0.311	0.984	0.122	0.723	0.996

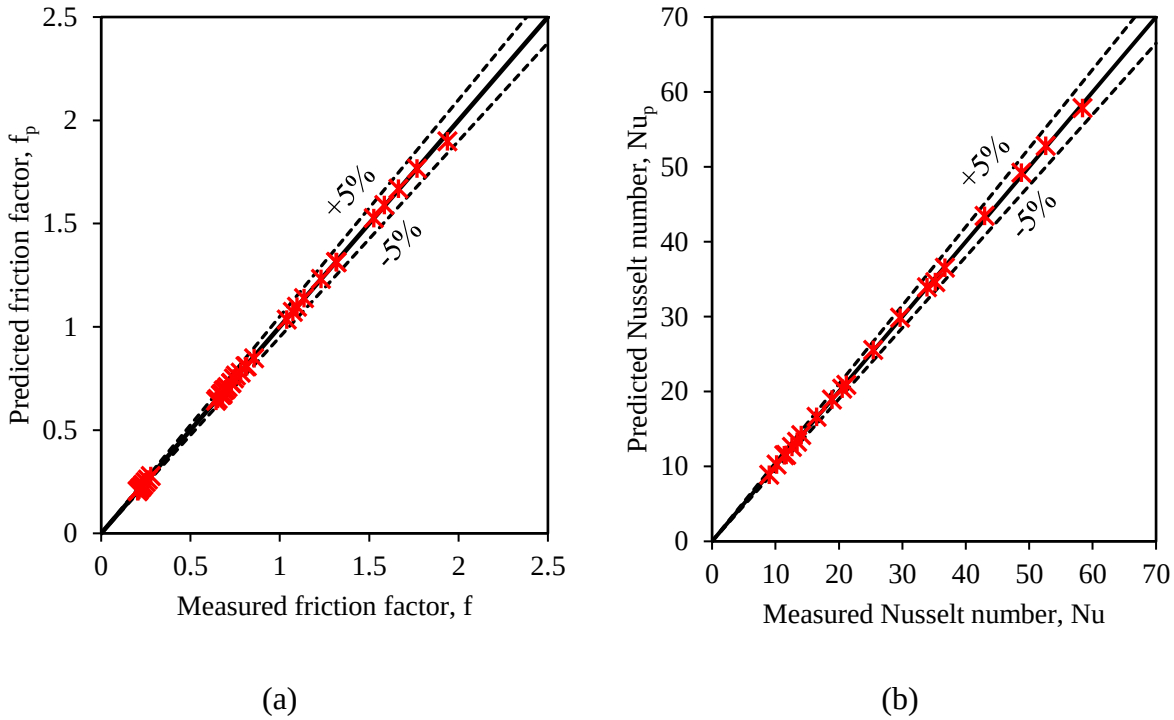

(a) (b)

Figure B.8. Comparison of experimental (a) friction factor and (b) Nusselt number with predictions (Eqs. (B.10) and (B.11)).

From the experimental data, generalized correlations for friction factor and Nusselt number are developed as functions of corrugation angle, depth to pitch ratio, and Reynolds number, and are shown in Eqs. (B.12) and (B.13). The agreement between the predicted friction factor (Figure B.9 (a)) and Nusselt number values (Figure B.9 (b)) with the test data is within ±15%, respectively,

for most of the operating conditions. The deviations between test data and measurements are highest at lower corrugation angles. However, higher Nusselt numbers are reported at high corrugation angles, and for high corrugation angles, the correlations show a good agreement with the test data (<±5%). It should be noted that both the correlations (Eqs. (B.12) and (B.13)) are developed using the test data for $0.13< h_{ch}/P_{ch} <0.36$ and $25°< \beta <75°$.

$$f_p = 44.60\left[\left(\frac{\beta\left(h_{ch}/P_{ch}\right)^2}{Re}\right)^{9.32} + \frac{1}{\left(\frac{25056\, e^{(0.05\beta)}}{Re}\right)^{16.2}}\right]^{0.066} \quad \text{(B.12)}$$

$$Nu_p = 0.205\left(0.276 Re^{3/4} f^{1/2}\right)^{5/4} Pr^{1/3} \quad \text{(B.13)}$$

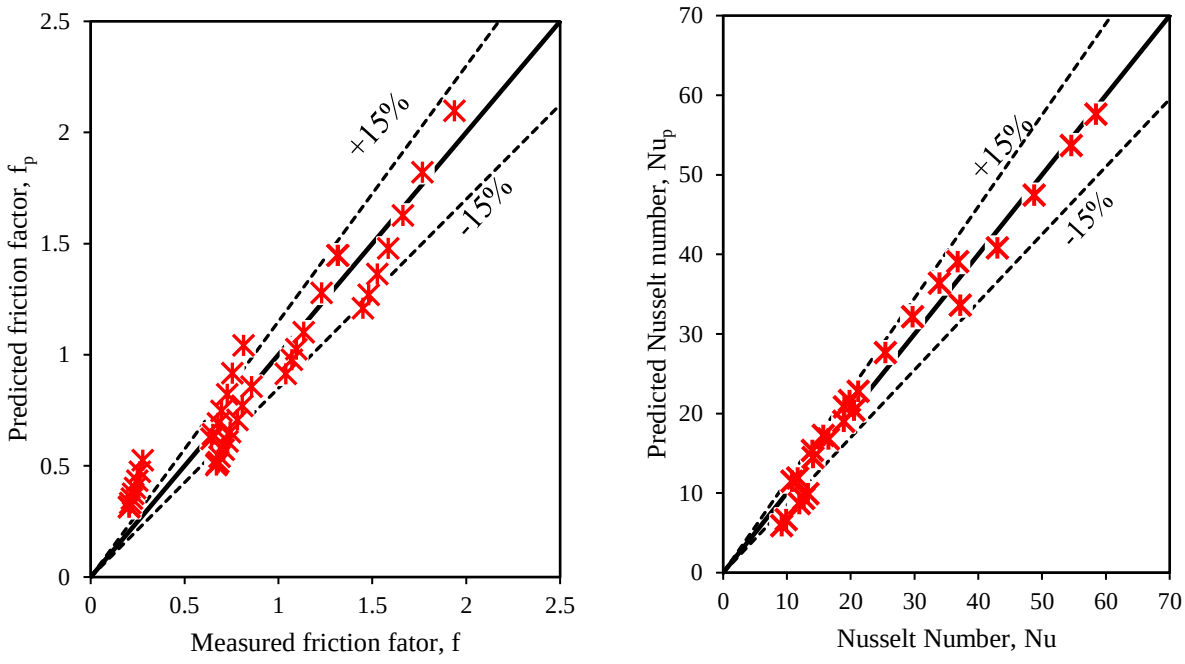

(a) (b)

Figure B.9. Comparison of experimental and predicted (a) friction factor and (b) Nusselt number.

B.4.5 Comparison of test data with literature

The published literature related to heat transfer and pressure drop in cross-corrugated passages[77]–[80], [114], [116], [117] is compared with the results of this study. Figure B.10 (a) shows the comparison of friction factor for corrugation angles ranging from 25°–80° for sinusoidal (by Gasier and Kottke [79]) and triangular configurations (test data from the present study). It should be noted that the data extracted from the literature are modified according to definition of the corrugation angle and h_{ch}/P_{ch} ratio presented in this paper. Also, the literature results (Figure B.10 (a)) correspond to the Reynolds number 2000, whereas the results of this study are obtained at Reynolds number 1250. However, from Figure B.6, it is clear the friction factor is nearly constant at high Reynolds numbers. Therefore, the qualitative comparison of test data and literature is reasonable. It can be concluded that, like sinusoidal corrugations, the Nusselt number is highest at intermediate corrugation angles compared to low and high corrugation angles. However, more number of experiments are required to determine the optimum corrugation angle for the maximum heat transfer.

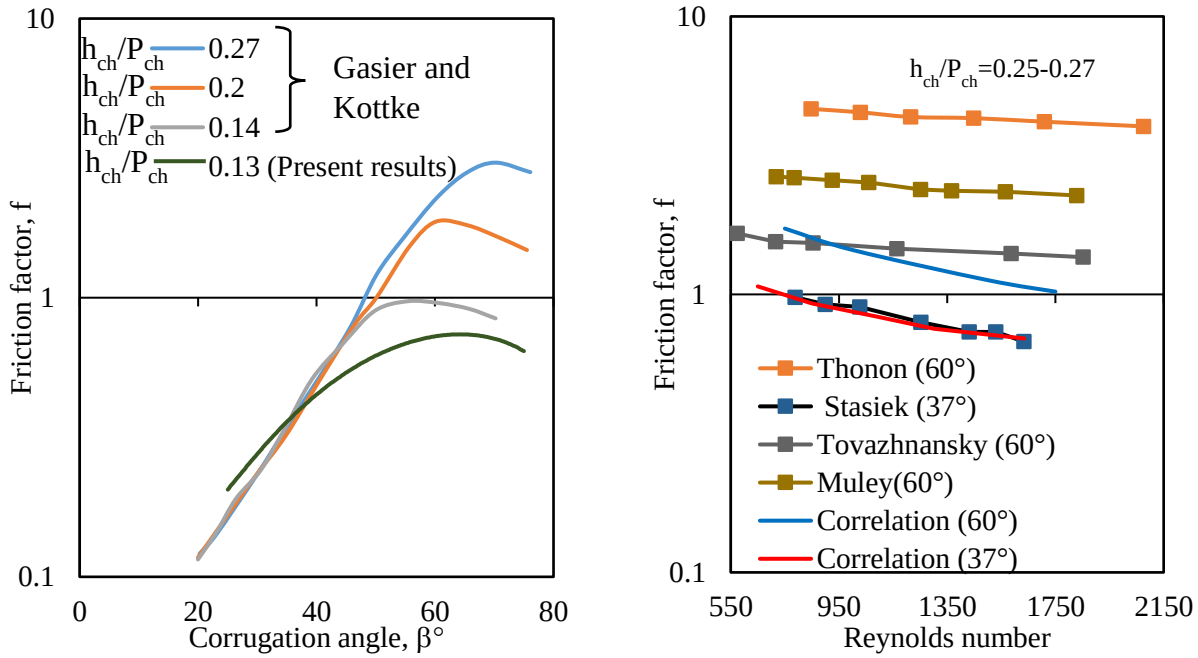

(a) (b)

Figure B.10. Comparison of friction factor results with literature data.

A comparison of the friction factor predicted from the correlation (Eq. (B.12)), and literature is presented in Figure B.10 (b). The plate configuration studied by Tovazhnyansky [114] is similar to this paper, and the correlation is in satisfactory agreement with his results compared to published data. Results of Muley [78] and Thonon [118] are based on sinusoidal configuration, and their results differ nearly by three times from each other. It is evident from the literature comparison that, similar to sinusoidal corrugation, increasing h_{ch}/P_{ch} increases the friction factor for intermediate corrugation angles. The higher friction factor values in literature data could be due to the difference in the corrugation pattern and experimental uncertainties.

The comparison of heat transfer performance is presented using $Nu/Pr^{0.4}$ with corrugation angle and Reynolds number (Nu is divided by $Pr^{0.4}$ to nullify the influence of Pr) in Figure B.11 (a) and (b). From the literature comparison (Figure B.11 (a)), the Nusselt number increases with an

increase in the corrugation angle initially. However, this trend is significant only at intermediate corrugation angles, which agrees with the findings presented in Figure B.4. The heat transfer results of Muley [78] and Stasiek [80] are compared with the correlation and presented in Figure B.11(b), and the Nusselt number results from the literature are comparable with the prediction. The quantitative comparisons are not possible because, unlike triangular corrugations, there are no sharp edges in sinusoidal corrugations. The sharp edges of triangular corrugations favor additional mixing and improved heat transfer process, resulting in high Nusselt numbers. Besides, the heat transfer area enhancement ratio (ratio of the effective area due to corrugation to the projected area) is nearly 1.15-1.3 for the sinusoidal cross-corrugated plates reported in the literature whereas it is 1.1-1.15 in the present study.

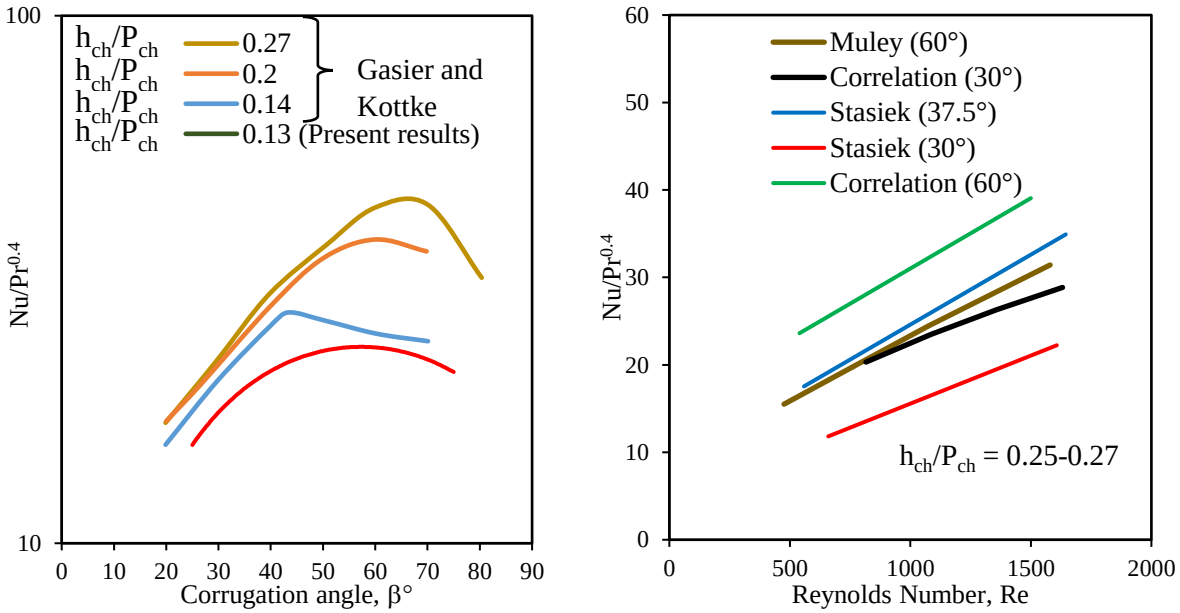

(a) (b)

Figure B.11 Comparison of Nusselt number results with literature data.

B.5 CONCLUSIONS

The thermo-hydraulic characteristics of triangular cross-corrugated flow passages are presented in this paper. The effects of corrugation angle, corrugation depth/pitch ratio, and plate length on average Nusselt number and friction factor are reported by testing representative compact heat exchangers. The average Nusselt number and friction factor (a) are highest for the exchanger having plates with intermediate corrugation angle (b) increases with an increase in the ratio of corrugation depth to pitch, and (c) is independent of the length of the plates on the direction of airflow. Finally, generalized correlations for the average Nusselt number and friction factor are developed based on the test data. The correlations and test data can be used as primary performance indicators for developing high-performance heat exchangers.

APPENDIX C

UNCERTAINTY ANALYSIS FOR HEAT TRANSFER COEFFICIENT AND SENSIBLE EFFECTIVENESS

The primary source of uncertainty in predictive method comes from uncertainty in heat transfer coefficients. The uncertainty in heat transfer coefficients arises from uncertainty in sensible effectiveness obtained from small-scale tests (i.e., due to bias error in temperature and flow rate measurements). The uncertainty in heat transfer coefficient is determined by propagating experimental uncertainties as follows:

Regenerator effectiveness: $\varepsilon = \left(\frac{NTU_o}{1+NTU_o}\right) \times ø$ (C.1)

where,

$$ø = \left(1 - \frac{1}{9Cr^{*1.93}}\right) \quad \text{(C.2)}$$

Uncertainty in NTU_o can be determined by:

$$U_{NTU_o} = \left\{\left[\frac{ø}{(ø-\varepsilon)^2} U_\varepsilon\right]^2 + \left[\frac{\varepsilon}{(ø-\varepsilon)^2} U_ø\right]^2\right\}^{0.5} \quad \text{(C.3)}$$

where U_ε and $U_ø$ are uncertainties in sensible effectiveness and correction factor can be determined as:

$$U_ø = \left(\frac{Cr^{*-2.93}}{17.37}\right) U_{Cr^*} \quad \text{(C.4)}$$

$$U_{Cr^*} = \left\{\left[\frac{Cr^*}{m_w} U_{m_w}\right]^2 + \left[\frac{Cr^*}{m_a} U_{m_a}\right]^2\right\}^{0.5} \quad \text{(C.5)}$$

$$U_\varepsilon = \left[\left(\frac{\partial\varepsilon}{\partial T_1} \cdot U_{T_1}\right)^2 + \left(\frac{\partial\varepsilon}{\partial T_2} \cdot U_{T_2}\right)^2 + \left(\frac{\partial\varepsilon}{\partial T_3} \cdot U_{T_3}\right)^2 + \left(\frac{\partial\varepsilon}{\partial m_1} \cdot U_{m_1}\right)^2 + \left(\frac{\partial\varepsilon}{\partial Tm_{min}} \cdot U_{m_{min}}\right)^2\right]^{0.5} \quad \text{(C.6)}$$

where each sensitivity term can be determined from Eq. (C.1)

$$\frac{\partial \varepsilon}{\partial T_1} = \frac{m_1}{m_{min}} \frac{(T_2 - T_3)}{(T_1 - T_3)^2} \tag{C.7}$$

$$\frac{\partial \varepsilon}{\partial T_2} = \frac{\varepsilon}{(T_1 - T_2)} \tag{C.8}$$

$$\frac{\partial \varepsilon}{\partial T_3} = \frac{\varepsilon}{(T_1 - T_3)} \tag{C.9}$$

$$\frac{\partial \varepsilon}{\partial m_1} = \frac{\varepsilon}{(m_1)} \tag{C.10}$$

$$\frac{\partial \varepsilon}{\partial m_{min}} = \frac{\varepsilon}{(m_{min})} \tag{C.11}$$

Finally, the uncertainty in heat transfer coefficient can be calculated from U_{NTUo} and U_{Cmin}

$$U_h = \left[\left(\frac{\partial h}{\partial NTU_o} \cdot U_{NTU_0} \right)^2 + \left(\frac{\partial h}{\partial C_{min}} \cdot U_{C_{min}} \right)^2 \right]^{0.5} \tag{C.12}$$

$$U_h = \left[\left(\frac{h}{NTU_o} \cdot U_{NTU_0} \right)^2 + \left(\frac{h}{C_{min}} \cdot U_{C_{min}} \right)^2 \right]^{0.5} \tag{C.13}$$

APPENDIX D

PRACTICAL CHALLENGES IN BAG SAMPLING METHOD

The bag sampling method (BSM) is a humidity measurement technique proposed in ASHRAE 84 and CSA C439-18 test standards [12], [13] as an alternative for obtaining accurate average humidity measurements at the outlet of FBRs using humidity sensors. The sensor measurements include errors due to the slow response, as explained in Sections 4.7.2 and 4.7.3 of Chapter 4. The BSM is a suitable alternative for determining the average humidity of airstreams. However, it is cumbersome and requires careful attention to achieve accurate measurements. Major challenges observed while implementing the BSM are reported below:

1. Verification of BSM facility:

The bag sampling setup must be verified before applying it to measure the humidity at the FBR outlets. This research verified the setup by measuring the humidity of a steady-state constant humidity airstream using the sensors and the BSM. Both the humidity measurements should agree each other within the experimental uncertainty limits. It must be ensured that there is no condensation of water vapor inside the sampling lines, valves, or bags, and no diffusion of water vapor from (or to) the sampling bags to the surroundings.

2. Contamination of air sample:

In a typical sampling analysis, the air sample is drawn with the help of a vacuum pump and stored in a sampling bag. The sampling tube usually attaches to the suction side of the vacuum pump, and delivery of the pump connects to the sampling bag. This way of connection is not suitable for the humidity measurements since the humidity of the airstream may vary as it flows through the vacuum pump and gets contaminated by the dust and oil from the pump. In this research, the

sample bag placed in a vacuum box (box equipped with a vacuum pump and a flow controller, cf. Figure 4.7) is used to draw air from the outlet of FBRs. Hence the possibilities of contamination were avoided. It should also be noted that the length (i.e., volume) of sampling lines should be kept as minimum as possible to reduce the possibility of the ambient air entering the sampling lines, which were already filled prior to the start of sampling.

3. Types of sampling bags:

Various types of sampling bags are available in the market. The material of the bag is critical as there are possibilities for water vapor diffusion from the high humidity to low humidity side, as reported in ref [119]. The materials with low water permeability rates can be good candidates for the bags. Similarly, the bag design plays a significant role since the bags having a highly restricted opening may result in excessive pressure drop and condensation at high humidity test conditions.

4. Duration of sampling

The duration of sampling is critical since the humidity of airstreams at the FBR outlets varies with time. The air sample should be drawn from the FBR outlets for exactly the same duration of the period. The best method to assure this is to use a relay-controlled vacuum pump where the on-off control can be achieved precisely via a data acquisition system. The BSM is more challenging in single-core test facilities as the conditioned airflow (or the flow at the FBR outlet) is not continuous. In this case, sampling should start at the beginning of each period and be finished at the end of the same period.

APPENDIX E

The sensible, latent, and total effectiveness obtained from experiments and numerical model for twelve different tests are reported in Table E.1.

Table E.1 Test conditions and effectiveness results of silica gel coated small-scale exchanger

Test	Face velocity (m/s)	Period (s)	Mass flow rate (g/s)	NTU_o	Cr^*	H^*	Latent Effectiveness (%) $U_{\varepsilon l}$=±5-8%		Sensible effectiveness (%) $U_{\varepsilon s}$=±3-5%		Total effectiveness (%) $U_{\varepsilon t}$=±5-8%	
							$\varepsilon_{average}$	$\varepsilon_{numerical}$	$\varepsilon_{average}$	$\varepsilon_{numerical}$	$\varepsilon_{average}$	$\varepsilon_{numerical}$
1	1.14	60	7.71	3.2	1.91	0.85	33.5	28.3	57.9	55.3	42.5	43.5
2	1.14	30	7.70	3.2	3.8	0.88	58.6	51	62.5	61.7	57.2	59
3	1.14	15	7.70	3.2	7.6	0.86	69.3	67	64.8	65.2	65.4	65.5
4	1.60	60	10.72	2.3	1.36	0.87	25.02	28.3	52.1	47.6	37	35.4
5	1.61	30	10.72	2.3	2.73	0.92	47.9	51.1	56.9	55.4	48	48.9
6	1.60	15	10.72	2.3	5.45	0.94	61.6	66.9	60.5	59.9	61.5	58.6
7	1.97	60	13.10	1.9	1.12	0.97	25.1	16.2	51.4	45.1	42.1	45.2
8	1.95	30	13.11	1.9	2.23	0.80	40.5	34.5	54.7	52.7	49.6	52.7
9	1.96	15	13.11	1.9	4.46	0.81	57.8	51.9	58.7	57.3	56.6	57.3
10	1.15	30	7.71	3.2	3.8	1.2	57.9	50	60.9	59.8	58.5	59.3
11	1.14	30	7.67	3.3	3.81	3	58	55	55	51.2	57.5	53.2
12	1.14	30	7.71	3.2	3.8	3.3	62.4	61.7	52.1	48.1	60	56.5